Università di Pisa

Facoltà di Scienze Matematiche, Fisiche e Naturali

Corso di Laurea Magistrale in Fisica

Anno Accademico 2013/2014

Tesi di Laurea Magistrale

Density Functional Theory simulations of the electromechanical properties of naturally corrugated epitaxial graphene

Candidato
Tommaso Cavallucci

Relatore
Dott. Valentina Tozzini

Contents

Introduction

Graphene, theoretically known since the 40s, is a single graphite layer, hence a monolayer of carbon atoms arranged in a hexagonal lattice. Studied more like a toy model or to study the graphite properties, it was believed that could not exist, due to its bidimensional structure. When in 2004 Geim and Novoselov isolated layers of free standing graphene, the interest around this material is rapidly increased, thanks to its unique structural and electronic properties related to its bidimensionality. Graphene combines an high flexibility and lightness with a noticeable mechanical resistance. The electronic structure is characterized by the linear dispersion of the π bands near the K point in the Brillouin zone, called Dirac point, where the Fermi energy lies. The linear dispersion implies that electrons near the Dirac point are described by a Dirac-like equation, hence they behave like relativistic particles, yet at low velocities and energies. Graphene is a semimetal with an high mobility of charge carriers, but it can become a semiconductor under appropriate substitutional doping or structural manipulation.

Due to its properties, there is a great interest on graphene based technological application. An important aspect for this purpose is the response of graphene to an external electric field, in particular if it is possible to tune the structure and the electronic properties. The aim of this Thesis work is to study the electromechanical properties and the electronic response to an orthogonal electrostatic field of graphene with the specific focus on the possibility of controlling the local curvature of the graphene sheet by means external electric fields. The interplay between electric field and curvature is related to the flexoelectricity, namely the polarization response to a gradient of strain.

For technological application, the possibility of epitaxially grow graphene on a substrate is very important, and the epitaxial grown on SiC seems promising. The characteristic of graphene are altered by the interaction with the substrate: the structure displays spontaneous ripples due to the compression of the lattice parameter caused by the mismatch with the substrate. The SiC-graphene interface shown a double periodicity: the first is the exact periodicity corresponding to a supercell of 13×13 compared to the graphene unit cell, the second is the periodicity of the rippled structures on graphene, corresponding to a $4\sqrt{3} \times 4\sqrt{3}R30$ supercell. Due to the spontaneous rippling, epitaxial graphene on SiC is an ideal experimental system to study the effect of electric field on curvature. However, up to now, very few experimental studies of graphene embedded in electric fields were published, due to the experimental difficulties.

In this Thesis work, the electronic and structural properties of a graphene system

exposed to electric field, as far as possible similar to the real one, were theoretically studied by means of Density Functional Theory (DFT) based computer calculations and simulations. At variance with the experiment, in computer simulations the exposure to an uniform and static electric field, even of high intensity, is possible with only minor additional difficulties. The model system that reproduce the graphene grown on SiC is quite large, including a thousand of atoms, and the use of massively parallel computational resources and high performing codes is necessary for this kind of simulations. The smaller $4\sqrt{3} \times 4\sqrt{3}R30$ cell, that approximately reproduce the rippling periodicity was also simulated, in addition to the unit cell, used as test and for comparison.

Model systems were simulated at null electric field and with fields of increasing intensity and different direction. The $4\sqrt{3} \times 4\sqrt{3}R30$ graphene cell was simulated at zero compression and with a 2% compression, in order to reproduce the ripples present in the graphene grown on SiC. For this cell also BN doped and N doped graphene structure were simulated. The range of considered electric fields is very large, reaching the limits of those that can currently be practically produced.

In Chapter 1, after a brief summary of the main properties of free standing graphene, the epitaxial grown graphene on SiC is described, showing the differences with the free standing monolayer. Then the flexoelectricity is described. Even if there is not a complete theory of the phenomenon and few articles and experiments have been performed on bidimensional systems, a phenomenological model for surfaces is given. Finally a possible technological application involving graphene is reported, the hydrogen storage. For this purpose the electromechanical properties of graphene are very important, since they could be the key to the functioning of an hypothetical device.

In Chapter 2 the theoretical and computational methods used to obtain the results are reported. The main theorems of the Density Functional Theory are described, as well as the semi-empirical implementation of the dispersion van der Waals interactions. The plane wave expansion and the related concept of pseudopotential are described, as well as methods for the Brillouin zone integration.

In Chapter 3, after a description of the calculation protocols and the model systems, the original results are reported, showing the change of electronic properties (band structure, charge distribution and density of electronic states) and structure due to the electric fields. Directly measurable observables, such as the local DOS measured by Scanning Tunneling Microscopy (STM), were evaluated. The ionization limit is evaluated and the change of flexoelectric properties and the possibility of manipulating curvature is quantitatively estimated, for bare and substituted graphene. These results are of particular interest for technological applications in energy storage and harvesting. In addition, the model systems mimic the real experimental ones and results could hopefully stimulate direct measurements with which they could be straightforwardly compared.

In Chapter 4, finally, conclusions and perspectives are reported after a summary of the main results.

Chapter 1

Properties of graphene

This chapter describes the concepts and the experimental developments on which the calculations are based. First the main characteristic of the free standing graphene are reported, with a focus on the electronic properties. Then an experimental system, the graphene epitaxially grown on silicon carbide, is described, showing the differences with the free standing graphene. This system is particularly important, since it is the reference of the simulations performed in this Thesis work. The flexoelectricity, the electromechanical properties studied, is described for both bulk and bidimensional systems, and previous results of electromechanical coupling of graphene are reported. Finally a possible technological application involving the flexoelectric properties of graphene is reported, the hydrogen storage.

1.1 Free standing graphene

Graphene is a monolayer of carbon atoms arranged in a honeycomb lattice. The flexibility of the bonds between carbon atoms allows different graphene based structure to be stable, whose properties depend on the structure size, symmetry and dimensionality. In fact graphene is the basis for all graphitic materials of different dimensionality, from fullerene to graphite[1] (Fig. 1.1). Fullerene is obtained from graphene by introducing pentagons in the hexagonal structure that create a curvature ("0D graphene"). Rolling up graphene one obtains nanotubes (1D graphene). Finally placing graphene layers one above the other, bound through van der Waals forces, one obtains graphite, a 3D structure.

Graphene has been studied theoretically since the 40s[2,3] either to better understand graphite or as a toy model, as it was believed that graphene, and all 2D structures, could not exist in free state, but only as a part of 3D structures. Peierls and Landau[4,5] argued that 2D structures were thermodinamically unstable, because the thermal fluctuations in these crystals was comparable to the interatomic distance at any finite temperature. This argument was later extended by experimental observations of Mermin[6], that noted that the melting temperature of thin films decreases with decreasing of thickness and that films of thickness of dozens of atomic layers are unstable.
However in 2004 Geim and Novoselov refuted these theories, isolating, observing

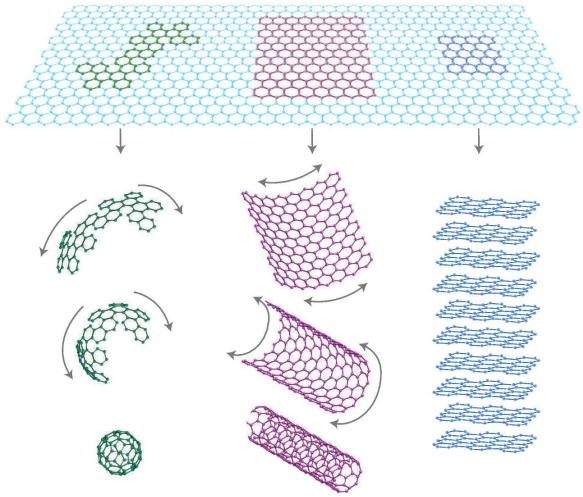

Figure 1.1: From graphene to other graphitic structures with different dimensionality; from left to right: fullerene, carbon nanotube, graphite. Picture from[1].

and measuring the properties of free standing layers of graphene[7].

1.1.1 Lattice structure

Graphene is a strictly bidimensional material since it is one atom thick, and this gives rise to a number of specific phenomena. The structure of graphene is shown in Fig. 1.2(a). It consists of an hexagonal lattice with two atoms per unit cell: this means that there are two overlapping sublattices, whose atoms are indicated in blue and yellow.

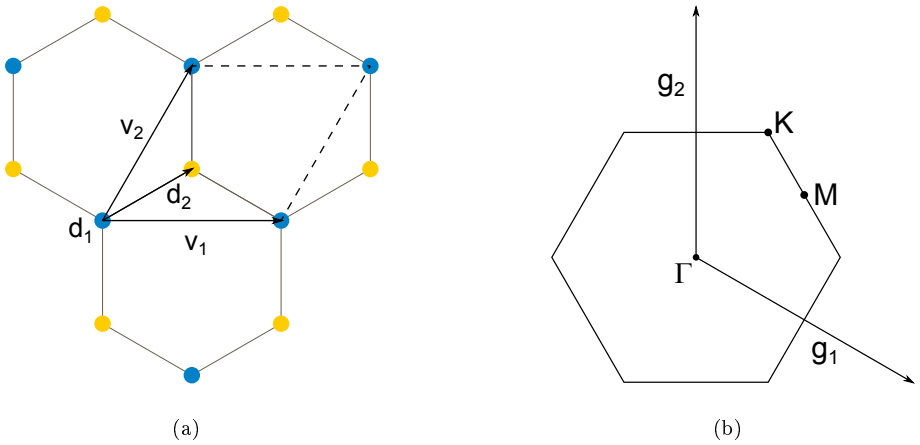

(a) (b)

Figure 1.2: (a) Graphene hexagonal lattice and (b) corresponding Brillouin zone.

The primitive traslational vectors are:

$$\mathbf{v_1} = a\,(1,0) \qquad \mathbf{v_2} = a\left(\frac{1}{2}, \frac{\sqrt{3}}{2}\right) \tag{1.1}$$

The basis vectors, namely the location of the atoms in the unit cell, are:

$$\mathbf{d_1} = (0,0) \qquad \mathbf{d_2} = a\left(\frac{1}{2}, \frac{\sqrt{3}}{6}\right) \tag{1.2}$$

a is the lattice constant and it is the distance between first neightbour of each sublattice; it is equal to 2.46 Å. The carbon bond length is 1.42 Å and is equal to $a/\sqrt{3}$.
The reciprocal lattice of an hexagonal lattice is still hexagonal. In Fig. 1.2(b) is shown the Brillouin zone, with fundamental vectors:

$$\mathbf{g_1} = \frac{2\pi}{a}\left(1, -\frac{\sqrt{3}}{3}\right) \qquad \mathbf{g_2} = \frac{2\pi}{a}\left(0, \frac{2\sqrt{3}}{3}\right) \tag{1.3}$$

The high simmetry points are Γ, M and K in Fig. 1.2(b).

Carbon has four valence electrons and the sp^2 hybridization leads to a trigonal planar geometry in graphene, with σ bonds between atoms that give robustness and strenght to the structure. Three electrons are involved in those bonds, while the fourth lies in a p orbital orthogonal to the crystal. The electrons in sp^2 orbitals give rise to the σ bands and the ones in the p orbital to the π band.

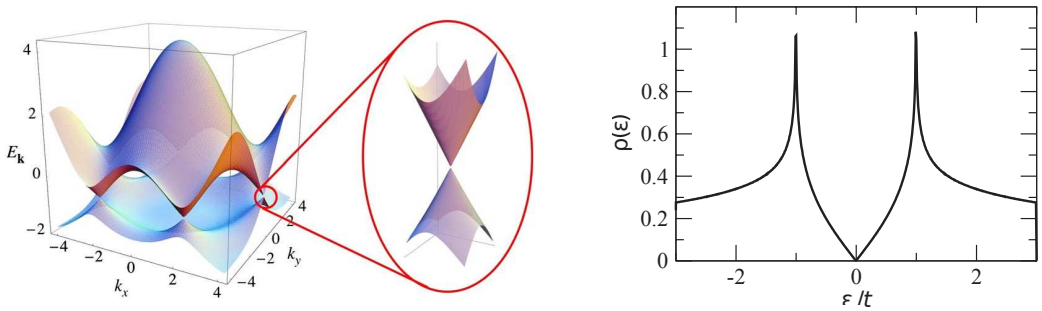

(a) (b)

Figure 1.3: (a) Plot of bidimensional energy surfaces of the π bands in the 2D hexagonal Brillouin zone, obtained by tight-binding calculation; zoom in near the Dirac point. (b) Density of states near the Dirac point; ε and t are tight-binding parameters. Pictures from [8].

Looking at the graph of the bands in Fig. 1.3(a), obtained by tight-binding calculation [8], it can be noted that graphene is a semi-metal: the band gap is null and valence and conduction π bands touch each other only at the K point (called Dirac point), where the states energy equals the Fermi energy and the density of states (DOS) is null (Fig. 1.3(b)).

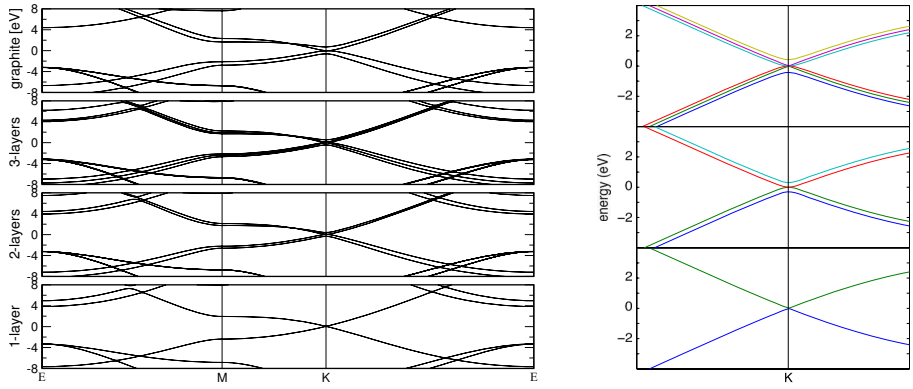

(a) (b)

Figure 1.4: (a) Band structure for mono, bi and three layer graphene and graphite. (b) Zoom in near the K point for mono, bi and three layer graphene. Pictures from [9].

The electronic behaviour of graphene is strictly related to its bidimensionality [9,10]. When more layers are placed one above the other, graphene starts to lose its properties and just with ten layers the electronic structure begins to resemble the graphite one. In Fig. 1.4 the band structure with different graphene layers, up to the graphite structure, are shown. Only mono and bi layer graphene are semimetal, while when more layers are added, the band structure become pretty complex, with valence and conduction bands that start to overlap and do not show the linear dispersion at the K point. According to the electronic structure, graphene could be divided into three groups [1]: monolayer, bilayer and with less than ten layers. Thicker structures should be considered as thin films of graphite.

1.1.2 Dirac point and ballistic transport

At the K point in the Brillouin zone, called Dirac point, the valence and conduction π bands touch each other (Fig. 1.3(a)). The dispersion near this point is linear and this gives rise to an unusual phenomenon in matter physics: the low energy excitations are described by a relativistic Dirac-like (2+1)-dimensional equation, typical of massless particles in quantum electrodynamics (QED).
Electrons near K point are massless, chiral, Dirac fermions, described by the Dirac-like Hamiltonian [8]:

$$H = \hbar v_F \begin{pmatrix} 0 & k_x - ik_y \\ k_x + ik_y & 0 \end{pmatrix} = \hbar v_F \boldsymbol{\sigma} \cdot \mathbf{k} \tag{1.4}$$

$\mathbf{k}$ is the momentum of the quasiparticle, $\boldsymbol{\sigma}$ is the 2D Pauli matrix and v_F is the Fermi velocity, the analog of the speed of light c ($v_F \approx 10^6$ m/s, about 300 times smaller than c). Hence graphene is a unique system for QED studies, since QED properties occur at much smaller speed and non relativistic energies.

Each sublattice contributes to the states of the quasiparticles near the Dirac point. For this to be taken into account, one has to introduce a sublattice index, in analogy with the spin index used in QED, called pseudospin; doing this the spinors, two-component wave functions, are used to describe the relativistic-like electrons. Usually the Pauli matrix is used for the pseudospin, while the real spin of electrons must be described by additional terms.
Due to the Dirac fermions, graphene exhibits the quantum Hall effect even at room temperature[11,12] (Fig. 1.5), since their large cyclotron energies. In fact, due to the linear dispersion, the cyclotron energy is not a constant, but depends on the square root of the electronic density: this was used also for experimental checks of the presence of relativistic electrons.

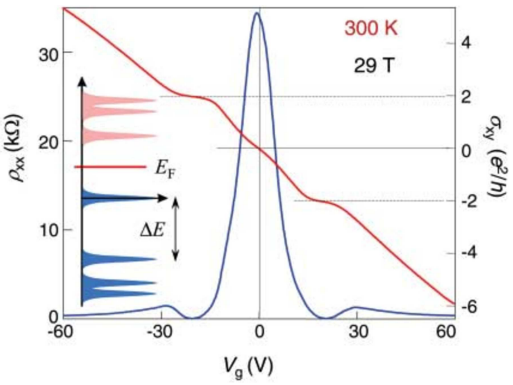

Figure 1.5: Quantum Hall Effect at temperature of 300 K and magnetic field of 29 T. Picture from[12].

Another important electronic property of graphene is the high mobility of charge carriers. Electrons and holes can be tuned continuously till concentrations to 10^{13} cm^{-2}, with the mobility that can go over 15 000 cm^{2}V^{-1}s^{-1} even in ambient conditions. The mobility is also poorly affected by the presence of doping elements. It has been observed[7] that the mobility has a weak dependence on temperature, thus means that is limited by scattering with impurities or imperfections in the structure. In a perfect graphene crystal the mobility could exceed 100 000 cm^{2}V^{-1}s^{-1}. Indeed, under certain conditions, the drift of charge carriers exhibits similar characteristics to the ballistic transport, at least on the micrometre scale: the Dirac fermions seem immune to localization effects, propagating for distances up to 0.3 μm at room temperature, without scattering[1,7].

1.2 Graphene on silicon carbide

Graphene was isolated for the first time by mechanical exfoliation of graphite[7]: layers of graphene were stuck in a scotch tape. However this method produces little and irregular flakes of graphene, interspersed by films of graphite, good for the analysis of fundamental properties, but not for implementation in technological

devices. Moreover the thickness of the graphene zones varies continuously from monolayer, bilayer and few-layer.

One promising method for the production of graphene samples is the epitaxial growth on a substrate of silicon carbide (SiC). The epitaxial growth of graphite on SiC is known from decades: when the silicon carbide is heated up to 1300 °C, the monocrystalline graphite grows on the SiC surface. By fine tuning of the growth parameters, it is possible to obtain a single layer of graphene on SiC[13]. However the interaction with the substrate can modifying the electronic and structural properties of the carbon layer. Actually, the first formed carbon layer is covalently bond to the substrate, and the elastic stress due to the interface (the lattice mismatch between SiC and graphite is equal to 8%[14]) is compensated by the binding energy. The carbon layer electronic properties are then completely different and it cannot be considered graphene. Actually the first layer is used like a buffer layer for the growth of the second layer, that displays properties similar to the free standing graphene.

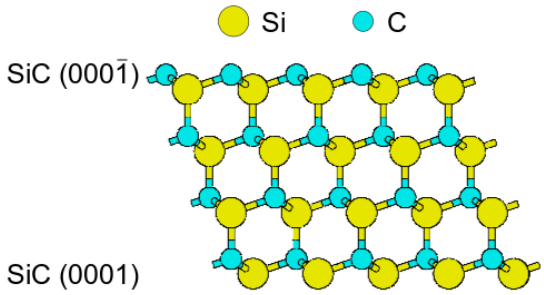

Figure 1.6: Silicon carbide structure. C-terminated surface top, SiC (000$\bar{1}$), Si-terminated surface below, SiC (0001).

The growth can be done in the silicon terminated surface, called SiC (0001), or in the carbon terminated surface, SiC (000$\bar{1}$) (Fig. 1.6): this affect the properties of the carbon layer and of the next ones. In the case of C-terminated surface, the covalent C-C bonds are stronger than the analogues Si-C, therefore the carbon layer is nearer and flatter. Furthermore the rearrangement of the atoms is different from the Si-termination case, so a different periodicity is involved. Finally on the SiC (000$\bar{1}$) graphene grows faster, and is more difficult to obtain the mono or bilayer required. For this reasons in the next sections the focus will be on the Si-terminated surface.

1.2.1 First carbon layer

When the first carbon layer grows on the SiC, the carbon atoms covalently bind to the substrate, namely with silicon atoms in SiC (0001) or with carbon atoms in SiC (000$\bar{1}$). A whole set of experiments show that the rearrangement of the atoms in the Si-terminated case produces a periodicity at the interface that can be represented by a $6\sqrt{3} \times 6\sqrt{3}R30$ cell for the SiC, that correspond to a 13×13 for graphene.

Scanning tunneling microscopy (STM) images evidence also a $\sim 6 \times 6$ periodicity for SiC at the interface ($4\sqrt{3} \times 4\sqrt{3}R30$ for graphene). In Fig. 1.7(a) the two cells are shown, dashed line for $6\sqrt{3} \times 6\sqrt{3}R30$ and bold line for $\sim 6 \times 6$. The latter is very clear, because is related to the bright spots on the carbon layer. For the C-termination the picture is not so clear, however a $6\sqrt{3} \times 6\sqrt{3}R30$ periodicity seems not to be present (data not shown).

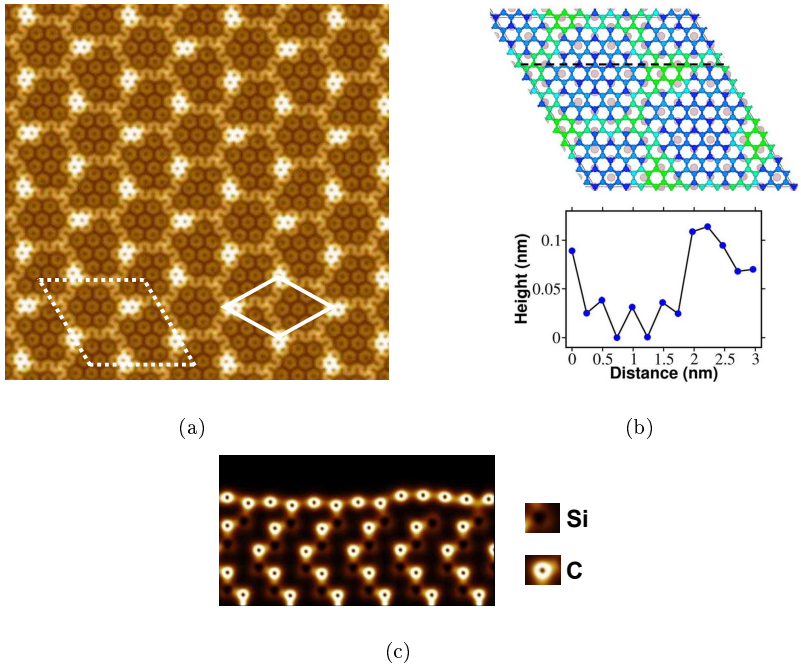

Figure 1.7: Ab initio total charge density of the Si-terminated substrate with one layer of carbon atoms. Analogous images are been obtained by STM observations[15]. (a) Top view of 121 nm^2; the dashed line indicates the $6\sqrt{3} \times 6\sqrt{3}R30$ SiC cell, while the bold line is the $\sim 6 \times 6$ SiC cell. (b) On top the $6\sqrt{3} \times 6\sqrt{3}R30$ cell, with the height of the atoms indicated by the color: blue near the substrate, green for the uppermost atoms; bottom the height profile of the carbon atoms along the dashed line on the top image. (c) Transverse view of the total charge. Pictures from[15].

Ab initio calculations[14–16] show that the substrate atoms involved in the covalent bond move outwards, while the corresponding atoms on the carbon layer relax towards the substrate. The bond lenght is 2.00 Å for the Si-terminated, slightly longer than the SiC bond lenght (1.87 Å). For the C-terminated surface, the C-C bond is stronger and the bond lenght is 1.87 Å. However not all atoms of the carbon layer are bound, hence the average distance of the layer from the substrate is 2.58 Å for the Si-terminated (2.44 Å for the C-terminated). This means that ripples are present in the layer structure, as shown in Fig. 1.7(c). The bright spots related to the $\sim 6 \times 6$ periodicity in Fig. 1.7(a) are the atoms not bound with the substrate that form ripples; dark areas, instead, are atoms covalently bound to the substrate. In the structure is present a pattern of irregular hexagons, each one large about 20 Å and bounded by the bright atoms, due to the mismatch of the lattice parameters. The height difference between the lower and upper atoms is pretty large, about 1.2 Å

(Fig. 1.7(b)).

In Fig. 1.8 the bands energy of the SiC with the buffer layer are shown, both in the Si-terminated and in the C-terminated substate. In both cases the covalent bonding between the carbon layer and the SiC surface preserves the σ bonds of the sp^2 hybridization, and then the corresponding σ bands, while the p orbitals are altered, and the ones of the not bound atoms give rise to a flat π band: there is not a linear dispersion, and hence no graphene-like behavior. Not all the Si atoms are bound with the buffer layer, and the unsaturated ones are responsible of the gap states near the Fermi energy. For the Si-terminated surface, the electronic density at the interface is strongly delocalized, due to the overlapping of the graphene-induced electron states with the conduction band, while for the C-terminated case electron states are more localized; this favors the spin polarization and thus the splitting of the gap state. From the point of view of the bands structure, the Si-terminated surface acts like a metal, while the C-terminated is an insulator.

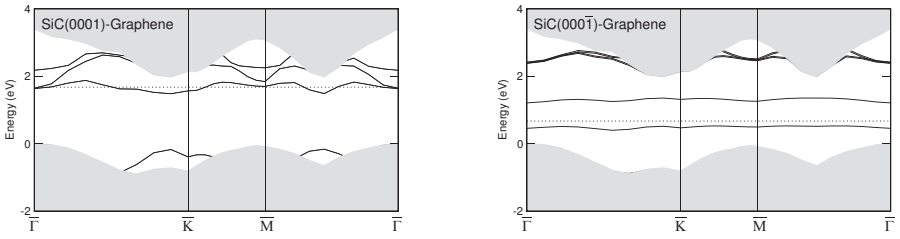

(a) SiC (0001) (b) SiC (000$\bar{1}$)

Figure 1.8: Bands structure at the interface, calculated with the $\sqrt{3} \times \sqrt{3}R30$ cell. The shaded regions are the projected energy bands of SiC. Pictures from [14].

STM experiments demonstrate that the structure of the buffer layer remains substantially unchanged when another carbon layer is added, making it a proper interface or buffer layer for a second (or more) layer of graphene, with a layer by layer epitaxial growth.

1.2.2 Second carbon layer

The second carbon layer, grown on the buffer layer, displays properties very similar to the free standing graphene, hence will be referred as graphene. The graphene layer grows according to the AB stacking scheme of graphite, and interacts with the substrate by van der Waals forces. For the Si-terminated substrate, the mean distance of the graphene plane is 3.35 Å, as the distance between layers in graphite, but graphene tends to follow the morphology of the buffer layer and therefore small ripples are present, as shown in Fig. 1.9(c). These ripples make very clear the $\sim 6\times6$ periodicity of SiC ($4\sqrt{3} \times 4\sqrt{3}R30$ for graphene), visible in Fig. 1.9(a), that now has an hexagonal lattice structure more evident. The ripples have an amplitude of 0.4 Å (Fig. 1.7(b)) and a wavelength of 19 Å.

For what concerns the electronic properties of the second layer, these are very similar to the free standing graphene, even if the interactions with the substrate

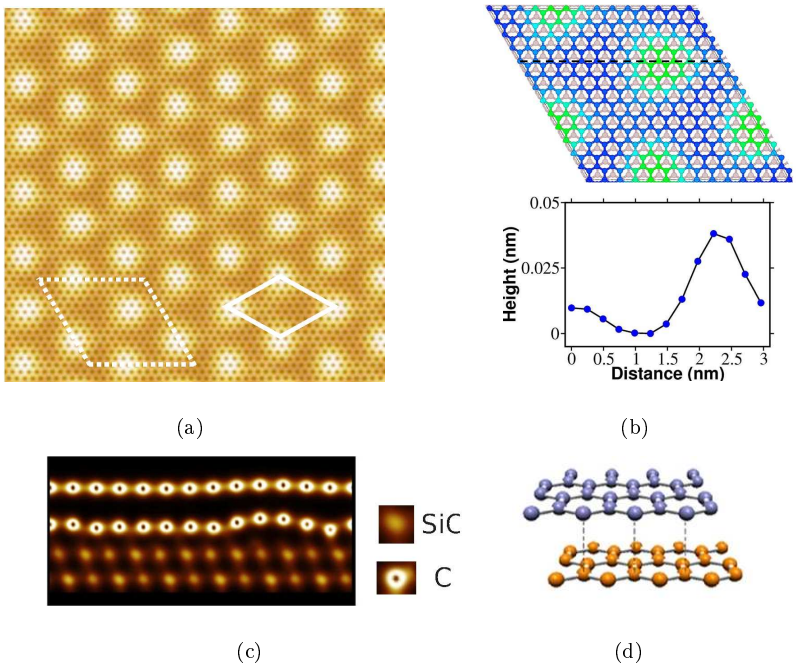

Figure 1.9: (a) (b) (c) Ab initio total charge density of the Si-terminated substrate with two layers of carbon atoms. Analogous images are been obtained by STM observations[15]. (a) Top view of 121 nm^2; the dashed line indicates the $6\sqrt{3} \times 6\sqrt{3}R30$ SiC cell, while the bold line is the $\sim 6 \times 6$ SiC cell. (b) On top the $6\sqrt{3} \times 6\sqrt{3}R30$ cell, with the height of the atoms indicated by the color: blue near the buffer layer, green for the uppermost atoms; bottom the height profile of the carbon atoms along the dashed line on the top image. (c) Transverse view of the total charge. Pictures from[15]. (d) AB stacking of the second carbon layer.

give rise to some differences. In the case of Si-terminated surface, the σ bands of the first layer are shifted up in energy, compared to the analogues of the buffer layer. The metallic state at the interface causes an electron doping (n doping) of about $8.7 \cdot 10^{12}$ cm^{-2}, and hence a displacement of the Dirac point under the Fermi energy, as can be seen in Fig. 1.10(a) and in Fig. 1.10(b), at a value about 0.4 eV below[14]. Furthermore at the Dirac point, a gap of about 0.2 eV appears, together with midgap states[16]. The gap opens because the interaction between graphene and the buffer layer is different depending on the atom's position. This fact breaks the sublattice symmetry of graphene and the wave functions near the Dirac point are the result of the different weight of each sublattice states. Instead the midgap states originate from the coupling between the graphene's p orbitals and the localized p orbitals on the bumped atoms of the buffer layer (the bounding hexagon).

On the C-terminated surface, the interface state is insulating, hence no doping occurs. The Dirac point lies exactly at the Fermi energy, like the free standing graphene, as visible in Fig. 1.10(c).

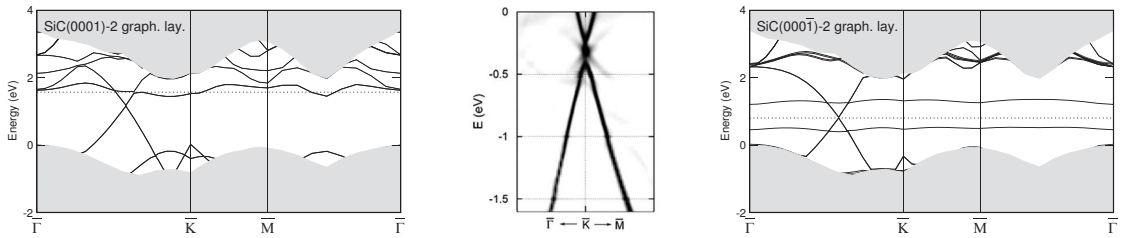

(a) SiC (0001) (b) SiC (0001) (c) SiC (000$\bar{1}$)

Figure 1.10: Bands structure of SiC with two carbon layers. The shaded regions are the projected energy bands of SiC. (a) Si-terminated surface, calculated with the $\sqrt{3} \times \sqrt{3}R30$ cell; picture from[14]. (b) Simulated spectrum for Angle-Resolved Photoemission Spectroscopy (ARPES) of the Si-terminated substrate, in the region near the Dirac point, where the gap and midgap states are visible; picture from[16] (c) C-terminated surface, calculated with the $\sqrt{3} \times \sqrt{3}R30$ cell; picture from[14].

1.3 Flexoelectricity

Since this Thesis work includes a study of interactions of curved graphene with electric fields, it is convenient to review some related concepts.

Flexoelectricity is the response of the polarization in dielectric materials to a gradient of mechanical strain, and can be viewed as an high order electromechanical phenomenon with respect to piezoelectricity, which is the response of the dielectric polarization to a mechanical strain[17]. Unlike piezoelectricity, that arises only in non centrosymmetric materials, flexoelectricity is allowed in materials of any symmetry. The flexoelectric effect in solid is usually weaker compared to others electromechanical effects, but on the nanoscale, where the strain gradient is larger due to the reduced lengths, it plays an important role. Despite this and the fact that it looks promising for technological applications, the understanding of flexoelectricity is still limited, as proved by the contradictory theoretical and experimental results available.

The flexoelectric contribution to the polarization P_i of a 3D crystal subjected to a strain gradient is[17–19]:

$$P_i = \mu_{klij} \frac{\partial \varepsilon_{kl}}{\partial x_j} \tag{1.5}$$

where μ_{klij} is the flexoelectric tensor and x_j are the cartesian coordinates inside the crystal at null strain. ε_{ij} is the strain tensor, defined as the symmetric part of the tensor $\partial u_i / \partial x_j$, where u_i is the displacement of the point x_j:

$$\varepsilon_{ij} = \frac{1}{2} \left(\frac{\partial u_i}{\partial x_j} + \frac{\partial u_j}{\partial x_i} \right) \tag{1.6}$$

This expression for the flexoelectricity refers to the bulk contribution, while the surface contribution is still subject of debate[20,21].

Graphene, exhibiting inversion symmetry, is not intrinsically piezoelectric, but its bidimensionality can produce a symmetry breaking on surfaces and hence new

electromechanical effects, as surface piezoelectricity or flexoelectricity, forbidden in the bulk[22,23]. For bidimensional systems the Eq. 1.5 for the polarization is not straight usable, since it is defined for bulk materials. In this case, the flexoelectricity can be considered as the linear electromechanical coupling proportional to the local curvature. Hence the direct flexoelectric effect, namely the polarization in presence of a gradient of strain, can be rewritten as[24]:

$$P = f(k_1 + k_2) \tag{1.7}$$

k_1 and k_2 are the principal curvatures, related to the Hessian calculated at each point, while f is the flexoelectric constant, related to the charge distribution:

$$f = \int \left.\frac{\partial P(z,k)}{\partial k}\right|_{k=0} \mathrm{d}z \tag{1.8}$$

where z is the coordinate normal to the surface. When a flexoelectric surface is immersed in an external electric field, it starts to bend, a phenomenon called inverse flexoelectric effect, that can be described as follow:

$$k_1 + k_2 = \frac{f}{D}F \tag{1.9}$$

F in the electric field, whereas D is the bending stiffness. In a flat surface of a nonpolar material, the dipole moment is null for symmetry. However when the surface is curved, there is a redistribution of ions and electrons, and a net dipole is created; this dipole is responsible for the flexoelectric coupling with the electric field, that increases with the curvature.

When an electric field is applied transversely to suspended graphene, the surface starts to deflect[25] (Fig. 1.11(a)). In ideal conditions, when the electric field is applied perfectly perpendicular to the plane of graphene, the induced dipole is parallel to the field and there is not moment of electrostatic force, hence no deformation would be possible. However the intrinsic height fluctuations and edge stresses make that the net moment is not null and a deflection appears. Molecular dynamics simulations[25] have proved that the deflection increase not only with the value of the electric field, but also with the size of the graphene surface, as visible in Fig. 1.11(b). For small deflection is possible to write the relation:

$$\delta \approx F\sqrt{\frac{L^3}{C}} \tag{1.10}$$

where δ is the maximum height of the deflection, L is the length of the graphene surface and $C = 60\,653\ \mathrm{eV/nm^2}$ is a constant related to the cross sectional area.

In bidimensional materials like graphene, the flexoelectricity can induce deformations of the shape of the structure under electric field. Deflections parallel to the field are enhanced, while the antiparallel are suppressed. This behaviour could be used for a series of new electromechanical devices based on graphene.

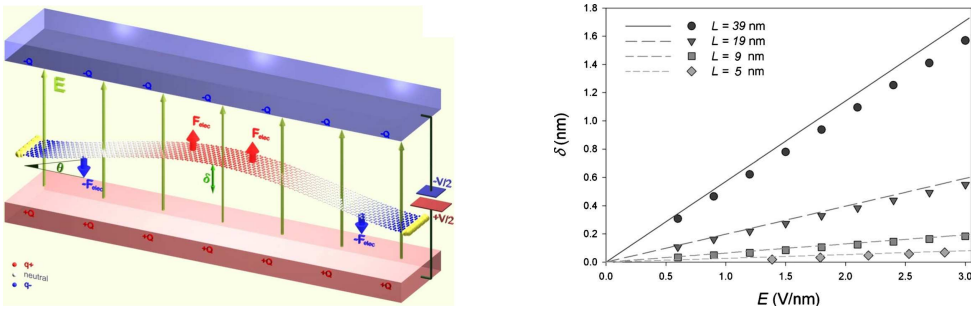

(a) (b)

Figure 1.11: Transverse electric field on suspended graphene. (a) Representation of the forces acting on the surface and of the charge distribution by color scale. (b) Dependency of the deflection by the electic field and the size of the surface of graphene. Pictures from[25].

1.4 Graphene for hydrogen storage

A possible application for graphene in technological devices is the hydrogen storage and transport[26]. Hydrogen is a flammable substance and could be used in fuel cells for the production of electric energy. The simplest way to stock hydrogen is to fill a gas cylinder, but the flammability is very dangerous and limits the amount of hydrogen that is possible to store. Graphene could overcome these problems, because hydrogen can physisorb or covalently chemisorb on the graphene surface.

Both processes are considered for hydrogen storage. The physisorption is more difficult to control and currently does not exhibit great storage capacities, except at low temperature and high pressure. The chemisorption of atomic hydrogen, instead, is an exothermic process with a barrier of about 0.3 eV and a binding energy of about 0.8 eV, depending if others hydrogen atoms are bound. Also molecular hydrogen can chemisorb on graphene, but the process is slower and the energy barrier increases up to values of $1 - 5$ eV, depending on the relative positions of the atoms bound with graphene.

For the atomic hydrogen, the reactivity depends also on the local structures of graphene, in particular by the presence of corrugated regions: hydrogen tends to react with the carbon atom on top of a local curvature, namely H atom binds in the convex curvatures, where the binding energy increases of about 1 eV than the flat surface. The orbitals of the C atom distort their sp^2 hybridization in favor of the sp^3, decreasing the chemisorption barrier and enhancing the reactivity. This type of curvatures are naturally presents on the graphene epitaxial growth on silicon carbide, hence this structure seems good for hydrogen storage. However to realise a device, a controlled mechanism for the hydrogen release must be defined.

A way to release hydrogen is to invert the local curvature: the H atom on the convex surface is now located on a concave curvature. The local geometry affect much on the chemisorption of hydrogen, and when the H atom is on a concave surface spontaneously desorbs: the binding energy decrease of about 2 eV than the convex curvature. When the first atom on the bottom of the concave curvature

is released, it favors the release of other atoms, also in regions of small concavity, giving rise to a sort of chain reaction.

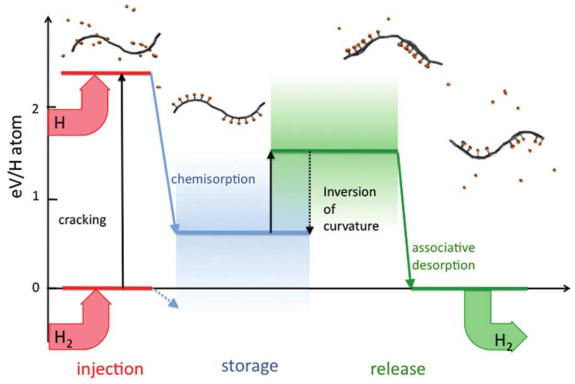

Figure 1.12: Working scheme for the possible hydrogen storage device. Picture from[26].

The working scheme for the hydrogen storage device is shown in Fig. 1.12. It consists of three steps:

1. *Injection*: the molecular hydrogen is broken by cracking in two H atoms that are introduced in the device.

2. *Storage*: the atomic hydrogen binds to the ripples of the graphene surface. Hydrogen is now stocked in the device and can be transported.

3. *Release*: the graphene curvature is inverted, and the hydrogen atoms are released. They bind in molecular hydrogen that is available in gaseous state.

How to invert the curvature is not yet defined. The attention is focused on the response of graphene to electric field: the flexoelectric properties, enhanced by appropriated doping, could permit the inversion, even partial, of the curvature. The curvature manipulation is interest as a way to control the adsorption and desorption, but it could find application in many others fields: the correlation between flexibility and electricity opens the way to the generation of potential differences related to substances flows that change the curvature, or the curvature control by electric field could be used for substances transport by means of graphene.

Chapter 2

Methods: Density Functional Theory and its plane wave implementation

This chapter describes the theoretical and computational methods used to obtain the results of this Thesis work. The basics of the Density Functional Theory are first reported, with a specific focus on the expansion in plane waves for the self consistent orbitals. The approximations used are described: treatment of the electronic exchange and correlation, description of van der Waals dispersion, treatment of the core electrons. A brief description of the algorithms used and of the code in which they are implemented is finally given.

2.1 Density Functional Theory: basic concepts

Addressing a system with a large number of atoms with quantum mechanics in computer simulations imposes some simplification to maintain the computational cost low enough. One commonly used the Born-Oppenheimer approximation: the mass ratio between a nucleus and an electron is so large that the nuclei could be considered frozen from the point of view of electron dynamics. This means that is possible to separate adiabatically the dynamics of electrons and nuclei, namely, indicating with Φ the total wave function:

$$\Phi = \psi(r, R)\varphi(R) \tag{2.1}$$

where $\varphi(R)$ is the nuclear wave function and $\psi(r, R)$ the electronic one.
Focusing on the electronic problem, one way to reduce the computational cost is to transform the many body problem into an equivalent one-electron problem in effective external field. The Density Functional Theory (DFT) locates within this class of theories, being a mean field ground state theory in which the emphasis is set on the one body electron density. It is based on two main pillars, namely the Hohenberg-Kohn theorem and the Kohn-Sham scheme, described in the following.

After the Born-Oppenheimer separation, the electronic system can be described as a system of N interacting electrons in an external potential V_{ext}, namely the electrostatic potential of the nuclei[27,28]. The Hamiltonian of the system is written

as:

$$H = H_{int} + V_{ext} \tag{2.2}$$

H_{int} includes the electrons kinetic energy and the electron-electron interaction:

$$H_{int} = \sum_{i=1}^{N} \frac{|\mathbf{p}_i|^2}{2m_\mathrm{e}} + \frac{1}{2}\sum_{i\neq j} \frac{\mathrm{e}^2}{|\mathbf{r}_i - \mathbf{r}_j|} \tag{2.3}$$

the sum runs over the electrons indices. The external potential, generated by the nuclei, can be rewritten as:

$$V_{ext} = \sum_i v_{ext}(\mathbf{r}_i) = -\sum_i \sum_I \frac{Z_I \mathrm{e}^2}{|\mathbf{r}_i - \mathbf{R}_I|} \tag{2.4}$$

where $\mathbf{R}_I$ are the nuclear coordinates. Naming $|\Psi\rangle$ the ground state of the system, the electron density is defined as:

$$n(\mathbf{r}) = \langle\Psi(\mathbf{r}_1 \dots \mathbf{r}_N)| \sum_i \delta(\mathbf{r} - \mathbf{r}_i) \, |\Psi(\mathbf{r}_1 \dots \mathbf{r}_N)\rangle \tag{2.5}$$

Since the mass of the electrons, their charge, their number and their interaction are given, the only variable of the system is the external potential V_{ext}. The Hohenberg-Kohn theorem states that there is a one to one correspondence between the external potential and the ground state electron density: this means that the variable of the system became the electron density, and that there is only one external potential (apart from additive constant) that leads to a given ground state charge density. Moreover the ground state depends on the electronic density:

$$\Psi = \Psi\left[V_{ext}\right] = \Psi\left[n(\mathbf{r})\right] \tag{2.6}$$

Also the ground state energy is a functional of the charge density: in fact the energy is determined by the ground state Ψ, that is proved to be a functional of the density. This means that also the expectation values of the kinetic energy of electrons and their interactions are functionals of the charge density. In mathematical terms the functional $E\left[n(\mathbf{r})\right]$, called the Hohenberg-Kohn functional, is expressed as:

$$E\left[n(\mathbf{r})\right] = \langle\Psi| \, T + V_\mathrm{ee} + V_{ext} \, |\Psi\rangle = T\left[n(\mathbf{r})\right] + V_\mathrm{ee}\left[n(\mathbf{r})\right] + \int n(\mathbf{r}) v_{ext}(\mathbf{r}) \, \mathrm{d}^3\mathbf{r} \tag{2.7}$$

T is the kinetic energy and V_ee is the electron-electron interaction. The energy functional is minimized by the exact ground state charge density: in this case the energy value is the exact of the many body system. The problem is then reduced to the determination of the electron density that minimize the energy functional. However the functional $T\left[n(\mathbf{r})\right] + V_\mathrm{ee}\left[n(\mathbf{r})\right]$, even if universal (it does not depend on the external potential but only on the charge density) is not known explicity.

An operative way to use the principles included in the Hohenberg-Kohn theorem is provided by the Kohn-Sham scheme. The ground state density is decomposed in a set of one electron orthonormal orbitals:

$$n(\mathbf{r}) = \sum_{i=1}^{N} |\phi_i(\mathbf{r})|^2 \tag{2.8}$$

ϕ_i are the Kohn-Sham orbitals. They are chosen with the help of an auxiliary system of non-interacting electrons. Eq. 2.8 describes a system of N non-interacting electrons with the same ground state charge density $n(\mathbf{r})$. The Kohn-Sham orbitals are solutions of the single electron Schrödinger equation:

$$\left[-\frac{\hbar^2\nabla^2}{2m} + V(\mathbf{r})\right]\phi_i(\mathbf{r}) = \varepsilon_i\phi_i(\mathbf{r}) \tag{2.9}$$

$V(\mathbf{r})$ is an effective external potential including the effect of all interacting electrons in addition to the external potential. The Hohenberg-Kohn theorem implies that the potential $V(\mathbf{r})$ is totally determined by $n(\mathbf{r})$ and it is unique.
The energy functional is conveniently rewritten as:

$$E\left[n(\mathbf{r})\right] = T_0\left[n(\mathbf{r})\right] + E_H\left[n(\mathbf{r})\right] + \int n(\mathbf{r})v_{ext}n(\mathbf{r})\,\mathrm{d}^3\mathbf{r} + E_{xc}\left[n(\mathbf{r})\right] \tag{2.10}$$

where T_0 is the kinetic energy of the non-interacting electron system, E_H is the Hartree energy, namely the Coulomb interactions between clouds of charge, and E_{xc} is the exchange-correlation energy, that contains all the unknown informations. It is defined as:

$$E_{xc}\left[n(\mathbf{r})\right] = T\left[n(\mathbf{r})\right] - T_0\left[n(\mathbf{r})\right] + V_{\mathrm{ee}}\left[n(\mathbf{r})\right] - E_H\left[n(\mathbf{r})\right] \tag{2.11}$$

Using the variational principle, one obtains the Kohn-Sham equations[29]:

$$\left[-\frac{\hbar^2\nabla^2}{2m} + V_H(\mathbf{r}) + V_{xc}\left[n(\mathbf{r})\right] + V_{ext}(\mathbf{r})\right]\phi_i(\mathbf{r}) = \varepsilon_i\phi_i(\mathbf{r}) \tag{2.12}$$

V_H and V_{xc} are the potentials associated to the Hartree and the exchange-correlation energies, and can be expressed as:

$$\begin{aligned} V_{xc}\left[n(\mathbf{r})\right] &= \frac{\delta E_{xc}\left[n(\mathbf{r})\right]}{\delta n(\mathbf{r})} \\ V_H(\mathbf{r}) &= \mathrm{e}^2\int\frac{n(\mathbf{r}')}{|\mathbf{r}-\mathbf{r}'|}\,\mathrm{d}^3\mathbf{r}'\phi_i(\mathbf{r}) \end{aligned} \tag{2.13}$$

The Kohn-Sham equations are standard differential equations; an effective potential $V_{KS}(\mathbf{r})$ appears, due to the nuclear, the Hartree and the exchange-correlation terms:

$$V_{KS}(\mathbf{r}) = V_H(\mathbf{r}) + V_{xc}\left[n(\mathbf{r})\right] + V_{ext}(\mathbf{r}) \tag{2.14}$$

In DFT simulations, one makes an initial guess on the electron density, as can be seen in Fig. 2.1, and proceeds solving the Kohn-Sham equations to calculate new orbitals. If the results are self-consistent, the DFT calculation ends and the orbitals are used to calculate all the physical quantities of the system; otherwise, the new electronic density, obtained with the new orbitals, is used to repeat the cycle until the convergence is achieved. With the Kohn-Sham orbitals and their energies

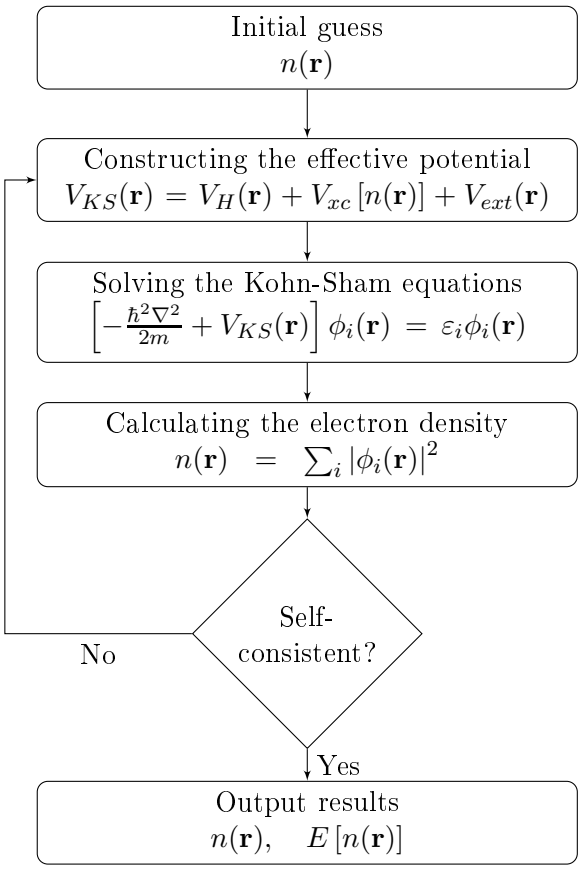

Figure 2.1: Flow chart of the DFT self-consistent calculation.

determined, is possible to calculate the ground state energy, with the following expression:

$$E = \sum_i \varepsilon_i - \frac{1}{2}\sum_{ij} \langle\phi_i\phi_j| \frac{e^2}{r_{ij}} |\phi_i\phi_j\rangle + E_{xc}[n(\mathbf{r})] - \int n(\mathbf{r})V_{xc}(\mathbf{r})\,\mathrm{d}^3\mathbf{r} \tag{2.15}$$

The orbital energies ε_i do not have a direct physical meaning, being just Lagrange multipliers, although their differences can be used as very rough approximations for the excitation energies.

2.1.1 Approximations for the exchange-correlation energy

In the derivation of the Kohn-Sham equations, all the unknown terms are hidden into the exchange-correlation energy. However this functional is not of any practical use, because it is totally unknown, hence some approximations must be done. The most popular is the local density approximation (LDA), introduced by Kohn and Sham[29]. The exchange-correlation functional is written as:

$$E_{xc}^{LDA}[n(\mathbf{r})] = \int \varepsilon_{xc}(n(\mathbf{r}))n(\mathbf{r})\,\mathrm{d}^3\mathbf{r} \tag{2.16}$$

$\varepsilon_{xc}(n(\mathbf{r}))$ is the many body exchange-correlation energy per electron of a homogeneous gas. The exchange-correlation potential takes the form:

$$V_{xc}^{LDA}[n(\mathbf{r})] = \frac{\delta E_{xc}^{LDA}[n(\mathbf{r})]}{\delta n(\mathbf{r})} = \varepsilon_{xc}(n(\mathbf{r})) + n(\mathbf{r}) + \frac{\mathrm{d}\varepsilon_{xc}(n(\mathbf{r}))}{\mathrm{d}n(\mathbf{r})} \tag{2.17}$$

A numerical expression for $\varepsilon_{xc}(n)$ can be obtained by Monte Carlo calculations[27,30]:

$$\varepsilon_{xc}(r_s) = \begin{cases} -\dfrac{0.9164}{r_s} - \dfrac{0.2846}{1 + 1.0529\sqrt{r_s} + 0.3334 r_s} & r_s \geq 1 \\ -\dfrac{0.9164}{r_s} - 0.0960 + 0.0622 \ln r_s - 0.0232 r_s + 0.0040 r_s \ln r_s & r_s \leq 1 \end{cases} \tag{2.18}$$

The result is expressed in Rydberg, while r_s is a dimensionless parameter related to the electron density, and defined as:

$$\frac{4}{3}\pi (r_s a_B)^3 = \frac{1}{n} \tag{2.19}$$

where $a_B = 0.529$ Å is the Bohr radius. The LDA was introduced in analogy with the Slater local approximation[31] of the exchange potential in the Hartree-Fock equations. In these equations there is not an exchange-correlation terms, but an exchange potential V_x appears. The exchange potential in HF theory is a nonlocal operator, so to facilitate the comparison the Slater local approximation can be considered:

$$V_x(\mathbf{r}) = -\frac{3}{2}\frac{\mathrm{e}^2}{\pi}\left[3\pi^2 n(\mathbf{r})\right]^{\frac{1}{3}} \tag{2.20}$$

which could be considered the exchange-only part of the Eq. 2.17. In this sense, the DFT is an extension of the HF theory.

LDA fails when spatial density fluctuations are large and short ranged. Thus, a more accurate approximations are needed specifically in atomic and molecular systems, where the electronic charge is localized in space. Usually gradient corrections are introduced; the exchange-correlation energy is written as a function of the local charge density and of its gradient, that is the generalized gradient approximation (GGA):

$$E_{xc}^{GGA}[n(\mathbf{r})] = \int \varepsilon_{xc}\left(n(\mathbf{r}), \nabla n(\mathbf{r})\right) \mathrm{d}^3\mathbf{r} \tag{2.21}$$

The LDA usually overrates the cohesive energy and the bond strenght; these problems are especially corrected with GGA functionals. Moreover the GGA improves atomization energies, energy barriers, structural energy differences, and it favors density inhomogeneity more than LDA.
Among the most widely used GGA-based functional is the PBE (Perdew, Burke and Ernzerhof)[32]. This kind of functional has a pretty simple implementation of the GGA, because has few parameters; the energy functional is written as:

$$E_{xc}^{GGA}[n(\mathbf{r})] = \int n(\mathbf{r}) \varepsilon_x(n(\mathbf{r})) F_{xc}\left(n(\mathbf{r}), |\nabla n(\mathbf{r})|\right) \mathrm{d}^3\mathbf{r} \tag{2.22}$$

F_{xc} is called enhancement factor and is usually written in terms of the dimensionless variables r_s and $s(\mathbf{r})$:

$$s(\mathbf{r}) = \frac{|\nabla n(\mathbf{r})|}{2k_F n(\mathbf{r})} \tag{2.23}$$

The PBE functional is build mainly taking into account the energetic constraints, and combines the LDA simplicity with the energetic corrections of the GGA.

However some inaccuracies still remain also with the GGA functionals. The first is the impossibility to reproduce the van der Waals interactions, due their nonlocal behaviour; another important is the underestimation of the band gap. To estimate the band gap one has to calculate the excited states and their eigenvalues. The DFT is a ground state theory and is not much accurate to reproduce excited states; moreover the Kohn-Sham orbitals and their energies are mathematical quantities, with no physical meaning. In DFT the band gap is usually underestimated by a 40-50%, with LDA, little less GGA. For the same reasons, the slope of the bands at K point in graphene is underestimated of 10-20%[33]. This is due to the inability of the approximated functionals to reproduce the dependence of the real functional on the number of electrons. Better agreement are obtained with nonlocal functionals including a given portion of explicit exchange (such as B3LYP[34,35] or PBE0[36]) and with theories including the self energy (like GW theory[37]), or using the Time-dependent DFT[38] which evaluates the true electronic excitation of the system self-consistently. However all of these approaches imply a noticeable increasing of the computational cost and cannot generally be used for extended systems. Thus they are beyond the scope of this Thesis work.

2.1.2 Van der Waals forces

The van der Waals forces are intermolecular interactions caused by charge fluctuations, attractive on long range and repulsive on short range. Even if they are weaker than the covalent or ionic bonds, they play an important role in many systems: for example they are presents in the graphite, where they bind the graphene layers, or in the second carbon layer grown on SiC, that is bound to the buffer layer by van der Waals interactions; moreover they play a main role at surfaces and interfaces, where they are responsible of the orientation of the molecules. Van der Waals forces include three kind of interactions[39]:

- Keesom force: interaction between two permant dipoles;
- Debye force: interaction between a permanent dipole and a corresponding induced dipole;
- London force: dispersion interaction between two instantaneously induced dipoles.

The latter is underestimated in the LDA or GGA functionals due to its nonlocal character. In fact it is caused by the dipole in a part of the system induced by the charge fluctuations in another part.

From a theoretical point of view the best way to reproduce the van der Waals interactions is to use a nonlocal exchange-correlation functional[34–36]. However this leads to a much heavier calculation. A simpler approach is to add a semi-empirical dispersion term to the DFT energy[40,41], like the method of Grimme, the DFT-D2. With the DFT-D2 method the energy is written as:

$$E_{DFT-D} = E_{DFT} + E_{disp} \tag{2.24}$$

where E_{DFT} is the Kohn-Sham energy of Eq. 2.15 and E_{disp} is the empirical dispersion correction:

$$E_{disp} = -s_6 \sum_{i=1}^{N-1} \sum_{j=i+1}^{N} \frac{C_6^{ij}}{R_{ij}^6} f_{dmp}(R_{ij}) \tag{2.25}$$

N is the number of atoms, s_6 is a scaling factor that only depends on the type of functional, R_{ij} is the distance between the i-th atom and the j-th and C_6^{ij} is the dispersion coefficient for the atom pair ij. Finally $f_{dmp}(R)$ is a damping function, used to avoid near-singularities for small interatomic distances R. The dispersion coefficients C_6^{ij} for different atomic species are obtained by a geometric mean of specific atomic C_6 coefficients:

$$C_6^{ij} = \sqrt{C_6^i C_6^j} \tag{2.26}$$

In the calculation of the atomic C_6 coefficients, several observable enter, such as the ionization potential and the static dipole polarizability.
The damping function is given by the following expression:

$$f_{dmp}(R) = \frac{1}{1 + e^{-d(R/R_r - 1)}} \tag{2.27}$$

where d is a parameter and R_r is the sum of atomic van der Waals radii.

Being an empirical implementation of the van der Waals forces, some limitations remain. In particular, the C_6 coefficients are calculated for isolated atoms in the ground state, but the electronic behaviour of an atom in a molecule or in a crystal can be different.

2.2 Plane wave basis set

Kohn-Sham equations (Eq. 2.12) are generally solved expanding the orbitals in a suitable basis set. Different basis sets can be chosen, each one with their characteristics and benefits. One of the most used in crystal structures is the expansion of the orbitals in a sum of plane waves, to take advantage of the lattice periodicity.

In a periodic lattice the Bloch theorem applies and the orbital wave functions can be written as:

$$\phi_{j,\mathbf{k}}(\mathbf{r}) = e^{i\mathbf{k}\cdot\mathbf{r}} u_{j,\mathbf{k}}(\mathbf{r}) \tag{2.28}$$

$\mathbf{k}$ is a vector of the first Brillouin zone, while $u_{j,\mathbf{k}}(\mathbf{r})$ is the Bloch function that has the same periodicity of the lattice, and it can be expanded in a Fourier series:

$$u_{j,\mathbf{k}}(\mathbf{r}) = \frac{1}{\sqrt{\Omega}} \sum_{\mathbf{G}} c_{j,\mathbf{k}}(\mathbf{G}) e^{i\mathbf{G}\cdot\mathbf{r}} \tag{2.29}$$

where Ω is the volume of the primitive cell in reciprocal space and $\mathbf{G}$ is a vector of the reciprocal lattice. In a periodic lattice, also the Kohn-Sham effective potential must be periodic, namely $V_{KS}(\mathbf{r}) = V_{KS}(\mathbf{r}+\mathbf{R})$, where $\mathbf{R}$ is a vector of the Bravais lattice, hence it can be expanded:

$$V_{KS}(\mathbf{r}) = \sum_{\mathbf{G}} \widetilde{V}_{KS}(\mathbf{G}) e^{i\mathbf{G}\cdot\mathbf{r}} \tag{2.30}$$

$\widetilde{V}_{KS}(\mathbf{G})$ is the Fourier transform of the potential. With the plane wave basis, the kinetic energy operator is already diagonal, hence substituting the expansions of the orbitals and of the potential in the Kohn-Sham equations one obtains:

$$\sum_{\mathbf{G}'} \left[\frac{\hbar \left|\mathbf{k}+\mathbf{G}\right|^2}{2m_\mathrm{e}} \delta_{\mathbf{G},\mathbf{G}'} + \widetilde{V}_{KS}(\mathbf{G}-\mathbf{G}') \right] c_{j,\mathbf{k}}(\mathbf{G}') = \varepsilon_{j,\mathbf{k}} c_{j,\mathbf{k}}(\mathbf{G}) \tag{2.31}$$

To limit the computational cost, and since the contribution of the higher energy plane waves is less than those of lower, the sum is truncated to a cutoff energy E_{cut}, and done on all plane waves that satisfy:

$$\frac{\hbar^2 \left|\mathbf{k}+\mathbf{G}\right|^2}{2m_\mathrm{e}} < E_{cut} \tag{2.32}$$

The cutoff energy is an input parameter of all the plane waves-based DFT simulations and is system dependent, hence it must be setted empirically after few tests. The higher its value, the more accurate are the results of the simulation, but also heavier the computation. Hence a compromise must be found. This is also chosen considering the calculation of the electronic density:

$$n(\mathbf{r}) = \sum_{j}^{\mathrm{occ}} \int_{\Omega} \frac{\mathrm{d}^3\mathbf{k}}{\Omega} \left|\phi_{j,\mathbf{k}}(\mathbf{r})\right|^2 = \sum_{\mathbf{G}} \widetilde{n}(\mathbf{G}) e^{i\mathbf{G}\cdot\mathbf{r}} \tag{2.33}$$

which also requires a cutoff E_{n-cut}. Since the electronic density is the square of the orbitals it can vary twice as rapidly, hence the cutoff must be higher, or at least equal, than the corresponding for orbitals for an accurate representation:

$$\frac{\hbar^2 \left|\mathbf{G}\right|^2}{2m_\mathrm{e}} < E_{n-cut} \tag{2.34}$$

Again the choice of E_{n-cut} must be in balance between an high accuracy and a cheap calculation.

The plane wave expansion is widely used in DFT simulations, because has some benefits: the basis set is independent of atomic species or positions, and the switch

between real and reciprocal space is done by fast Fourier transform (FFT), a very efficient algorithm. However the plane wave expansion can only address periodic systems. Non periodic system (e.g. molecules) are approximated using periodic systems with supercells large enough to leave a sufficient amount of empty space between molecules. Another problem is the representation of the very localized orbitals which would require very large energy and density cutoffs: this problem particularly rises with core electrons. To address this problem, the concept of pseudopotential was introduced[42].

2.2.1 Pseudopotential and ultrasoft pseudopotential

In a crystal, the electrons of an atom can be separated in core and valence ones. The former stay in localized states and do not contribute to the chemical properties of the material. Hence they do not differ much passing from isolated atoms to molecules or crystal. Conversely the valence electrons determine the binding properties of the structure. Since the problem of a bad representation of the localized states in the plane wave expansion affects specifically the core electrons, the pseudopotential method abandon their explicit description, substituting the real potential in the core region with an appropriate pseudopotential. Core electrons are considered frozen and the studied system is then composed of ions, formed by nuclei and core electrons, and valence electrons. The corresponding pseudo wave functions must represent the real ones only outside the core region, without worrying of the chemically inert core states. Moreover the valence states, that rapidly oscillate close to the core region, are made smoother.

The most common forms of pseudopotential are the norm-conserving and the ultrasoft. Norm-conserving pseudopotentials are constructed to enforce the condiction that the norm of a pseudo wave function is equal to the corresponding all-electron wave function, namely that the total pseudo charge and real charge of the system are identical outside the core radius. However this kind of pseudopotentials requires an high cutoff energy to achieve a good accuracy[43].

Ultrasoft pseudopotentials were developed[44] with the specific purpose of reducing the computational cost, relaxing the norm-conserving constraint. The ultrasoft pseudopotential take the form:

$$V_{PS} = V_L + V_{NL} \tag{2.35}$$

where V_L is the local part of the pseudopotential that takes into account the Coulomb interaction between electrons and nuclei, while V_{NL} is nonlocal and describes the interaction between core and valence electrons, included the orthogonalization constraint. For a one-electron atom, the attractive potential is spherically symmetric, hence the solutions may be split into a radial and an angular part. In a many particle system, the DFT approach leads to an analogous Schrödinger equation for each orbital, the Kohn-Sham equation. This means that the effective potential depends only on the radial variable, namely $V_{KS}(\mathbf{r}) = V_{KS}(r)$. Hence also the local term of

the pseudopotential depends on one variable:

$$V_L(r) = \begin{cases} V_{core}(r) & r < r_C \\ V_{AE}(r) & r > r_C \end{cases} \tag{2.36}$$

where r_C is the core radius, namely the distance at which the pseudopotential and the pseudo wave function match the all-electron (AE) corresponding values, as visible in Fig. 2.2.

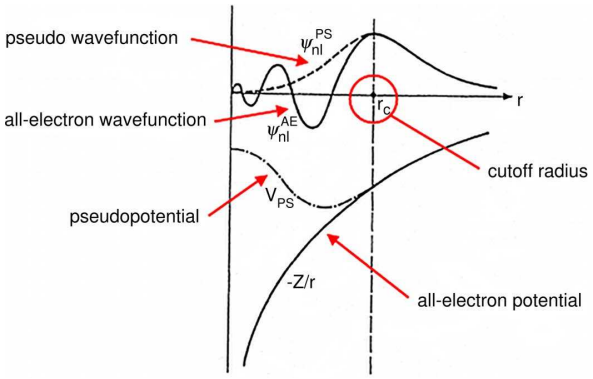

Figure 2.2: Solid line for the all-electron potential and wave function, dashed line for the pseudopotential and the pseudo wave function. The cutoff radius is also visible.

The ultrasoft pseudopotentials allow a much lower cutoff energy values, making the computation cheaper and faster. Without a norm-conserving constraint, the core radius r_C can be increased to larger values than norm-conserving pseudopotential, but this gives rise to the need of an higher plane wave cutoff E_{n-cut} for the electronic density, that is typically several times the cutoff energy E_{cut} used for the wave functions.

2.3 Structural optimization

Once all the details of the electronic and nuclear interactions and of calculations are set, one can proceed exploring the configurational or phase space. The simplest action to take is the search for local minima of potential energy upon variation of the atomic coordinates, namely the structural optimization. In the Born-Oppenheimer approximation, the electronic density and the relaxation of the structure are calculated separately, hence the ionic positions R become parameters of the electronic Hamiltonian and density. Using the Hellmann-Feynman theorem, the force acting on the J-th ion is[27]:

$$\mathbf{F}_J = -\frac{\partial E(R)}{\partial \mathbf{R}_J} = \int n(\mathbf{r};R)\frac{\partial}{\partial \mathbf{R}_J}\frac{z_J \mathrm{e}^2}{|\mathbf{r}-\mathbf{R}_J|}\,\mathrm{d}^3\mathbf{r} - \frac{\partial}{\partial \mathbf{R}_J}\sum_{I\neq J}\frac{z_I z_J \mathrm{e}^2}{|\mathbf{R}_I - \mathbf{R}_J|} \tag{2.37}$$

where z_I and z_J are the atomic numbers and R indicate the array of positions of all atoms, while $\mathbf{R}$ is the position of a single one.

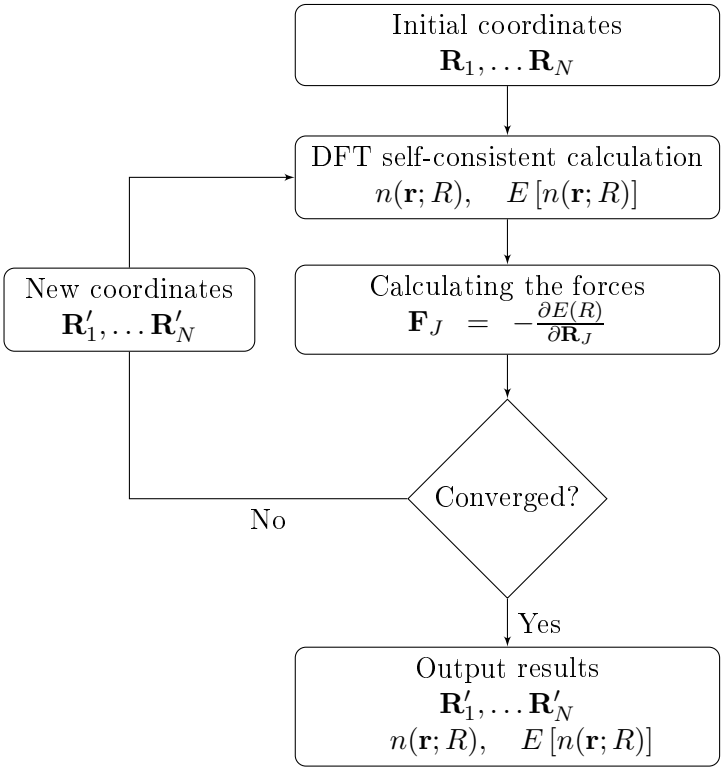

Figure 2.3: Flow chart of the structural optimization.

Knowing the forces acting on them, the atoms are shifted consequently and a new electronic optimization, namely a new DFT self-consistent calculation is done to obtain the new charge density. This cycle is repeated until convergence. Generally the convergence is defined by two threshold parameters, one for the forces and the other for the energies. The first is the maximum value that the force acting on any atoms can have at the convergence. The latter, instead, is related to the energy difference between two consecutive self-consistent steps: the convergence criterion is satisfied if this difference is smaller than the threshold parameter. The convergence is achieved only if both criteria are satisfied[45].

2.4 Brillouin zone integration

As an effect of the expansion of Eq. 2.29, the Kohn-Sham eigenvalues are solutions of an eigenvalue problem that depends on $\mathbf{k}$, hence the total energy must be calculated by an integration on $\mathbf{k}$ over the Brillouin zone. The integral is converted into a discrete sum on N_k specific k-points, that have to be uniformly distributed in the Brillouin zone[46]. A widely used procedure to determine the set of points is the one introduced by Monkhorst and Pack[47], with the formula:

$$\mathbf{k}_{n_1,n_2,n_3} = \sum_{i=1}^{3} \frac{2n_i - N_i - 1}{2N_i} \mathbf{G}_i \tag{2.38}$$

where i indicate a direction, N_i are the number of k-points along the i-th direction, $n_i = 1, \ldots, N_i$ and $\mathbf{G}_i$ are the primitive vectors of the reciprocal lattice.

Obviously increasing the number of sampling points the accuracy of the integration improves, but the calculation becomes heavier, because the corresponding Kohn-Sham orbitals must be calculated. A way to lighten the calculation without loss of accuracy is to exploit the symmetry of the Brillouin zone, reducing the integration region. Points in the reciprocal space grid generated for the Brillouin zone integration are usually connected to each other by symmetry operations. Using these operations, the points to be used in the integration may be reduced to what is known as the irreducible Brillouin zone (IBZ), as shown in Fig. 2.4. If $f(\mathbf{k})$ is a function in reciprocal space, its integral becomes:

$$\int_{BZ} \frac{\mathrm{d}^3\mathbf{k}}{\Omega} f(\mathbf{k}) = \frac{1}{N_k} \sum_{\mathbf{k}}^{BZ} f(\mathbf{k}) = \sum_{\mathbf{k}}^{IBZ} w_{\mathbf{k}} f(\mathbf{k}) \tag{2.39}$$

where N_k is the number of k-points sampled, and $w_{\mathbf{k}}$ is the weight of each k-point.

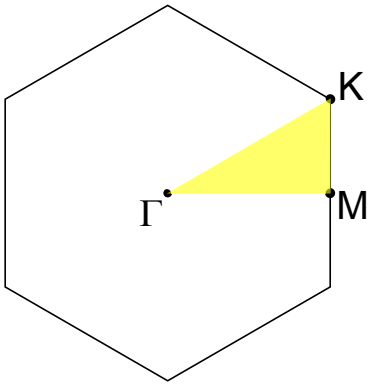

Figure 2.4: Irreducible Brillouin zone in yellow for an hexagonal lattice.

2.4.1 Gaussian smearing

Integrating on the irreducible Brillouin zone over the filled states for metallic materials can cause some inaccuracies. In fact in insulators and semiconductors the Fermi energy lies on the energy gap, hence the density of states (DOS) vanishes smoothly in proximity of the gap. For metals, instead, the gap is null and the sampling of k-points implies that the states near the Fermi energy are not well described. The integral over the filled states of a function $f(\mathbf{k})$ is made multiplying it with a step function $\theta(E(\mathbf{k}) - E_F)$:

$$\int_{BZ} \frac{\mathrm{d}^3\mathbf{k}}{\Omega} f(\mathbf{k})\theta(E(\mathbf{k}) - E_F) = \sum_{\mathbf{k}}^{IBZ} w_{\mathbf{k}} f(\mathbf{k})\theta(E(\mathbf{k}) - E_F) \tag{2.40}$$

where E_F is the Fermi energy. The inaccuracies for metals originate from the difficulty on the reproduction of the step function in plane waves.

In order to overcome this problem, an artificial smearing is introduced, replacing the step function with a smoother one. This implies that states over the Fermi energy are partially occupied, hence an artificial temperature is introduced. Several smearing methods have been developed, starting from the Fermi-Dirac distribution, but one of the widest used is the gaussian smearing, where the step function is replaced by this expression:

$$f_{GS}(E) = \frac{1}{2}\left[1 - \mathrm{erf}\left(\frac{E - E_F}{\sigma}\right)\right] \tag{2.41}$$

$\mathrm{erf}(x)$ is the error function and σ is the smearing parameter, that has no physical interpretation. The parameters for the smearing function are set in the preliminary phases of the calculation by means of tests.

2.5 DFT implementation in the code QUANTUM ESPRESSO

Calculations and simulations of this Thesis work were performed with QUANTUM ESPRESSO. QUANTUM ESPRESSO (QE), acronym for opEn Source Package for Research in Electronic Structure, Simulation, and Optimization[48], is a software suite for electronic structure calculations and materials modeling, based on density functional theory (DFT), plane wave expansion and pseudopotentials. The softwares are written using several programming languages, mainly Fortran-95, but also Tcl, Fortran-77 and C, plus parts of external libraries. A key feature of QE is the implementation of OpenMP and MPI libraries, that allow the parallelization and scalability of simulations on multicores computers.

The main physical quantities that can be calculated with simulations performed using QE are:

- Kohn-Sham orbitals and ground state energy for isolated or periodic systems, also for spin-polarized systems;
- structural optimization;
- electronic density of the ground state and of its projections in selected energy intervals;
- electronic structure in Kohn-Sham approximation and correlated properties;
- phonon dispersions, plus electron-phonon and phonon-phonon interactions and static response functions;
- molecular dynamics using the Car-Parrinello method.

A more detailed and pratical view of the software is reported in App. A.1.

Chapter 3

Results: structural and electronic properties of corrugated graphene with and without electric fields

This chapter reports the original results of this Thesis work. These are organized as follows. The model systems and specific calculation protocols are first described. The model system considered are: the free standing graphene layer, flat and with a corrugation mimicking that of graphene on SiC, with and without substitutional B and N doping; the SiC substrate with buffer layer and with buffer plus monolayer graphene. The calculated structural, energetic and electronic properties of the model system are then reported without and with external electric fields of different intensities and directions.

3.1 Model systems and calculation protocols

3.1.1 Supercell definitions

Considering the symmetry of the ripples of graphene grown on SiC illustrated in Sec. 1.2, three different graphene cells were used for simulations in this work. These are shown in Fig. 3.1(a): the red one is the unit cell, including two carbon atoms and with a cell vector $a = 2.46$ Å; the blue one is the $4\sqrt{3} \times 4\sqrt{3}R30$ that approximately reproduces the periodicity of graphene grown on SiC with lattice constant 17.04 Å; the green one is the 13×13 that reproduces the exact periodicity of the SiC-graphene interface, with a lattice constant of 31.93 Å. This cell was used for simulations of the buffer and monolayer graphene on SiC, thus including several layers of the substrate also, for a total up to 1648 atoms.

Due to the plane wave expansion, there is also a periodicity along the z direction in addition to that on the xy plane, hence the simulated systems are in fact multilayers instead of free standing layers. To simulate as far as possible isolated systems, the lattice constant c, namely the cell height, must be large enough to avoid interactions between two layers. The cell height varies from 20.0 Å to 31.3 Å

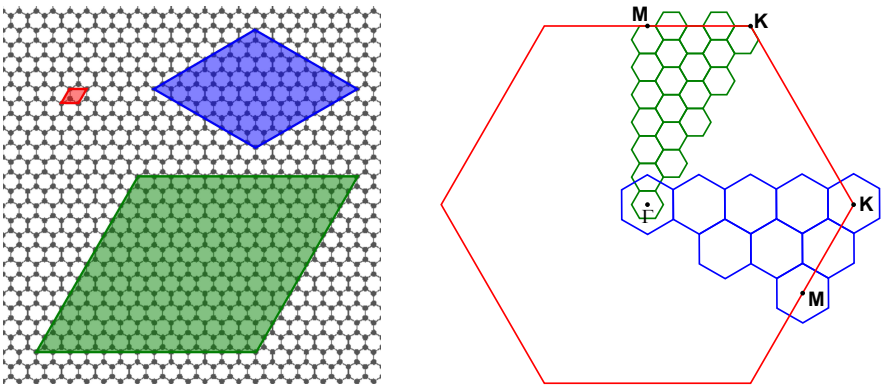

(a) (b)

	Graphene	SiC
—	Unit cell	-
—	$4\sqrt{3} \times 4\sqrt{3}R30$	$\sim 6 \times 6$
—	13×13	$6\sqrt{3} \times 6\sqrt{3}R30$

Figure 3.1: (a) The three supercells used in calculations and simulations and (b) their corresponding Brillouin zones. The color code and the labeling of the cells with respect to the lattice of graphene and SiC are reported in the Table at the bottom.

depending the supercell studied (see below), thus leaving 15-20 Å of empty space between layers.

As it can be seen in Fig. 3.1(b), increasing of the cells size reduces the Brillouin zone. This leads to two consequences: the first is that a smaller Brillouin zone requires a less intensive sampling for the integration to achieve the same accuracy in calculations. This aspect will be discussed in detail in Sec. 3.1.3. The second is that, as it can be seen in Fig. 3.1(b), the refolding of the Brillouin zone of the bigger cells into that of the unit cell, combined with the 30° rotation in the case of the $4\sqrt{3} \times 4\sqrt{3}R30$, generates a remapping of the high simmetry k-points, summarized in Tab. 3.1. In particular this implies that the Dirac point is remapped onto the Γ point in the $4\sqrt{3} \times 4\sqrt{3}R30$ cell.

Unit cell	$\mathbf{4\sqrt{3} \times 4\sqrt{3}R30}$	$\mathbf{13 \times 13}$
Γ	Γ	Γ
M	Γ	M
K	Γ	K

Table 3.1: Remapping of the high symmetry k-points due to the refolding.

Unit cell

The unit cell of graphene includes two carbon atoms at a distance of 1.42 Å. It was used for preliminary simulations and test, in particular for setting the z periodicity for larger cells and for the analysis of the electronic behaviour under high electric

field (see below). The lattice constant is 2.46 Å, while for the cell height the final value of $c = 20.0$ Å was chosen.

$4\sqrt{3} \times 4\sqrt{3}R30$ cell

The $4\sqrt{3} \times 4\sqrt{3}R30$ cell reproduce approximately the periodicity of the ripples of graphene grown on SiC, and includes 96 atoms. The lattice vector lenght is equal to 17.04 Å and the cell height is set to 20.0 Å. Ripples were created by lateral compression. This is achieved by reducing the lattice parameter of 2%, to a value of 16.70 Å. This value was chosen because it was shown to reproduce the experimental amplitude of natural ripples of graphene on SiC[49].

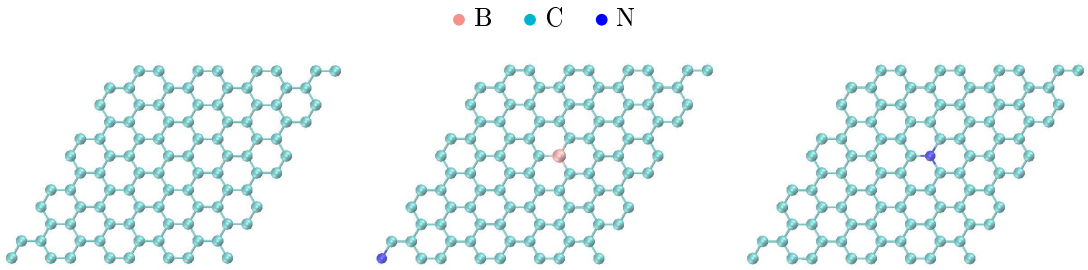

(a) Graphene (b) BN-graphene (c) N-graphene

Figure 3.2: The three systems studied with the $4\sqrt{3} \times 4\sqrt{3}R30$ cell. All these were simulated also with the rippled structure.

Besides pure graphene, this cell was used also for simulations of doped graphene, with boron and nitrogen atoms, in two different configuration, named BN-graphene and N-graphene, shown in Fig. 3.2: all the cell parameters are left unchanged with respect to the undoped graphene. In the BN-graphene two carbon atoms are replaced by boron and nitrogen; the boron atom is placed at the center of the cell (where the rippled structure reaches its maximum height within a concavity over the plane of the flat cell), while the nitrogen one is at the vertex. In N-graphene, one carbon atom is replaced by a nitrogen atom.

The aim of these studies with "substitutional doping" is to investigate if these substitutions can alter the flexoelectric properties of graphene. The specific choice of the location of substitution is indicated by experimental feasibility. In fact one way to create substitutional doping is to expose rippled graphene to substituents, and presumably these will locate on the more reactive sites (namely the convex ones at the center of the cell), thus creating a structure similar to N-graphene, for instance. The structure of BN-graphene is considered as the simplest possible B and N substituted graphene, which also as the advantage of being isoelectronic with pure graphene.

13 × 13 cell with substrate

The 13 × 13 cell was used for simulations of graphene with the SiC substrate. The in plane cell vector is 31.93 Å while c is 31.3 Å. The SiC substrate is implemented with four layers, enough to extinguish the bulk rearrangement, and at the bottom surface the dangling bonds are saturated by hydrogen atoms. The thickness of this structure plus the buffer layer is 11.3 Å, hence to have a vacuum zone of 20.0 Å the cell height c is increased to 31.3 Å. Two systems were simulated with this cell, the buffer layer over a SiC substrate (Fig. 3.3) and a graphene monolayer over the buffer layer (Fig. 3.4).

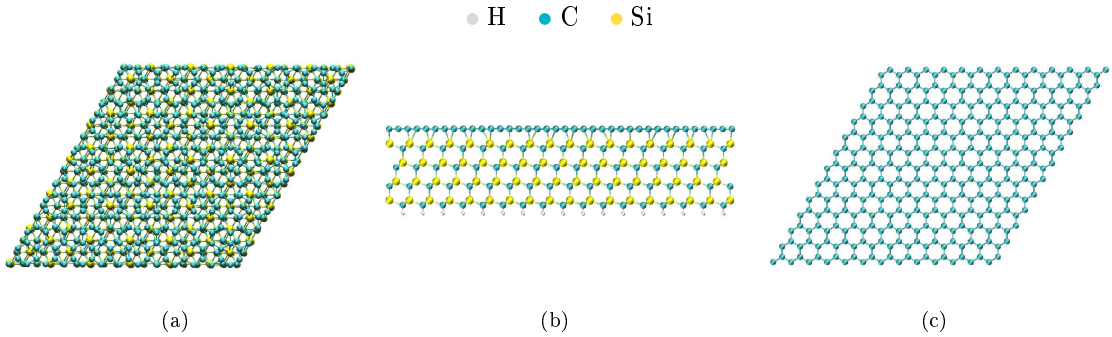

Figure 3.3: (a) Top and (b) side view of the buffer layer structure simulated; the carbon layer was initially placed at 2.0 Å from the SiC surface. (c) Top view of the carbon layer added to the SiC.

Starting from the SiC structure, the buffer layer system was built adding 338 carbon atoms arranged to form a layer at an average distance of 2.0 Å from the Si-terminated surface. The buffer layer is composed by 108 hydrogen atoms, 770 carbon and 432 silicon, for a total of 1310 atoms.

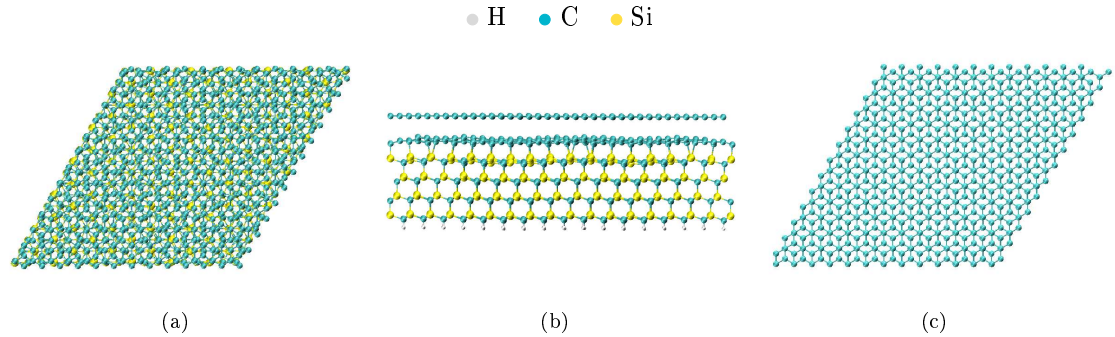

Figure 3.4: (a) Top and (b) side view of the graphene layer on SiC structure; the graphene layer was placed at a main distance of 3.3 Å from the buffer layer. (c) Top view of the two carbon layers over the SiC: one can see the AB stacking of the layers.

For the graphene monolayer on SiC system, the same cell parameters of the buffer layer were used. As can be seen in Fig. 3.4, the system was built adding a

second graphene layer (338 carbon atoms) on the relaxed buffer layer structure, at a mean distance of 3.3 Å and with AB stacking. Hence the system is composed by 1648 atoms, of which 1108 are carbon atoms, while hydrogen and silicon remain unchanged from the buffer layer system, with 108 and 432 respectively. The presence of the graphene monolayer makes that the structure is no more centered on the z direction and the vacuum zone is reduced to 16.6 Å.

3.1.2 Electrostatic field

All the free standing graphene systems were simulated with and without an electric field orthogonal to the graphene sheet up to values of about 40 GV/m, while for the graphene on SiC the field parameters were set for future simulations. Adding a static electric field is made a complex task due to the periodicity along the z direction. In fact the potential generating the electric field must be periodic as well, thus it cannot be an indefinitely linear increasing as the potential generating a uniform electric field should be. Hence a sawtooth like function is used. In order to avoid the numerical instabilities generated by a real sawtooth, the electrostatic potential is designed to drop smoothly in a region which is defined by the input parameters. The systems must be located inside the region of h_F length where the electric field is uniform (Fig. 3.5). Indicating with c the height of the cell, the systems are located at the coordinate $c/2$ and the region h_F is centered around that point, in order to avoid the drop zone.

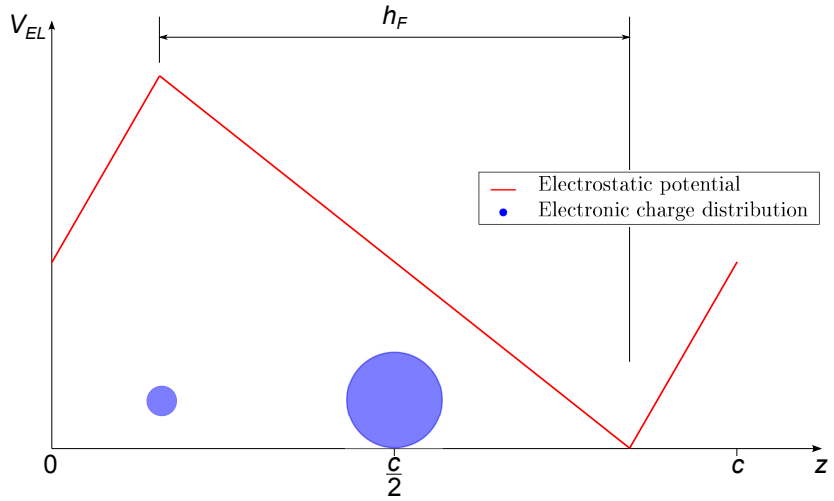

Figure 3.5: Schematic representation of the cell along the z direction. The electrostatic potential, in red, has the sawtooth like shape and the periodicity of c, the cell height. The system is placed at the center of the cell, on the $c/2$ position, and is represented by the big blue electronic charge distribution; with high electric field, some charge can be teared off and it accumulates on the well formed by the change of slope of the potential. The region h_F is where the electric field is equal to the value set by input.

To enhance the response of the systems, high values of the electric field have also been implemented in this Thesis work. This implies that, in some cases, the

ionization limit is reached and charge is teared off from the atoms. Due to the periodic sawtooth shape of the potential, this free charge accumulates in the region where the electrostatic potential changes slope. In order to evaluate the effect of this accumulation, preliminary tests were performed to properly choose the parameters c and h_F. For the unit cell and the $4\sqrt{3} \times 4\sqrt{3}R30$ cell the region h_F has a size of 15.0 Å, while for the 13×13 cell it is set to 23.5 Å, keeping the same ratio between the lenghts of the h_F region and the drop zone of the two others cell. A summary of the main characteristics of all the systems is shown in Tab. 3.2.

System	**Cell type**	$\boldsymbol{a}$ (Å)	$\boldsymbol{c}$ (Å)	$\boldsymbol{h_F}$ (Å)	**Number of atoms**
Graphene	Unit cell	2.46	20.0	15.0	2
Flat graphene	$4\sqrt{3} \times 4\sqrt{3}R30$	17.04	20.0	15.0	96
Rippled graphene		16.70			
Buffer layer	13×13	31.93	31.3	-	1310
Graphene on SiC				23.5	1648

Table 3.2: Main characteristics of the simulated systems.

3.1.3 Setting of calculation parameters

Calculations were performed using PBE pseudopotentials with van der Waals semi-empirical correction. The cutoff energy for the plane wave expansion was set after a convergence test on the unit cell, which results are reported in App. B.1. The cutoff energy for the plane waves was setted to 30 Ry, while the cutoff energy for the electronic density to 300 Ry.

As discussed in the previous sections, with a bigger cell the corresponding Brillouin zone is smaller. This means that a lower sampling is necessary to achieve a good convergence in results. Convergence tests were made for the unit cell and the $4\sqrt{3} \times 4\sqrt{3}R30$ cell with different grid sampling in the reciprocal space, whose data are reported in App. B.2. For the unit cell a 15×15 grid was chosen, while for the $4\sqrt{3} \times 4\sqrt{3}R30$ cell only the Γ point was sampled. Finally for the 13×13 cell, being bigger than the $4\sqrt{3} \times 4\sqrt{3}R30$ and hence having a smaller Brillouin zone, a convergence study was not done and the Γ point sampling was used.

For the electronic optimizations, namely the DFT self-consistent calculations, the convergence criterion was setted to 10^{-8} Ry, while for the structure optimizations the QE default criteria were used, equal to 10^{-3} au for the forces and 10^{-4} au for the energy (au are Hartree atomic units).

Graphene is a semi-metallic material hence a smearing method is necessary to accurately integrate over the Brillouin zone (see Sec. 2.4.1). The gaussian smearing was used and it was set to a value of 0.02 Ry for the unit cell and of 0.01 Ry for the others two cells. All the parameters values are summarized in Tab. 3.3.

3.1.4 Protocols for electronic structures and geometry optimization calculations

The cohesive energy for structures at null electric field is evaluated based on the standard definition:

$$E_{coh} = E_{struct} - \sum_i N_i E_i \tag{3.1}$$

where E_{struct} is the structure energy as obtained by output by QE, N_i is the number of i atoms in the structure and E_i is the energy of the free i atom, calculated with another simulation of one i atom in a large cell with the same parameters. When an electric field is added, both E_{struct} and E_i should be evaluated in the electric field. However this quantity is not easy to evaluate accurately, due to the high polarizability and ionizability of isolated atoms, nor it is the most interesting for this work purposes.

Hence the formation energy referred to the isolated atoms energy in the null field is evaluated:

$$E_f(F) = E_{struct}(F) \sum_i N_i E_i = E_{coh}(F) + E_{field}(F) \tag{3.2}$$

At variance with the cohesive energy, E_f is expected to decrease with electric field F, since it includes the interaction between the polarized system and the electric field.

For the electronic bands structure and the density of states (DOS), differents reciprocal space sampling schemes were used, depending on the cell. For the unit cell, 250 points were sampled along the $\Gamma - \mathrm{M} - \mathrm{K} - \Gamma$ path for the band structure calculations, and a grid of 50×50 was used for the DOS calculations. An analogous sampling for the other two cells would have lead to a too heavy calculation, hence, thanks to the smaller Brillouin zones, a sparser samplings were used, consisting of 100 points along the $\Gamma - \mathrm{M} - \mathrm{K} - \Gamma$ path for the band structure calculations, and a grid of 15×15 for the DOS calculations. All parameters are reported in Tab. 3.3.

Parameter	**Unit cell**	$\mathbf{4\sqrt{3} \times 4\sqrt{3}R30}$	$\mathbf{13 \times 13}$
E_{cut}	30 Ry		
E_{n-cut}	300 Ry		
El. convergence	10^{-8} Ry		
Str. for. conv.	10^{-3} au		
Str. en. conv.	10^{-4} au		
Gaussian smearing	0.02 Ry	0.01 Ry	
k-point grid	$15 \times 15 \times 1$	Γ	
k-point along Γ-M-K-Γ	250	100	
k-point grid (DOS calc.)	$50 \times 50 \times 1$	$15 \times 15 \times 1$	

Table 3.3: Main calculation parameters for the studied cells.

Electronic density were evaluated, and STM images were simulated. For the

latter, a range of energy states of ±0.1 eV around the Fermi energy was selected and the electronic isosurface level was set optimizing to the quality of images.

For the $4\sqrt{3} \times 4\sqrt{3}R30$ cell, rippled structures were also simulated. To obtain a rippled structure, the cell was compressed at 2% of its relaxed value and the structure relaxed after superimposing a small bell shape displacement to guide the ripple formation, as described in App. B.3. This rippled structure was subsequently used for further relaxations within electric field.

3.1.5 Curvature evaluation and flexoelectricity model

To evaluate the flexoelectronic properties of graphene, the measure of the local curvature is necessary. The principal curvatures that appear in Eq. 1.9 cannot be calculated, because they are obtained from the Hessian of the surface. Due to the discrete nature of the studied surfaces, the Hessian is not well defined. Previous works[26,49] have considered the local curvature of the i-th atom by the improper dihedral angle ϕ_i formed by the carbon atom and its three first neighbours, as shown in Fig. 3.6(a), which has positive or negative values depending on convexity and it is null when the structure is flat. Some graphene properties, like the band gap opening at high bending[49], seem to be correlated to the root of the average on all atoms of ϕ^2, that is a measure of the average curvature.

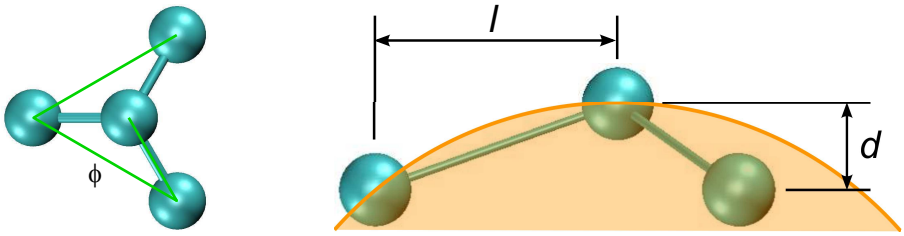

(a) (b)

Figure 3.6: Local curvature of a rippled structure. (a) Improper dihedral angle ϕ. (b) Definition of the variables used for the calculation of the local curvature: d is the height of the atom over the plane of its first neighbours and l is the distance between one first neighbour and the projection of the central atom on the neighbours plane; in orange the local sphere radius.

For each atom, three improper dihedrals are defined, and ϕ_i is defined as theirs average value. Indicating, as in Fig. 3.6(b), with d the height of the i-th atom over the plane of its first neighbours and with l the distance between each first neighbour and the projection of the central atom on the neighbours plane, in the assumption that is the same for all neighbours, the improper dihedral angle ϕ_i is calculated as follows:

$$\phi_i = \mathrm{sgn}(d) \arccos \frac{l}{\sqrt{4d^2 + l^2}} \tag{3.3}$$

For small angles and heights the expression can be approximated with Taylor expansions:

$$\phi_i \approx \frac{2dl}{d^2 + l^2} \tag{3.4}$$

Fig. 3.7(a) reports the improper dihedral for the graphene rippled structure relaxed at 2% compression and the two analytical functions of Eq. 3.3 and Eq. 3.4. As can be seen, the approximated function reproduces pretty well the exact one for angle up to about 20°. For the studied structures, the improper dihedrals rarely overcome this value.

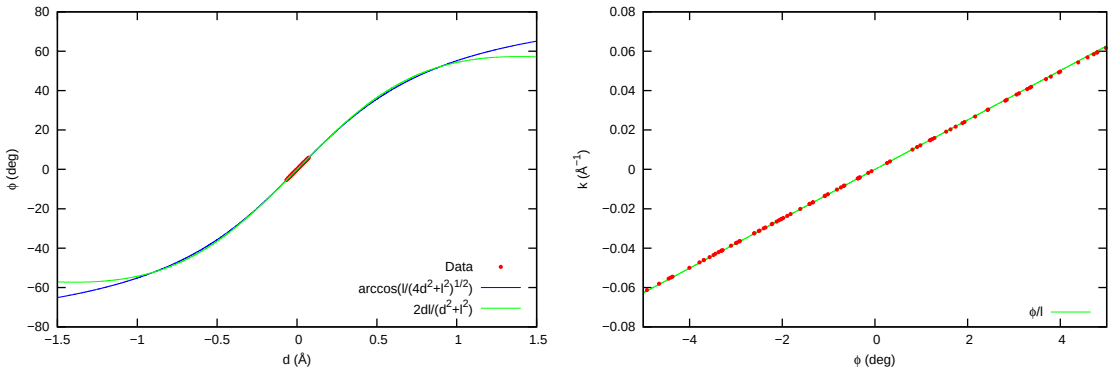

(a) (b)

Figure 3.7: (a) Improper dihedral angle as a function of the height d. The exact and the approximated functions are reported. (b) Local curvature k_i as a function of the improper dihedral angle ϕ_i. (a) (b) All the data reported, in red, are from the the relaxed rippled cell at 2% compression.

The principal curvatures of Eq. 1.9 have the units of the reciprocal of length, hence it is useful to correlate the improper dihedral with a quantity with the same units. Using again d and l, the local curvature, indicated by k_i, can be redefined as the reciprocal of the sphere radius R_i that touches the i-th atom and its three neighbours. Like for the improper dihedral angle, also for the local radius there are three values per atom, one for each neighbour, and R_i is defined as their average value. By simple geometrical considerations:

$$R_i = \frac{l^2 + d^2}{2d} \tag{3.5}$$

For small improper dihedral angles, the local curvature k_i depends linearly on ϕ_i, as can be seen in Fig. 3.7(b):

$$k_i = \frac{2d}{l^2 + d^2} = \frac{\phi_i}{l} \tag{3.6}$$

The same dependence on the average ϕ^2 is expected for phenomenons that involve the bending. The average curvature k of a structure was calculated as the root of the average of the square local curvatures:

$$k = \sqrt{\frac{1}{N}\sum_{i=1}^{N} k_i^2} = \sqrt{\frac{1}{N}\sum_{i=1}^{N} \frac{1}{R_i^2}} \tag{3.7}$$

N is the number of atoms of the cell.

Clearly, in this way only a single local curvature is valuable, which is the average of the two principal ones. Thus a simplified formula with respect to the Eq. 1.9 must be used to relate curvature and electric field:

$$k(F) = \eta F \tag{3.8}$$

where η is the ratio between the flexoelectric constant f and the bending stiffness, and it is the parameter that was evaluated in this work.

3.1.6 Computational resources

Two different computing systems were used to perform the simulations. Test and lighter calculations (basically those on unit cell) were performed on local 12 cores workstations. Heavier calculations were performed using the FERMI supercomputer at CINECA, one of the most powerful in the world and the most in Italy, which exploits a massive parallelization[50]. FERMI is a IBM BlueGene/Q system composed by 10 240 PowerA2 compute nodes each with 16 GB of RAM and 16 cores that work at 1.6 GHz, for a total of 163 840 cores and a peak performance of 2.1 PFlop/s.

The starting of a simulation on FERMI means enter into a queue whose position is determined according to the computational resources required, namely the number of nodes and the simulation time, that must be setted in advance following the default classes. The computational resources are obtained through grants upon presentation of a specific project subject to peer review.

3.2 Results

3.2.1 Free standing pure graphene

The free standing pure graphene was simulated with the unit cell and the $4\sqrt{3} \times 4\sqrt{3}R30$ cell, and in the latter case with a flat and a rippled structure. A study on the lattice constant for the $4\sqrt{3} \times 4\sqrt{3}R30$ flat cell was made (details in App. C). The minimum of the cohesive energy is at a value of 16.9914 Å, corresponding to a C-C bond lenght of 1.4160 Å. The cohesive energy per atom at this lattice constant is -8.4753 eV. For the flat graphene, the lattice vector lenght of 17.04 Å was finally used.

The optimized structure of rippled graphene compressed at 2% is reported in Fig. 3.8 and its cohesive energy per atom is -8.7670 eV. The STM-like images are reported in Fig. 3.9. As it can be seen, they show a quantitative agreement with those of Fig. 1.9.

The electronic structure of the flat and rippled systems are shown in Fig. 3.10. A comparison between the bands of the flat unit cell with that of the flat $4\sqrt{3}\times4\sqrt{3}R30$ cell (panels (a) and (b)) clearly shows the refolding (with multiplication of the bands) and consequent remapping of the Dirac point in Γ. Conversely, the DOS (panels (d) and (e)) coincide within the numerical error, as expected since the two systems physically coincide and must have the same electronic structure.

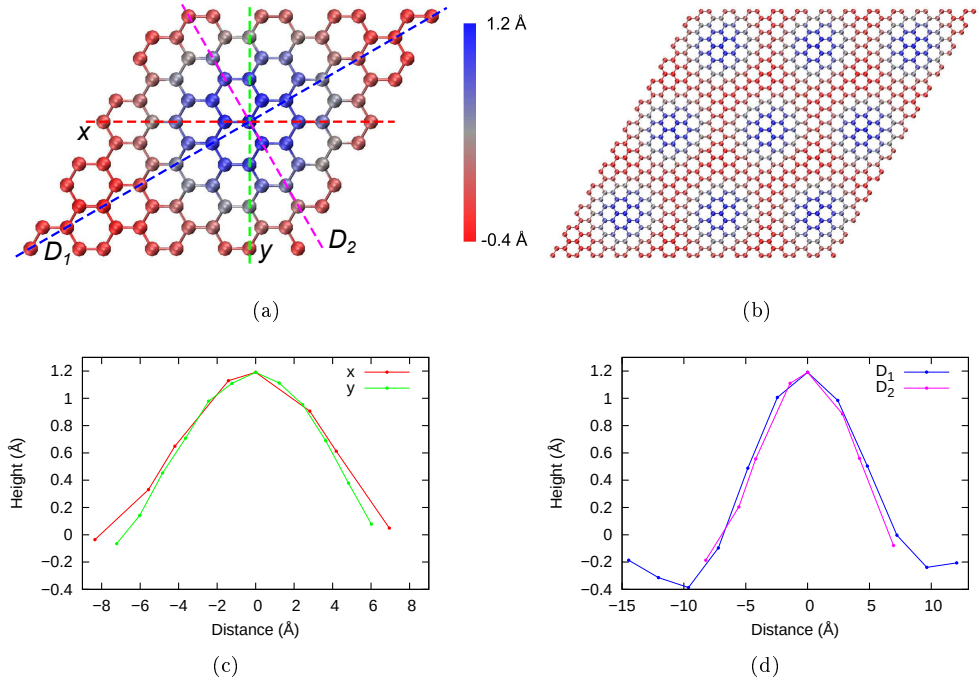

Figure 3.8: (a) Top view of the optimized ripple structure. (b) Top view of same structure with eight periodic copies. The color scale indicates the different heights of the atoms, red for the lower, blue for the higher. (c) Atoms height along the x and y paths indicated in (a). (d) Atoms height along the two diagonals, as indicates in (a).

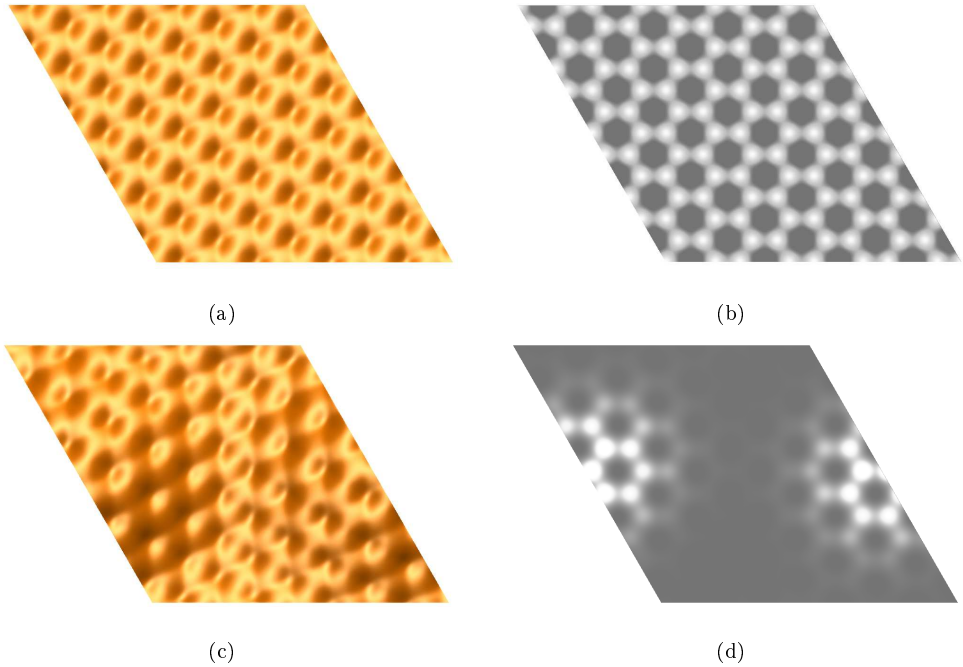

Figure 3.9: (a) Total electronic density and (b) STM simulated image of the flat $4\sqrt{3} \times 4\sqrt{3}R30$ cell. (c) Total electronic density and (d) STM simulated image of the rippled $4\sqrt{3} \times 4\sqrt{3}R30$ cell. Isovalue set to 0.001 Bohr^{-3}.

The comparison between the panels (b) and (c), and (e) and (f), shows the effect of the rippling on the electronic structure. The first observation is that the system does not show appreciable band gap opening at this small rippling level (while it is known that it happens at higher bending levels[49]), thus preserving the peculiar graphene electronic properties. It can be observed, however, a small band splitting above 1.5 eV and below −1.5 eV, compatible with symmetry breaking. As a consequences, irregularities in the DOS can be seen (e.g. an "indentation" at about −6 eV).

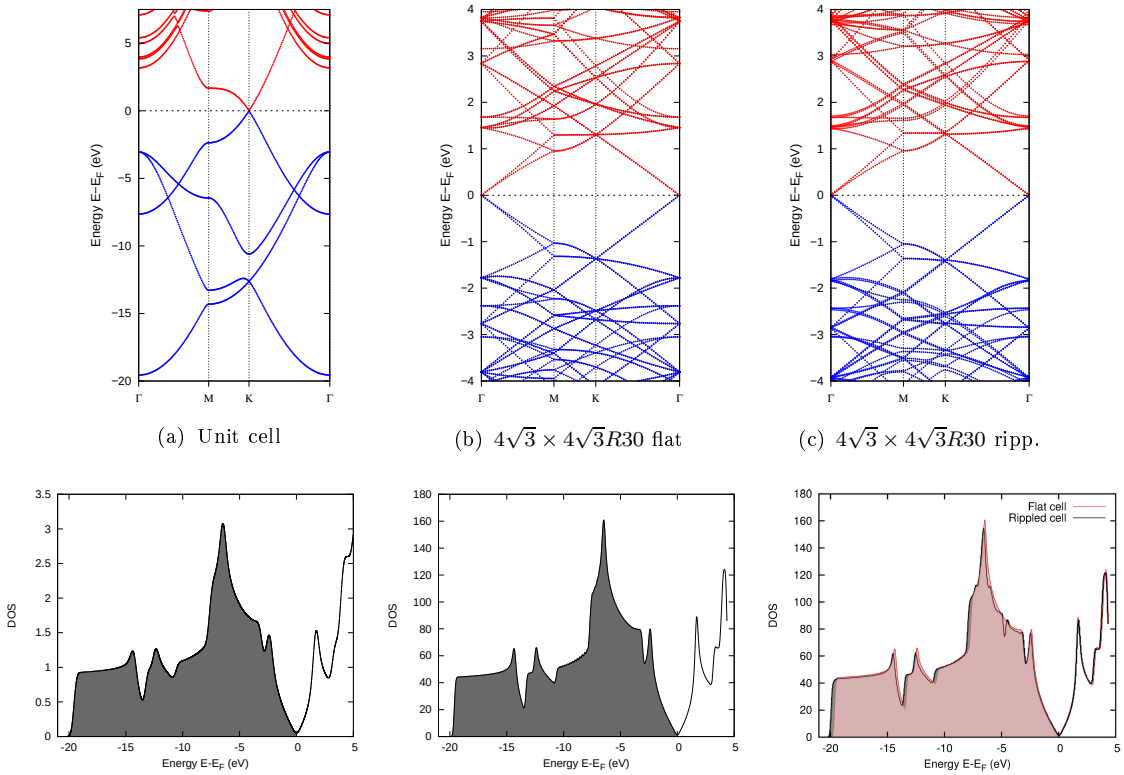

(a) Unit cell (b) $4\sqrt{3} \times 4\sqrt{3}R30$ flat (c) $4\sqrt{3} \times 4\sqrt{3}R30$ ripp.

(d) Unit cell (e) $4\sqrt{3} \times 4\sqrt{3}R30$ flat (f) $4\sqrt{3} \times 4\sqrt{3}R30$ rippled

Figure 3.10: (a) (b) (c) Band structure for (a) the unit cell, (b) the $4\sqrt{3} \times 4\sqrt{3}R30$ cell with flat structure and (c) the $4\sqrt{3} \times 4\sqrt{3}R30$ cell with rippled structure. The bands in blue are those below the Fermi energy, while the ones in red are above. (d) (e) (f) DOS for (d) the unit cell, (e) the $4\sqrt{3} \times 4\sqrt{3}R30$ cell with flat structure and (f) the $4\sqrt{3} \times 4\sqrt{3}R30$ cell with rippled structure in black overlapped to the equivalent flat structure in red.

3.2.2 Free standing graphene in electric field

The results of flat and rippled graphene in electric field are reported in this section. The electric fields are here allowed to vary in a wide range, reaching also very high values to quantitatively enhance the effects on the system, up to 40 GV/m, wich currently could be reached only with coherent electromagnetic radiations in the

THz range[51–53]. Due to the high value of the electric field, a preliminary study to determine over which threshold the system is ionized, was performed.

Ionization threshold of flat graphene

The study of the ionization threshold was performed by embedding the unit cell (two carbon atoms) in increasing electric fields up to 41.1 GV/m. The system remains flat so to separate the electronic from the structural changes due to the electric field. Data are reported in Tab. 3.4 and Fig. 3.11 and show a threshold above which the charge starts to be removed from graphene, which can be located at 6.7 GV/m. Above the threshold, the depleted charge increased linearly with the field, following the law $\delta(F) = \beta F + \delta_0$, with F the electric field (the fitted parameters are reported in Fig. 3.11). Non negligible values of the depleted charge (namely larger than 1%) are obtained for fields of the order of 10 GV/m. At the highest fields considered, the ionization level is ~ 0.09 e/atom.

F (GV/m)	q (e/atom)	δ
5.1	0	0
6.4	0	0
6.7	0.0000005	0.00000013
7.1	0.00172	0.000429
7.7	0.00380	0.000951
10.3	0.00950	0.00237
15.4	0.0233	0.00582
20.6	0.0371	0.00926
25.7	0.0505	0.0126
30.9	0.0636	0.0159
36.0	0.0763	0.0191
41.1	0.0886	0.0222

Table 3.4: Depleted charge per carbon atom, q, and ratio of depleted charge per electron, δ at different electric fields. Charges are measured in unit of e.

The energies per atom referred to the isolated atoms at null electric field, namely $E_f(F)$ as defined in Eq. 3.2, are reported in Tab. 3.5 and Fig. 3.12. From the analysis of these data, the polarizability of the system can be evaluated. To separate the simple polarizability from the ionization, the data are analysed separately below (Tab. 3.5(a)) and above (Tab. 3.5(b)) the threshold. Below the threshold, one can write:

$$E_f(F) = E_{coh} - \frac{1}{2}\alpha F^2 \tag{3.9}$$

where E_{coh} is the cohesive energy of the structure at null field and α is the polarizability. Using the data below the threshold, one can fit $\alpha = 5.41 \cdot 10^{-41}$ C $\cdot$ m^2/V $=$ 0.486 Å^3 (Fig. 3.12(a)), which is of the same order of magnitude of a previous theoretical estimate based on calculations of the graphene dielectric constant[54].

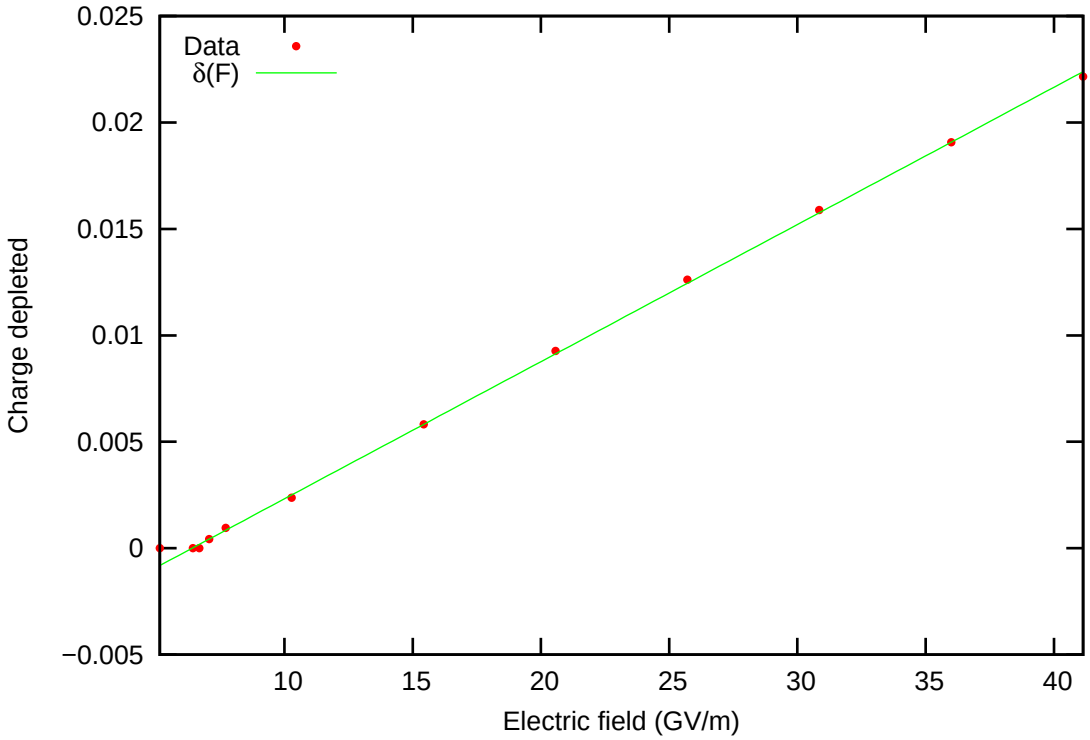

Figure 3.11: Graph of δ as a function of the electric field, with the same units of Tab. 3.4. Data in red, in green the fit curve. According to the law $\delta(F) = \beta F + \delta_0$, the parameter are fitted to $\beta = (6.44 \pm 0.04) \cdot 10^{-4}$ m/GV and $\delta_0 = (-0.00413 \pm 0.00009)$.

F (GV/m)	E_f (eV/atom)
0.0	−8.8169
0.5	−8.8169
1.0	−8.8170
1.5	−8.8173
2.1	−8.8176
2.6	−8.8180
3.1	−8.8185
3.6	−8.8191
4.1	−8.8197
4.6	−8.8205
5.1	−8.8213

(a)

F (GV/m)	E_f (eV/atom)
10.3	−8.9145
15.4	−8.9852
20.6	−9.1072
25.7	−9.2803
36.0	−9.7761
41.1	−10.0969

(b)

Table 3.5: Energies per atom at different electric field for the unit cell, (a) below and (b) above the ionization threshold. The energy E_f is calculated referring to the isolated atoms at null electric field.

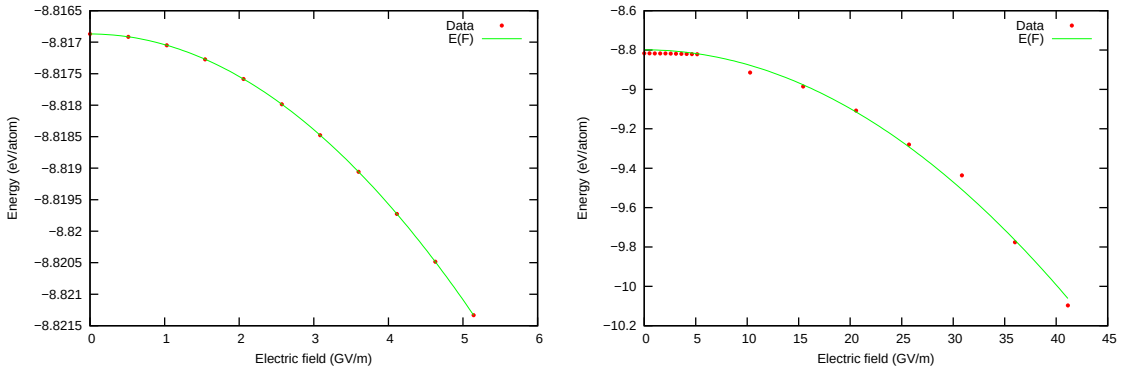

(a) (b)

Figure 3.12: Graph of the energy as a function of the electric field, (a) below and (b) above the ionization threshold. In the latter case also data below the threshold are reported, but not fitted. Data in red, fit curve in green.

Above the ionization threshold the picture is more complex. The removed charge δ accumulates at a distance $h_F/2$ from the graphene plane (see Fig. 3.13), producing a dipole and the corresponding polarization of amplitude $P_1(F) = 4e\delta(F)h_F$ (taking account the eight valence electrons of the unit cell). The ionized carbon atoms are also polarized, with a polarization that is $P_2(F) = \alpha_I(\delta)F$, where α_I is the polarizability of the ionized graphene that depends on the depleted charge δ. In first approximation α_I can be considered linearly dependent on δ, hence $\alpha_I(\delta) = \alpha + \gamma\delta(F)$. The energy E_f can be approximated as follow:

$$\begin{aligned} E_f(F) &= E_0 - \int_0^F [P_1(F') + P_2(F')]\,\mathrm{d}F' = \\ &= -\frac{1}{3}\gamma\beta|F|^3 - \left(\frac{\alpha+\gamma\delta_0}{2} + 2eh_F\beta\right)F^2 - 4eh_F\delta_0|F| + E_0 \end{aligned} \tag{3.10}$$

Since E_f is continuous at $\delta = 0$, one has $E_0 = E_{coh}$. Fitting the data (Fig. 3.12(b)), the value of $\gamma = -4.48 \cdot 10^{-38}$ C$\cdot$m^2/V $= -403$ Å^3 was obtained. This indicates that the polarizability decreases as the depleted charge increased. These empirical formulas can be used to separate the polarization from the ionization effects.

In Fig. 3.14 the effect of electric field on band structure is illustrated. At increasing fields, the empty bands are shifted downwards and the filled one upwards (though to a minor extent). A p-doping effect is clearly visible above the ionization threshold (panels (c) - (f)), as the Dirac point is shifted upwards with respect to the Fermi level.

A comparison of the electronic density at null field and with electric field, below and above the threshold, is reported in Fig. 3.13. Below the threshold the orbitals start to deform along the z direction for effect of the electric field, while above the deformation is very strong and a charge plane, formed by the removed charge that accumulates in the region where the electrostatic potential changes slope, appears, the blue line in Fig. 3.13(b).

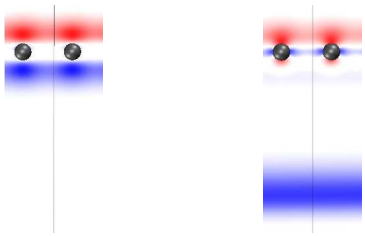

(a) (b)

Figure 3.13: (a) Difference of the total charge density between 5.1 GV/m and null field. (b) Difference of the total charge density between 36.0 GV/m and null field. In blue the areas where the there is more charge with the electric field, in red where there is lesser. The accumulation of charge at the cell boundary is visible as a blue band.

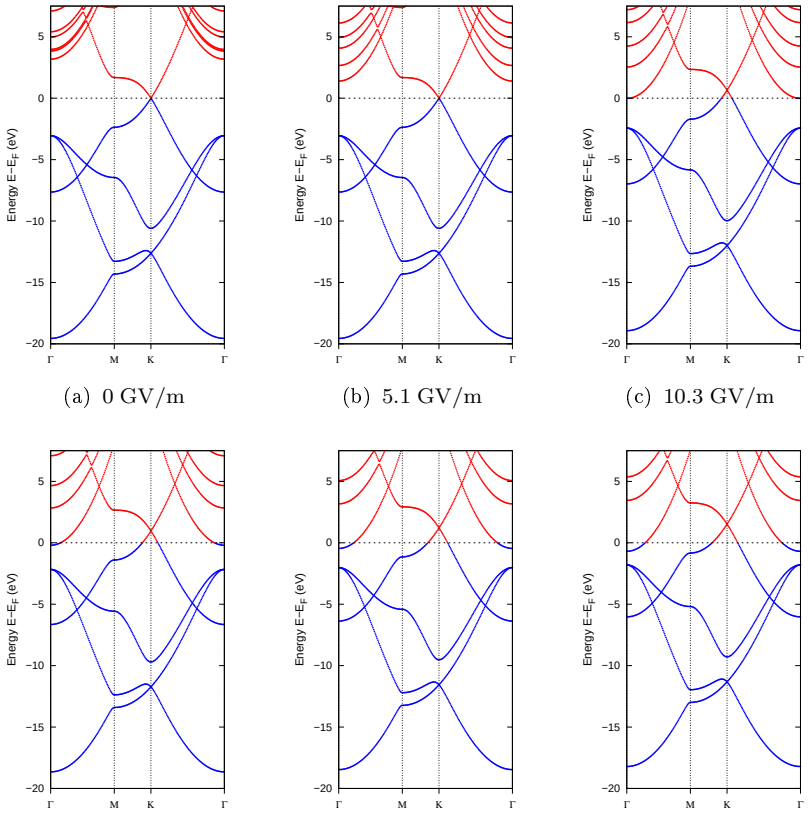

(a) 0 GV/m (b) 5.1 GV/m (c) 10.3 GV/m

(d) 15.4 GV/m (e) 25.7 GV/m (f) 36.0 GV/m

Figure 3.14: Band structures for the unit cell at different electric field values.

Hence, summarizing, below the threshold the electric field causes the deformation of the orbitals, while the bands structure remains almost unchanged, with the exception of the drop of the empty bands. Above the threshold, instead, much more charge is moved and the depleted charge causes a p-doping of the system, while other effects are accentuated at these electric field values.

$4\sqrt{3} \times 4\sqrt{3}R30$ cell at zero compression

Relaxations of the $4\sqrt{3} \times 4\sqrt{3}R30$ cell at zero compression with different electric fields, below and above the ionization threshold, were performed. The energy E_f and the average curvature k at different electric fields are reported in Tab. 3.6 and in Fig. 3.16. The structure starts to bend at about 4.9 GV/m.

F (GV/m)	E_f (eV/atom)	k (Å^{-1})
0.0	−8.7951	0
4.6	−8.7987	0
4.9	−8.7991	0.00000347
5.1	−8.7996	0.00000366
5.4	−8.8000	0.00000386
5.7	−8.8005	0.00000405
5.9	−8.8010	0.00000424
6.2	−8.8015	0.00000440
6.4	−8.8021	0.00000460
6.7	−8.8026	0.00000477
6.9	−8.8032	0.00000459
7.2	−8.8041	0.00000457
7.5	−8.8052	0.00000466
7.7	−8.8064	0.00000470
10.3	−8.8276	0.00000461
15.4	−8.9088	0.00000455
25.7	−9.2103	0.00000441
36.0	−9.6941	0.00002119

Table 3.6: Energy E_f and average curvature k at different electric field value for the $4\sqrt{3}\times4\sqrt{3}R30$ cell at zero compression.

As can be seen in Fig. 3.15, the curvature is initially opposite to the field direction, then at high electric field values it changes direction. This change in curvature happens over 15 GV/m, when the system is widely over the ionization threshold. Thus it is not an effect of the ionization. Rather, the relative instability of different curvatures could be interpreted as the interplay between the electric field and the in-plane translational symmetry, in the case of initially planar graphene. In fact, the electric field can only produce displacement of charges in the plane which will then be enhanced and generate ripples, but being translationally symmetric, it cannot determine the location of the ripples, and changing the location of a ripple, concavity with convexity might be inverted. The situation can change, of course, if a ripple is already present before the application of the field.

Observing the graph in Fig. 3.16(b), that reports the average curvature at different electric fields, it can be seen that the graphene, after starting to bend, increases linearly its curvature, as expected from flexoelectricity. Then, when the ionization threshold is reached, a new regime is entered and the curvature value is stabilized.

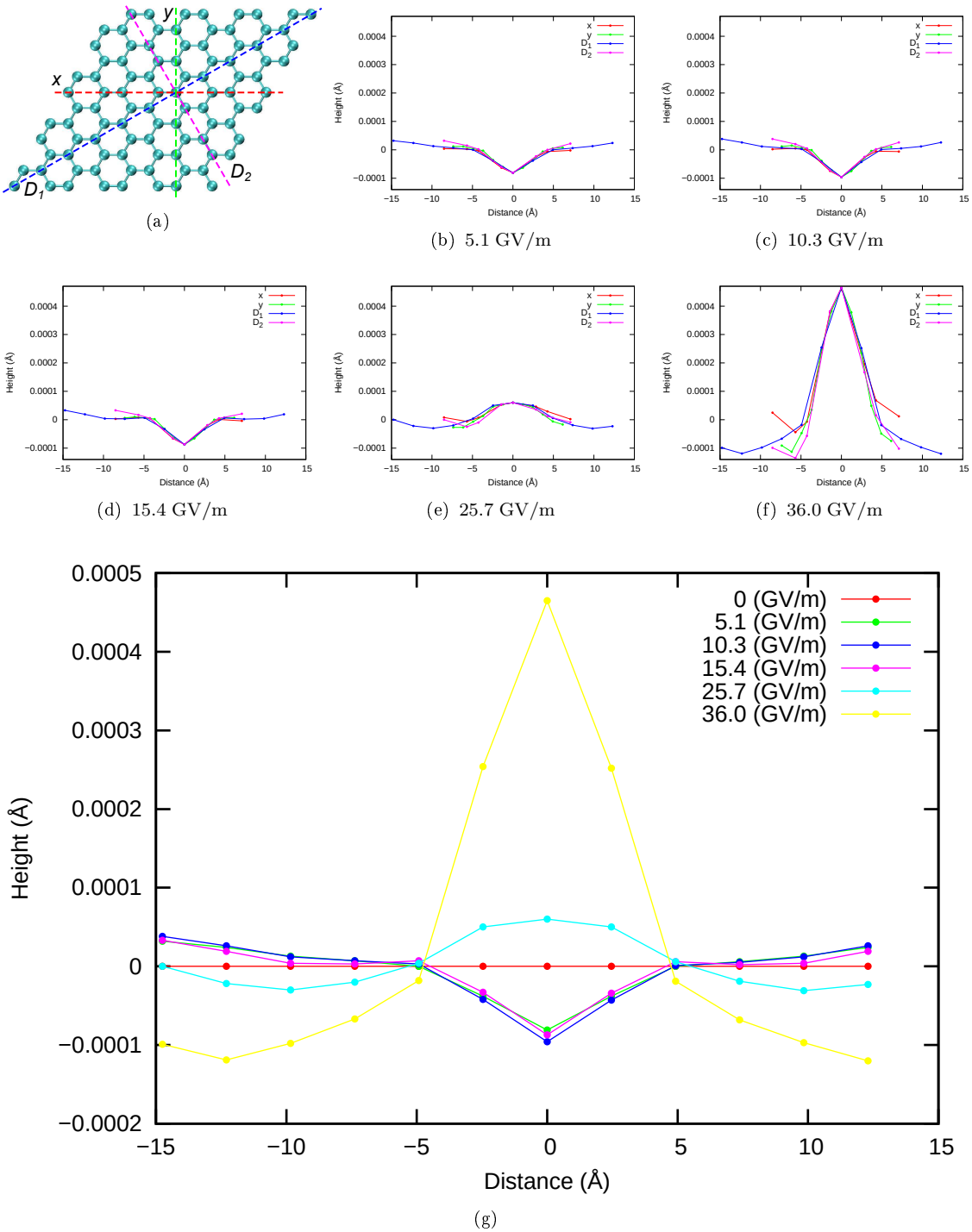

(a) (b) 5.1 GV/m (c) 10.3 GV/m

(d) 15.4 GV/m (e) 25.7 GV/m (f) 36.0 GV/m

(g)

Figure 3.15: Height of the atoms of the $4\sqrt{3}\times 4\sqrt{3}R30$ cell at zero compression. (a) Section lines x, y, D_1 and D_2, passing through the atom on top of the curvature, along which the height of the atoms were plotted. (b) (c) (d) (e) (f) Height of the atoms along the lines x, y, D_1 and D_2. (g) z coordinate of the atoms along D_1 for different electric field values.

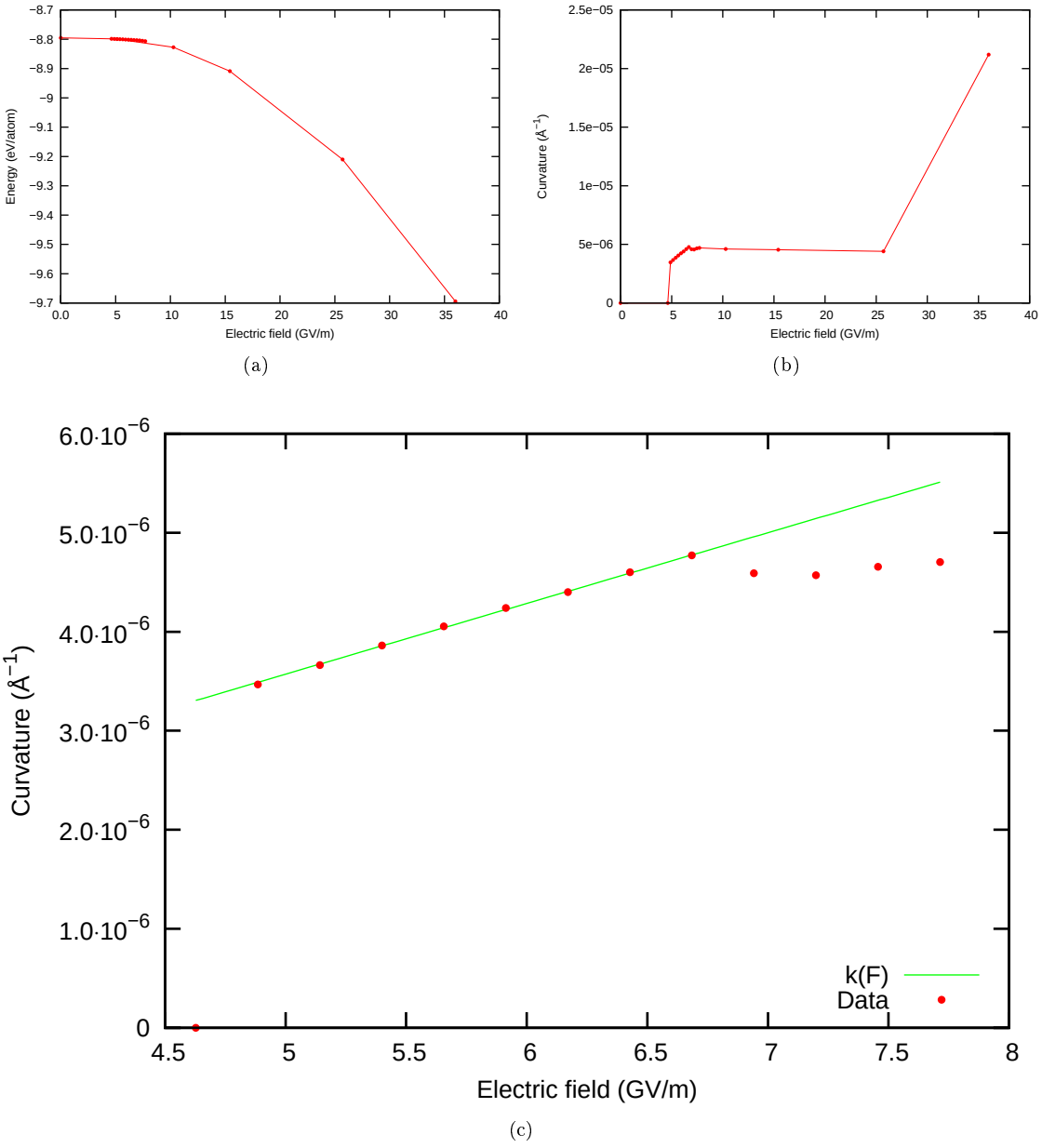

Figure 3.16: (a) Energy E_f referred to the atoms at null field and (b) average curvature k at different electric field values. (c) Zoom of the average curvature in the linear region, from the value of starting bend to the ionization threshold. The constant η was fitted in the linear region to $7.144 \cdot 10^{-6}$ C/N $\cdot$ m. In red the data, in green the fitting curve.

In this regime the evaluation of flexoelectricity is not simple because to the external field of the accumulated charge that must be considered. Finally at 36.0 GV/m the curvature increases rapidly, a consequence of the direct effect of the electric field on a ionized structure.

Due to the change of electronic properties over the ionization threshold, the flexoelectric effect was evaluated for electric fields below this value. In Fig. 3.16(c)

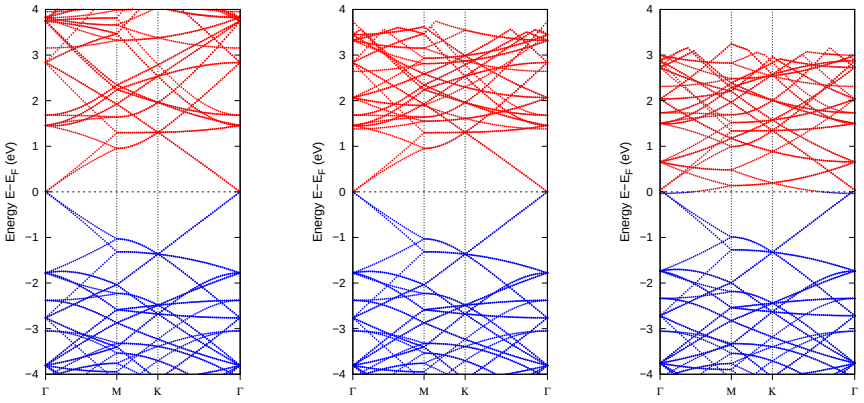

(a) 0 GV/m (b) 5.1 GV/m (c) 10.3 GV/m

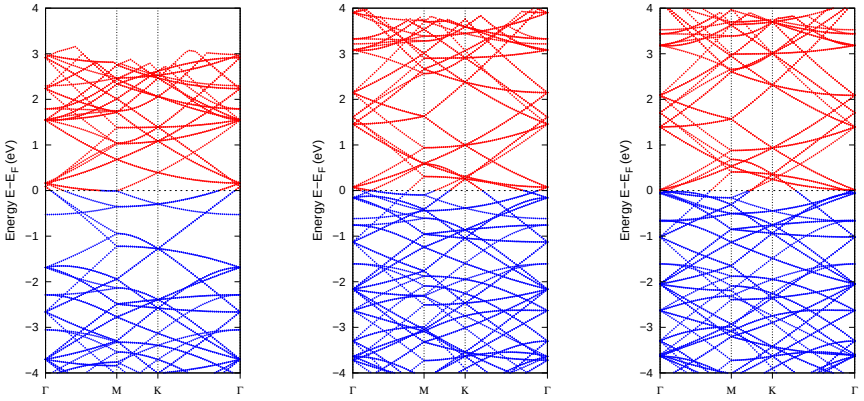

(d) 15.4 GV/m (e) 25.7 GV/m (f) 36.0 GV/m

Figure 3.17: Band structures for the $4\sqrt{3} \times 4\sqrt{3}R30$ cell at zero compression at different electric field values. In blue the states below the Fermi energy, in red the states above.

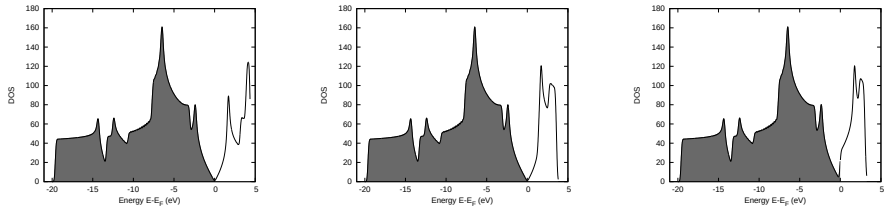

(a) 0 GV/m (b) 5.1 GV/m (c) 10.3 GV/m

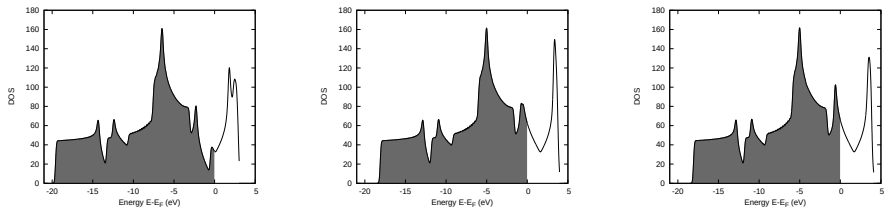

(d) 15.4 GV/m (e) 25.7 GV/m (f) 36.0 GV/m

Figure 3.18: DOS for the $4\sqrt{3} \times 4\sqrt{3}R30$ cell at zero compression at different electric field values.

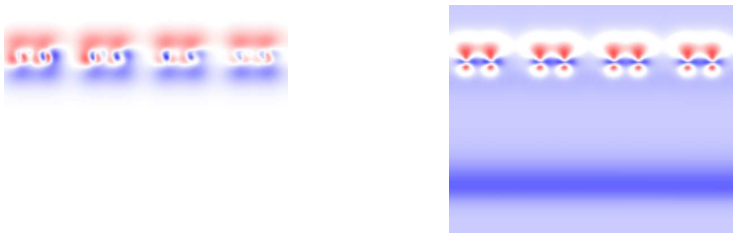

(a) (b)

Figure 3.19: (a) Difference of the total charge density between 5.1 GV/m and null field. (b) Difference of the total charge density between 36.0 GV/m and null field. Electronic charge accumulates in the blue areas.

the curvature at different electric field in a region near the ionization threshold is reported. Once the structure starts to bend, the curvature varies linearly with the electric field, as expected from the flexoelectric coupling. The flexoelectric constant η was fitted in the linear region, and for pure graphene was calculated as $7.144 \cdot 10^{-6}$ C/N $\cdot$ m. The bending stiffness of graphene has been evaluated by experimental and theoretical works[55,56] at about 0.2 nN $\cdot$ nm. Hence the value of the flexoelectric constant can be evaluated as $f = 1.43 \cdot 10^{-24}$ C $= 8.9 \cdot 10^{-6}$ e. A previous theoretical work[24], based on the polarization of a graphene membrane at different bending, indicates a much larger value of the flexoelectric constant. The specific reasons of this discrepancy are currently under investigation. Besides the different setup of the calculation, it should be considered that in this case, as in many different real situations (e.g. the graphene on SiC) there are specific boundary conditions which induce specific ripples geometries and, consequently, might influence the value of flexoelectricity.

The effects of the electric fields on the electronic structure are reported in Fig. 3.17, for the band structures, and in Fig. 3.18 for the DOS. Due to the refolding, the band structure at high fields is pretty complex. The curvatures involved, also at the highest electric fields, are not large enough to have visible effects on the electronic structure, like the band splitting on the corrugated cell at null field. As said in the previous section, the electric field causes a p-doping over the ionization threshold, that is clearly visible in the DOS. The downward shift of the empty bands and the upward of the filled ones implies that the DOS no longer vanishes for electric fields values above 15.4 GV/m. In Fig. 3.19 the electronic charge displacement due to the electric field is reported, for fields below and above the threshold. The π orbitals deformation is clearly visible in the first case, while the depleted charge can be seen in the second one.

$4\sqrt{3} \times 4\sqrt{3}R30$ rippled cell

Starting from the relaxed structure at null field, the rippled $4\sqrt{3} \times 4\sqrt{3}R30$ cell at 2% compression was simulated at different electric fields. Due to the symmetry breaking along the z direction caused by the ripple, electric fields in both directions

were considered. The presence of the ripple implies that the structure is not perfectly centered on the cell, but it is shifted of ~ 0.25 Å upwards.

F (GV/m)	E_f (eV/atom)	k (Å^{-1})
−36.0	−9.6103	0.05766
−25.7	−9.1570	0.04608
−15.4	−8.8738	0.03841
−10.3	−8.7980	0.03840
−5.1	−8.7717	0.03840
0.0	−8.7670	0.03840
5.1	−8.7716	0.03841
10.3	−8.8043	0.03841
15.4	−8.8915	0.03842
25.7	−9.2105	0.04761
36.0	−9.7286	0.06068

Table 3.7: Energy referred to the isoalted atom at null field and average curvature at different electric field values for the rippled $4\sqrt{3} \times 4\sqrt{3}R30$ cell at 2% compression.

The energy E_f, referred to the atoms at null field, and the average curvature k are reported in Tab. 3.7 for different electric fields value, and they are plotted in Fig. 3.20. For both the quantities there is an asymmetry comparing positive and negative values of the electric field, as expected from the presence of the ripple. The average curvature is strongly enhanced at values above the ionization threshold, at least at ± 25.7 GV/m, while for lower values curvature modifications are small. In Fig. 3.20 the structure and their sections are reported. As can be seen, also at -36.0 GV/m the curvature is enhanced upwards, antiparallel to the field direction, contrary to what one could expect from a ionized structure. One possible explanation is the electrostatic interaction with the removed charge that attracts graphene upwards.

The analysis of flexoelectricity in already corrugated graphene is not straightforward, because one has to redefine the flexoelectric coefficient in terms of the variation of curvature, rather than in terms of the curvature itself. In addition, due to the z symmetry breaking, this must be done for positive and negative fields separately. The results are reported in Fig. 3.20(c). The data were fitted separately for positive and negative fields under the threshold, with a formula of the form $k(F) = aF^2 + bF + k_0$. For positive electric field, the parameters were fitted to $a_+ = 5.58 \cdot 10^{-15}$ C^2/N$^2 \cdot$m, $b_+ = -5.09 \cdot 10^{-6}$ C/N$\cdot$m and $k_0^+ = 0.038396$ Å^{-1}, while for negative field to $a_- = 1.22 \cdot 10^{-15}$ C^2/N$^2 \cdot$m, $b_- = 3.70 \cdot 10^{-6}$ C/N$\cdot$m and $k_0^- = 0.038394$ Å^{-1}.

In both cases, two regimes are identified. For positive electric field, the regime transition seems mainly due to ionization, while for negative field the picture is more complex, and structural modifications seems also involved. For both positive and negative electric fields, a quadratic function fits well the data, and this could be

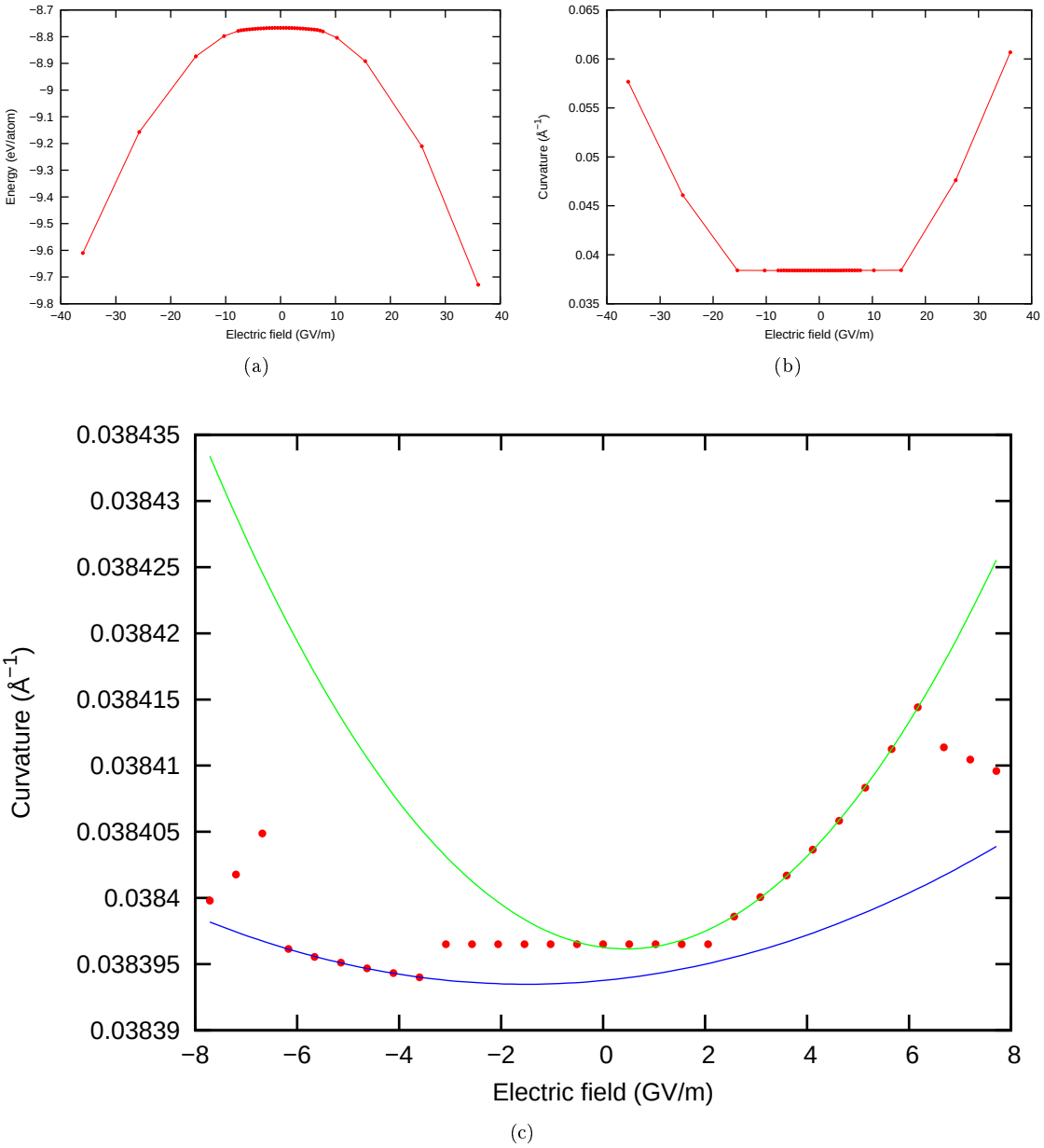

Figure 3.20: (a) Energy E_f and (b) average curvature k at different electric field values for the $4\sqrt{3} \times 4\sqrt{3}R30$ cell at 2% compression. (c) Curvature for electric field values below the ionization threshold. Data in red, fitting curve in green (positive fields) and blue (negative fields).

due to the starting curvature, that it is not null. Hence this is actually a second order effect of the curvature. This theoretical calculations could be experimentally checked, at least at medium-low electric fields.

The electronic density and the STM simulated images are shown in Fig. 3.22 at a values of 5.1 GV/m, below the ionization threshold, and 36.0 GV/m, above the threshold. The electric field removes charge mainly around the upwards curved points of the surface, where the corresponding orbitals are emptied. For the 36.0 GV/m

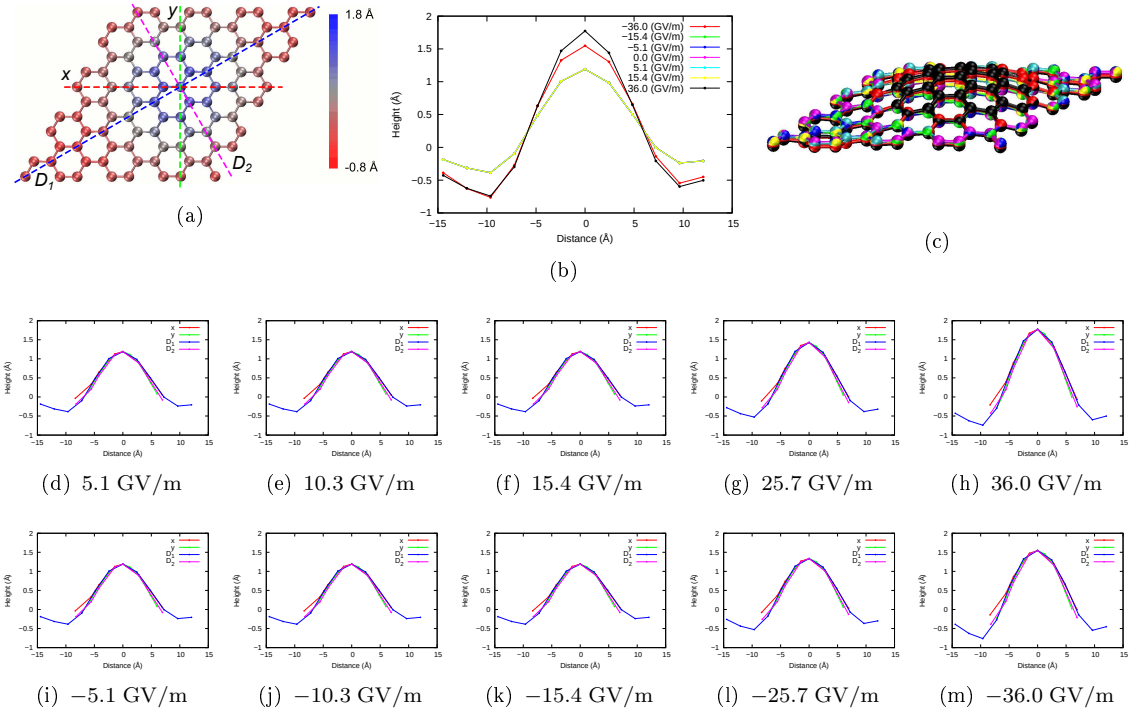

Figure 3.21: (a) Definition of the x, y, D_1 and D_2 lines along which the height of the atoms is shown. (b) Atom heights along the line D_1 for different electric field values. (c) Overlap of different structures at different electric field values. (d) - (m) Atom heights along the line x, y, D_1 and D_2 for different electric field values.

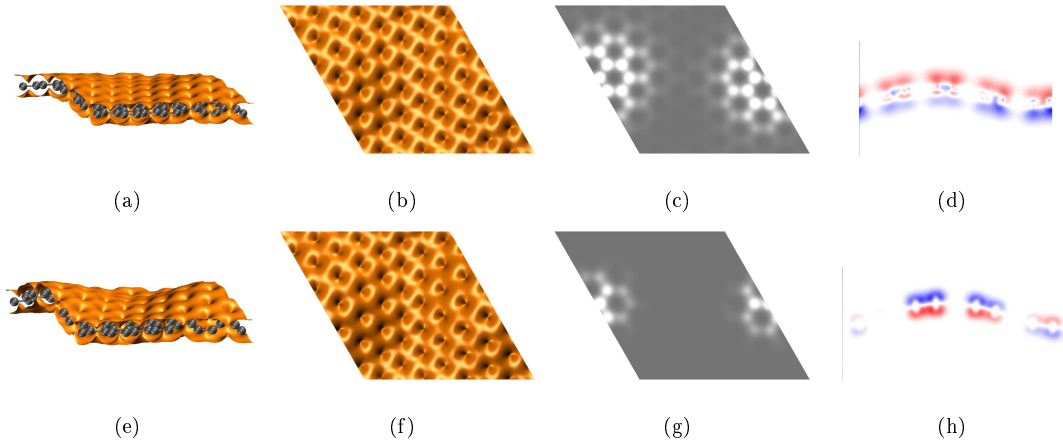

Figure 3.22: (a) (b) Side and top view of the total electronic density and (c) STM simulated image for the $4\sqrt{3} \times 4\sqrt{3}R30$ cell at 2% compression at 5.1 GV/m. (d) Difference of the total charge between 5.1 GV/m and null field; in blue the zones where more charge is present with the field, vice versa for red. (e) (f) Side and top view of the total electronic density and (g) STM simulated image for the $4\sqrt{3} \times 4\sqrt{3}R30$ cell at 2% compression at 36.0 GV/m. (d) Difference of the total charge between 36.0 GV/m and null field; the red background is due to the removed charge. Isovalue at 0.02 Bohr^{-3}.

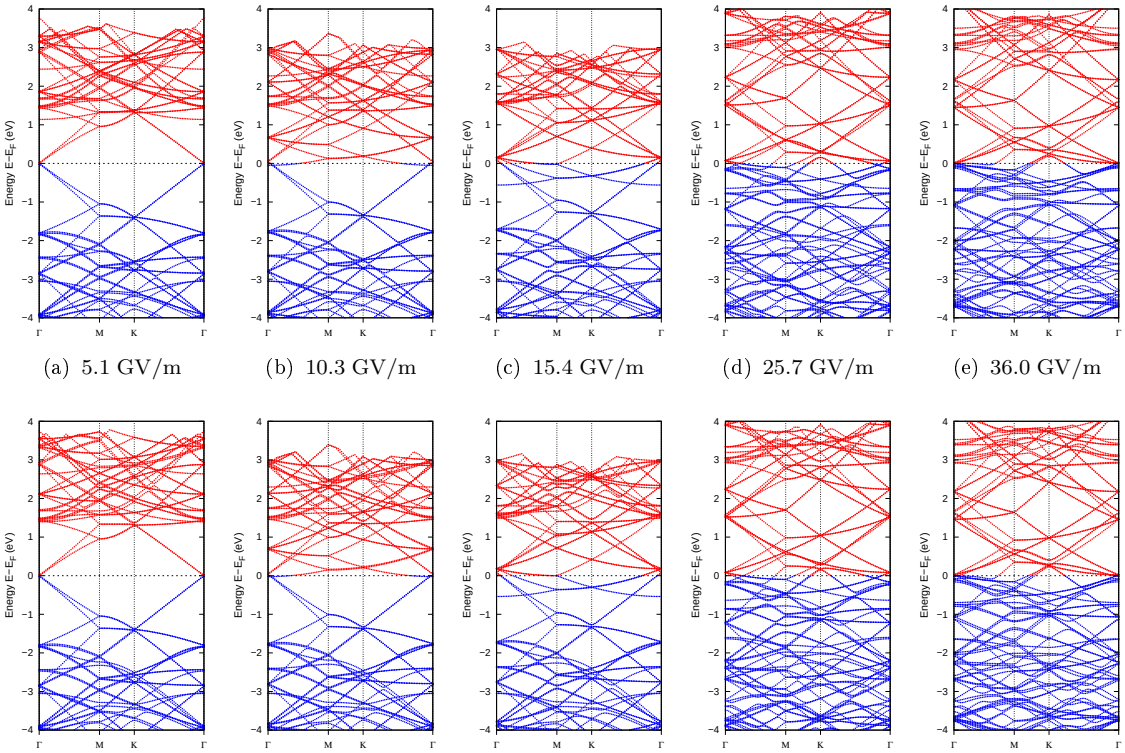

(a) 5.1 GV/m (b) 10.3 GV/m (c) 15.4 GV/m (d) 25.7 GV/m (e) 36.0 GV/m

(f) −5.1 GV/m (g) −10.3 GV/m (h) −15.4 GV/m (i) −25.7 GV/m (j) −36.0 GV/m

Figure 3.23: Band structures at different electric field values for the $4\sqrt{3} \times 4\sqrt{3}R30$ cell at 2% compression.

case, the charge difference depends mainly on the change of the atom locations due to the altered structure.

The electronic structure is reported in Fig. 3.23 and in Fig. 3.24, for the bands and DOS respectively. To the electric field effect to the band structure, the one of the curvature is added, especially at the highest fields, where also the curvature is higher. Comparing the bands near the Fermi energy for opposite values of electric fields, it can be noted that these bands, for positive values, are slightly lower. This is due to the removed charge, that is less for negative field values, an effect of the asymmetric curvature along z. Observing the DOS, in addition to the p-doping effect, it is visible a series of peaks, not present at low field values, caused by the curvature. At the highest fields, where the curvature is strongly enhanced, this effect is clearly visible. The results here shown could be directly compared with direct STM measurements of the electronic properties of the monolayer of graphene on SiC subject to electric field, because it has very similar ripples structure.

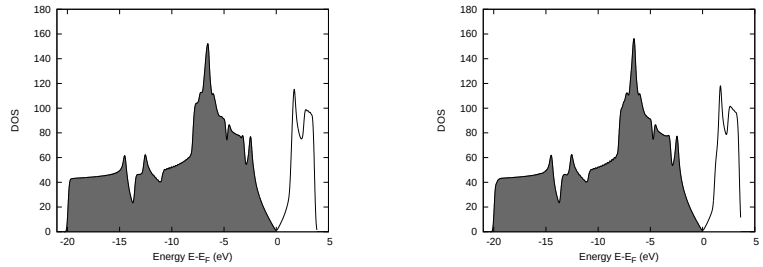

(a) −5.1 GV/m

(b) 5.1 GV/m

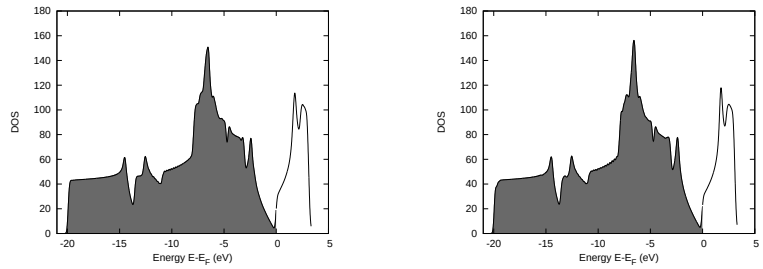

(c) −10.3 GV/m

(d) 10.3 GV/m

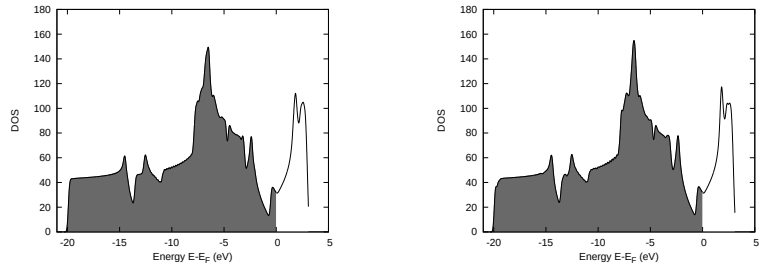

(e) −15.4 GV/m

(f) 15.4 GV/m

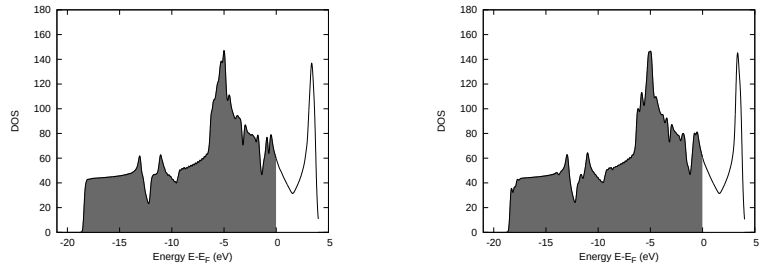

(g) −25.7 GV/m

(h) 25.7 GV/m

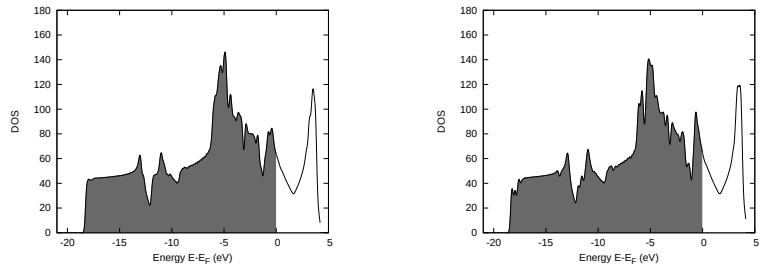

(i) −36.0 GV/m

(j) 36.0 GV/m

Figure 3.24: DOS at different electric field values for the $4\sqrt{3} \times 4\sqrt{3}R30$ cell at 2% compression.

3.2.3 Graphene on SiC

In this section the results of calculations of the graphene with its SiC substrate are reported. The system was simulated first with one layer of carbon atoms, to find the optimized structure of the buffer layer. Then the graphene monolayer was added on top of the structure and a second relaxation was performed. Both systems are composed by more than a thousand atoms, making these calculations pretty heavy. As a consequence, a complete analysis of the flexoelectric properties was not possible as in the free standing layer. However, as said, free standing layer at 2% compression has a very similar structure to the monolayer on SiC, thus comparison between the two cases is possible.

Buffer layer

The structure described in Sec. 3.1.1 with only the buffer layer was relaxed at null field. The optimized structure is shown in Fig. 3.25. The mean distance between the SiC surface and the buffer layer is 2.34 Å. The lattice structure is similar to the one shown in Sec. 1.2.1 with only minor differences on the maximum value of the vertical atom displacement.

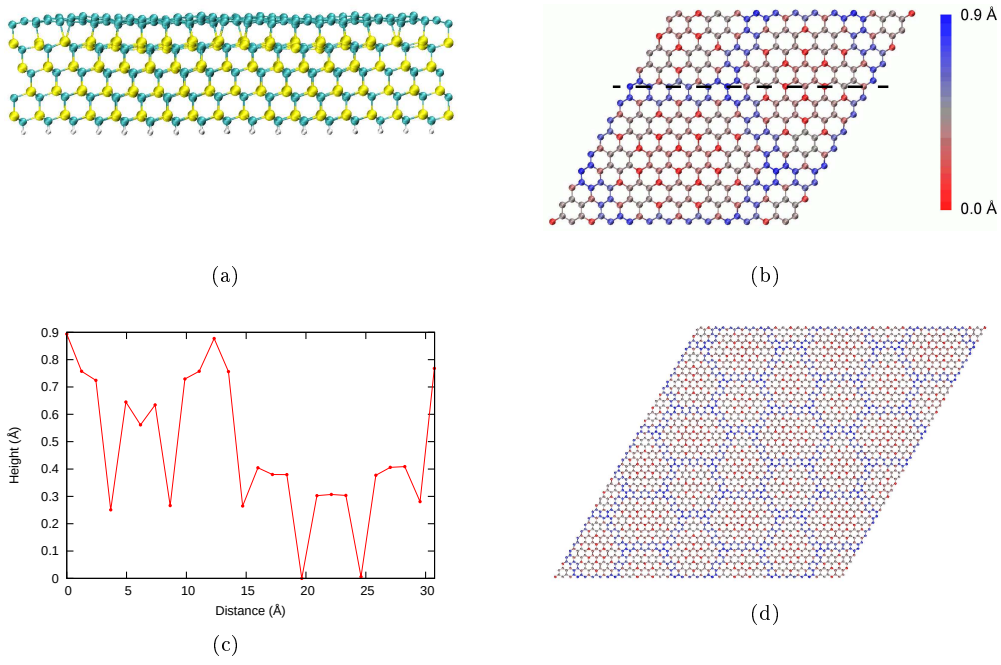

Figure 3.25: (a) Side view of the buffer layer structure: the ripples on the carbon layer are visible. (b) Top view of the buffer layer without the SiC substrate in color scale. (c) Heights of the atoms along the line indicated in (b). (d) Top view of the buffer layer with 8 periodic copies in color scale.

(a) (b) (c) (d)

Figure 3.26: (a) Side and (b) top view of the total charge density. (c) STM simulated image of the buffer layer. (d) Cross section of the total charge density: the color scale goes from red, where there is not charge, to blue, where the charge density is maxim.

In Fig. 3.26 the STM simulated image and the cross section of the total charge density are reported. In the latter case the charge is reported in color scale from blue, maxim density, to red, no charge. The buffer layer is represented by the blue charges on top of the structure. Observing the buffer layer it is possible to note the covalent bound of the lower carbon atoms by the downward deformed orbitals and the white charge linking the buffer layer to the substrate.

Graphene monolayer

On the relaxed buffer layer structure, a second carbon layer was added. The results of this structural optimization are shown in Fig. 3.27.

The mean distance between the buffer layer and the graphene layer is 3.27 Å, as previously found. The average curvature of the monolayer is 0.00709 $Å^{-1}$, as expected of the same order of that of the corrugated $4\sqrt{3} \times 4\sqrt{3}R30$ cell used in the calculations of the first part of this work. In Fig. 3.28 the STM simulated image and the total charge density cross section are reported. From the charge cross section it is clear visible that, differently from the buffer layer, the graphene monolayer is not covalently bound and its orbitals are almost unaffected by the presence of the substrate.

The symmetry of the ripples is also very similar to what expected. However, the analysis of the curvature reveals a first major difference with respect to previously reported data: the curvature is "inverted", namely wells separated by rippled are found, instead of hills separated by valleys. It is to be observed that in absence of z symmetry breaking, the two structures, namely the one found here and the one reported in the literature, would be degenerate in energy. The presence of the substrate breaks this symmetry, favoring one of the two. The one previously presented in the literature is the one with the opposite curvature, while here the optimization returned this one. One possible interpretation is that this one is as well a local minimum of energy. The question is if it is more or less stable with respect to the other. It is also to be observed that, as verified in the previous part of this work, the electric field modifies the curvature. Thus one possible way to obtain the alternative structure from this, is the application of an electric field.

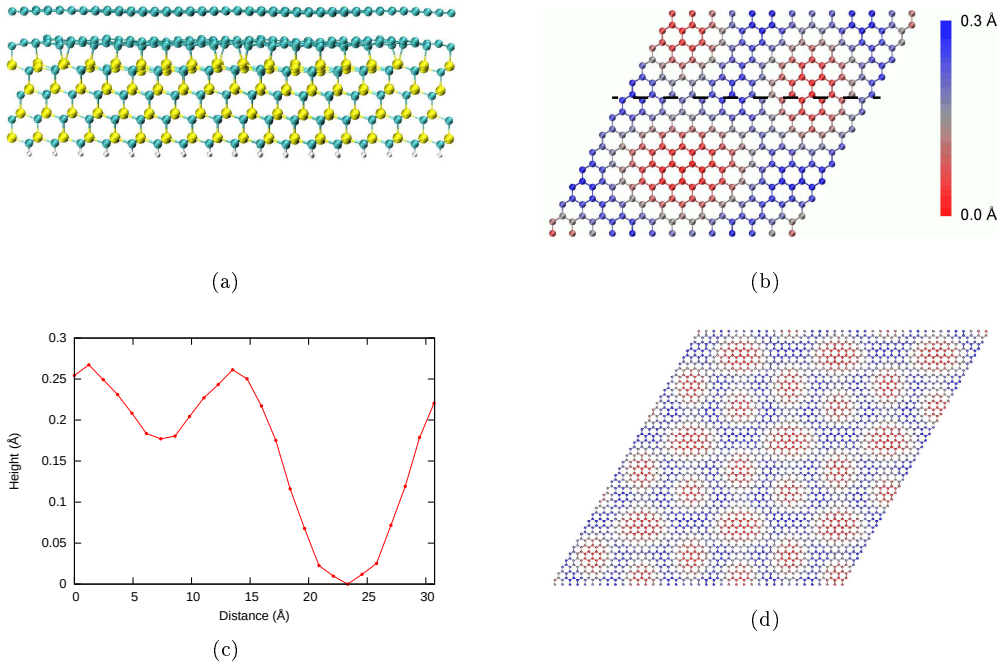

Figure 3.27: (a) Side view of the graphene on SiC: the ripples on the graphene and buffer layers are visible. (b) Top view of the graphene layer in color scale, without the SiC and buffer layer substrate. (c) Heights of the atoms along the line indicated in (b). (c) Top view of the graphene layer with 8 periodic copies.

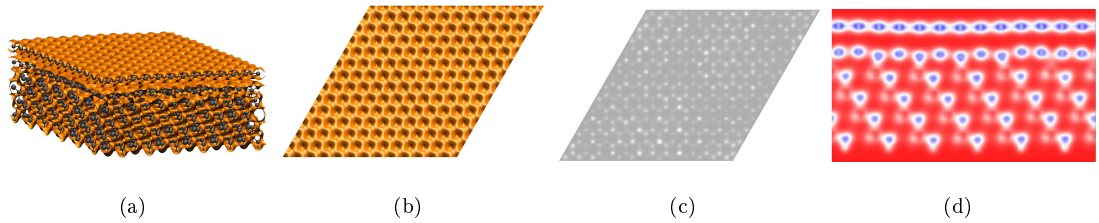

Figure 3.28: (a) Side and (b) top view of the total charge density. (c) STM simulated image of the graphene monolayer on SiC. (d) Cross section of the total charge density: the color scale goes from red, where there is not charge, to blue, where the charge density is maxim.

3.2.4 BN-Graphene

The BN-graphene system, described in Sec. 3.1.1, was simulated at zero compression and with 2% compression in the rippled structure, with and without electric field. The presence of two doping atoms makes that the electron density changes significally near these atoms compared to the pure graphene. In Fig. 3.29 is shown the difference of charge between pure and BN-doped graphene near the boron and nitrogen atoms. The graph, that reports the difference of charge in number of electrons and in absolute value, shown that the electron density is lower near B atom

and higher near N, as expected. The difference of charge exhibits fluctuations near the two atoms. As expected, the charges redistribute in order to screen the B and N atomic charges, which are -1 and $+1$ with respect to that of C, respectively. However this implies that electronic structures changes locally, with possible consequences on the flexoelectric properties.

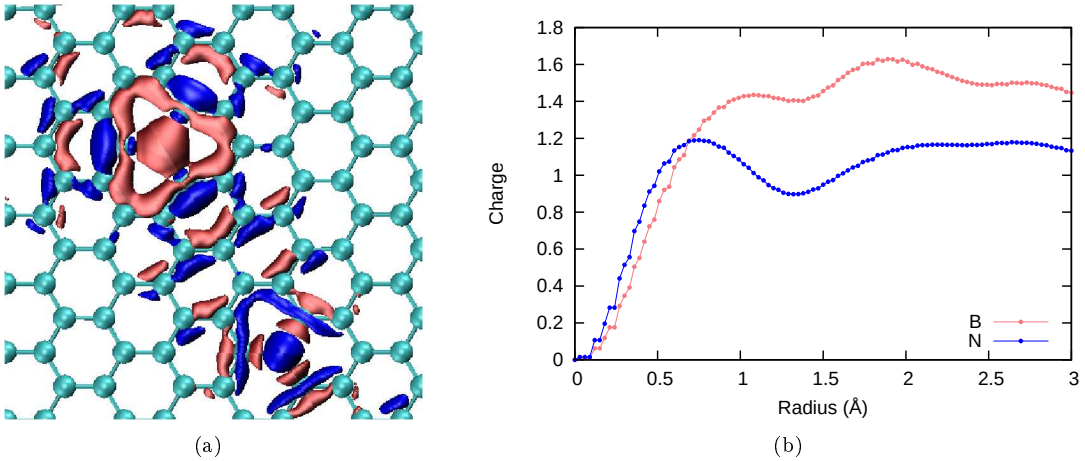

(a) (b)

Figure 3.29: (a) Charge difference around the B and N atoms respect to pure graphene, in pink and blue respectively. (b) Graph of the charge difference integrated at different radius.

$4\sqrt{3} \times 4\sqrt{3}R30$ cell at zero compression

The $4\sqrt{3} \times 4\sqrt{3}R30$ cell was relaxed at different electric field values. The energy E_f and the average curvature k are reported in Tab. 3.8. The structure starts to bend at 3.1 GV/m, a value about 2 GV/m lower than the one for pure graphene, which indicates an enhancement of the flexoelectric properties. Differently from pure graphene, in the BN-graphene the curvature is initially in the field direction, mainly due to the strong effect of the electric field on the boron atom. Then at about 15 GV/m, as can be seen in Fig. 3.30, the graphene-like behaviour emerges and the curvature changes direction, being opposite to the field; as for pure graphene, at about 36 GV/m the curvature changes direction again and it is strongly enhanced by the presence of the doping atoms.

In Fig. 3.31 the energy E_f and the average curvature are plotted. Below the ionization threshold two linear region for the curvature are visible. The first starts with the bending, while the second at the bending value of pure graphene: hence the first effect is due only to the doping atoms. Fitting the data, as reported in Fig. 3.31(c), the value of $\eta_1 = 5.739 \cdot 10^{-4}$ C/N $\cdot$ m was obtained for the first linear region. For the second region, a value of $\eta_2 = 1.873 \cdot 10^{-3}$ C/N $\cdot$ m and $k_0 = -2.1 \cdot 10^{-4}$ Å^{-1} (k_0 can be considered as the curvature at null field if it follows this law for all electric field values) were obtained. Using the bending stiffness of pure graphene, about 0.2 nN $\cdot$ nm, the flexoelectric constant are $f_1 = 2.87 \cdot 10^{-21}$ C $=$ 0.018 e for the first region, and $f_2 = 9.37 \cdot 10^{-21}$ C $=$ 0.058 e for the second region.

F (GV/m)	E_f (eV)	k (Å^{-1})
0.0	−839.76	0
2.6	−839.86	0
3.1	−839.91	0.00018
3.6	−839.97	0.00021
4.1	−840.03	0.00024
4.6	−840.10	0.00027
5.1	−840.18	0.00075
5.7	−840.27	0.00084
6.2	−840.37	0.00094
6.7	−840.48	0.00119
7.2	−840.63	0.00087
7.7	−840.85	0.00078
10.3	−842.88	0.00105
15.4	−850.71	0.00867
25.7	−879.97	0.01370
36.0	−927.87	0.04473

Table 3.8: Energy E_f, referred to the isolated atoms at null field, and average curvature k at different electric field value for the $4\sqrt{3} \times 4\sqrt{3}R30$ BN-graphene cell at zero compression.

As could be expected, the presence of the doping atoms enhances the flexoelectric coupling of about three orders of magnitude in the same region. Moreover the flexoelectricity manifests at lower electric field values, even if in minor amplitude.

Fig. 3.32 reports the total charge difference between the cell in electric field and at null field, for values of 5.1 GV/m, below the ionization threshold, and 36.0 GV/m, far above the threshold. The doping atoms and theirs neighbours are strongly affected by the electric field, with charge that mostly accumulates (and it is removed) below (above) the boron atom. For the 36.0 GV/m case, the charge difference is mainly due to the structural change that shift the atoms.

The electronic structure is strongly chacterized by the presence of the doping atoms. The π bands are splitted (Fig. 3.33) and at high electric field values the p-doping is effect is present, as a consequence of the ionization. In the DOS structure (Fig. 3.34) several peaks appear at all energy values and they are not correlated to the field intensity, as well as an isolated state at about −23 eV. Nevertheless, the conductive properties are not strongly modified, since the gap remains closed at these low doping levels.

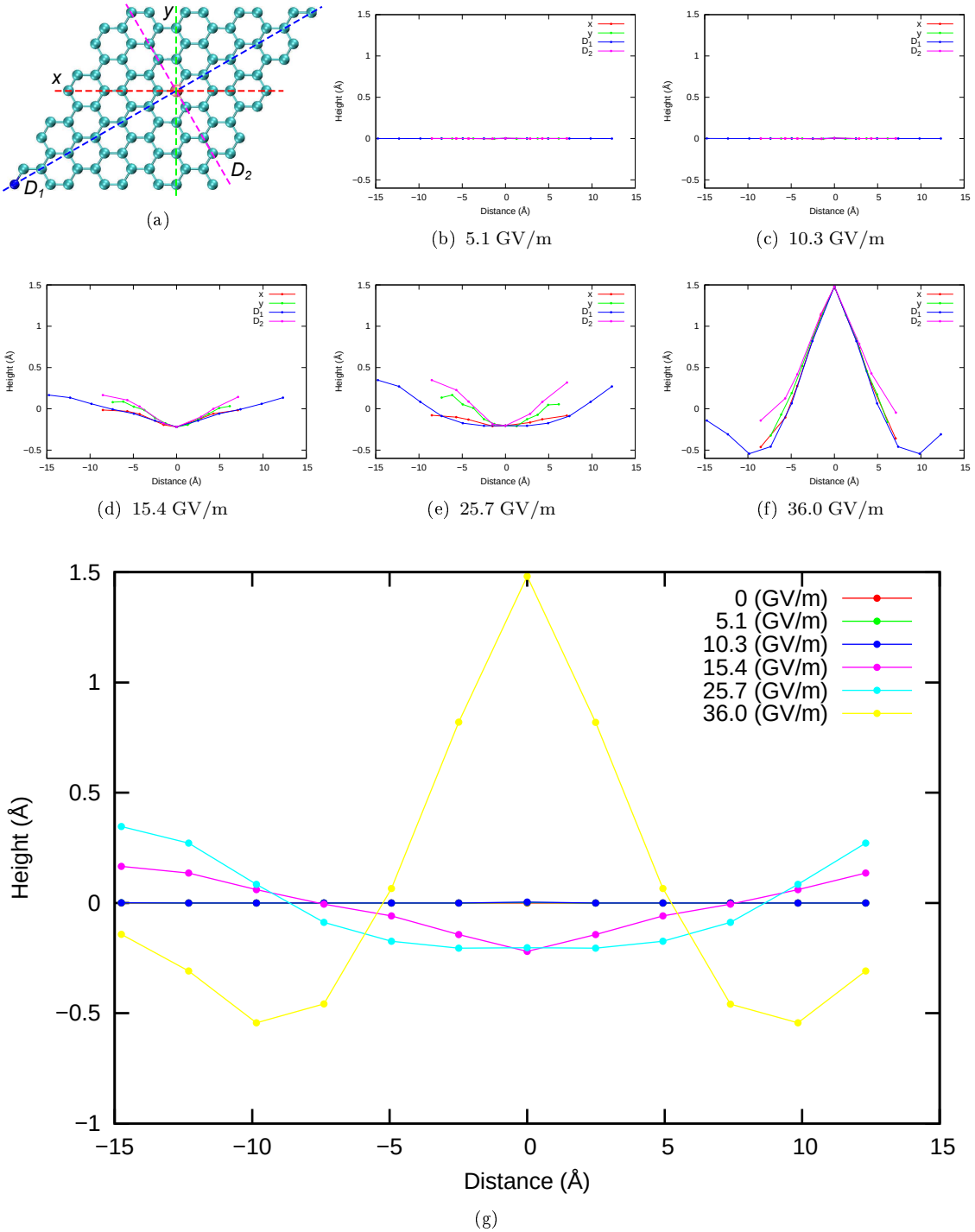

(a) (b) 5.1 GV/m (c) 10.3 GV/m

(d) 15.4 GV/m (e) 25.7 GV/m (f) 36.0 GV/m

(g)

Figure 3.30: Height of the atoms of the $4\sqrt{3} \times 4\sqrt{3}R30$ cell at zero compression. (a) Section lines x, y, D_1 and D_2, passing through the atom on top of the curvature, along which the height of the atoms were plotted. (b) (c) (d) (e) (f) Height of the atoms along the lines x, y, D_1 and D_2. (g) Height of atoms along the D_1 line at different electric field values.

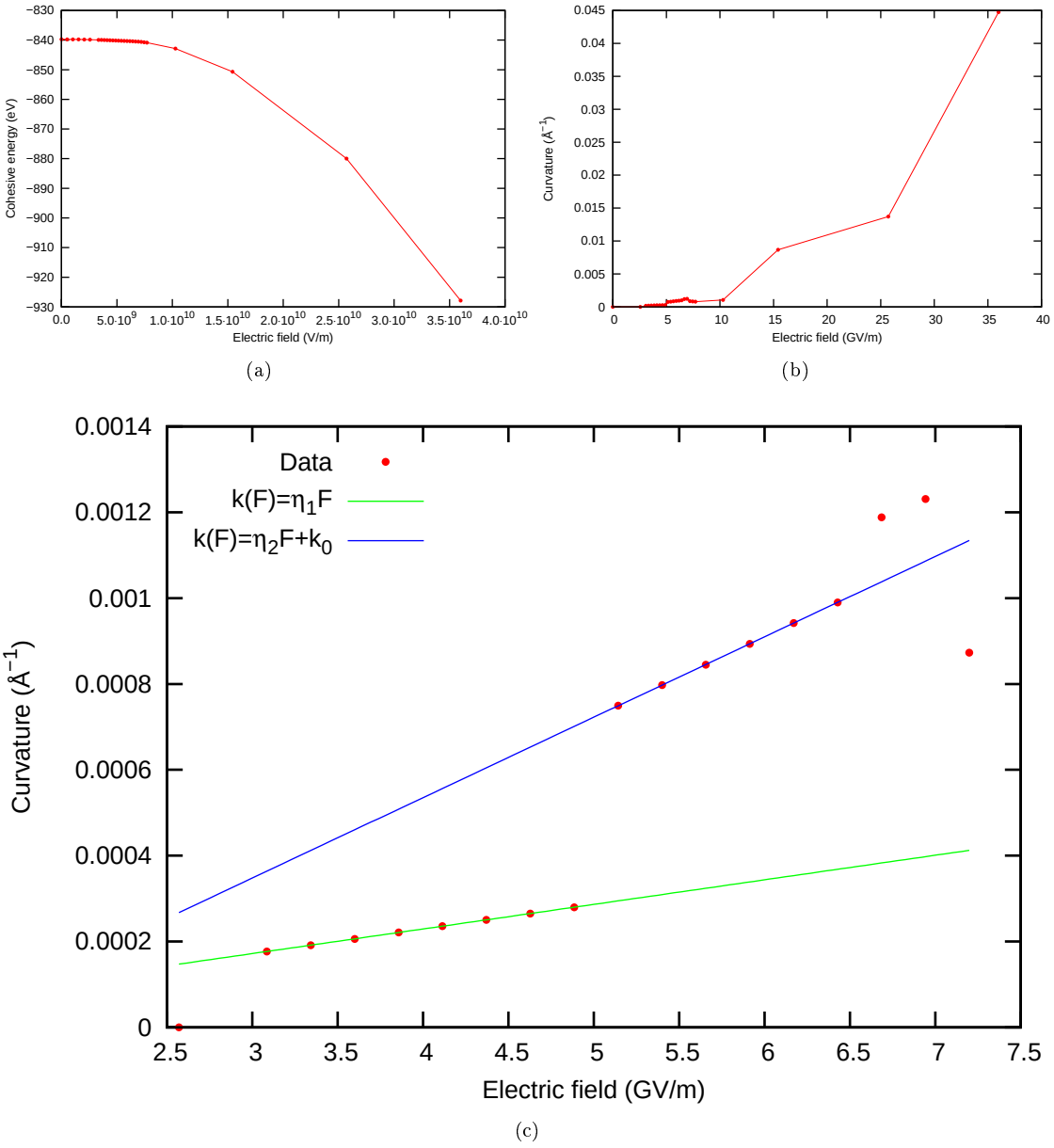

(a) (b)

(c)

Figure 3.31: (a) Energy E_f and (b) average curvature k at different electric field values. (c) Zoom of the average curvature near the ionization threshold.

(a) (b)

Figure 3.32: (a) Difference of the total charge density between 5.1 GV/m and null field. (b) Difference of the total charge density between 36.0 GV/m and null field. In blue the areas where the there is more charge with the electric field, in red where there is lesser.

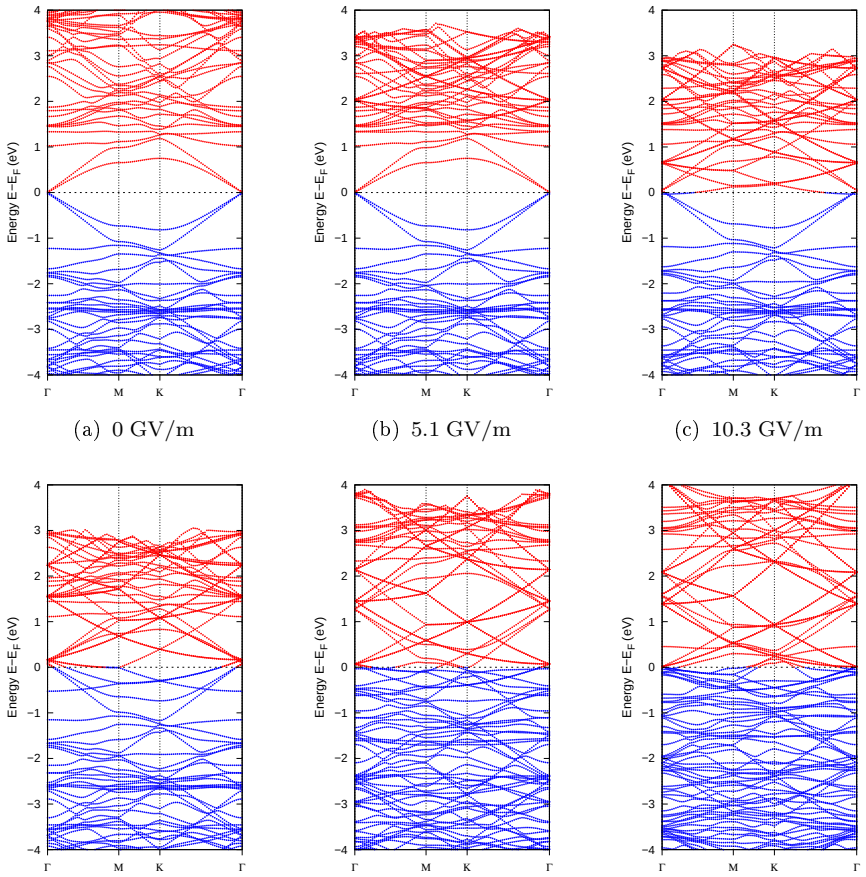

(a) 0 GV/m (b) 5.1 GV/m (c) 10.3 GV/m

(d) 15.4 GV/m (e) 25.7 GV/m (f) 36.0 GV/m

Figure 3.33: Band structures for the BN-doped graphene in the $4\sqrt{3} \times 4\sqrt{3}R30$ cell at zero compression at different electric field values.

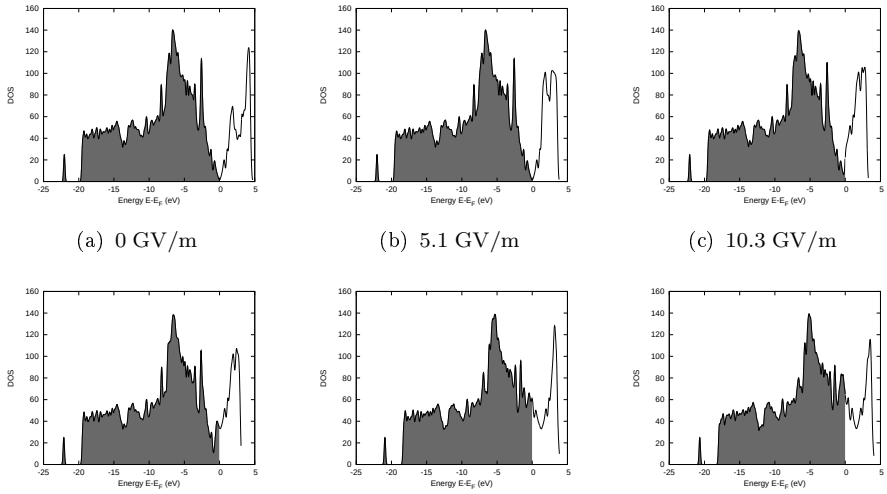

(a) 0 GV/m (b) 5.1 GV/m (c) 10.3 GV/m

(d) 15.4 GV/m (e) 25.7 GV/m (f) 36.0 GV/m

Figure 3.34: DOS for the BN-doped graphene in the $4\sqrt{3} \times 4\sqrt{3}R30$ cell at zero compression at different electric field values.

$4\sqrt{3} \times 4\sqrt{3}R30$ rippled cell

The BN-graphene was simulated in the $4\sqrt{3} \times 4\sqrt{3}R30$ rippled cell at 2% compression. Starting from the optimized structure of pure graphene at null field, the cell was relaxed at different electric field values. As for pure graphene, the electric field was implemented in both directions and the structure is shifted upwards of about 0.25 Å, due to the ripple presence.

F (GV/m)	E_f (eV)	k (Å^{-1})
−36.0	−919.41	0.06019
−25.7	−875.41	0.05069
−15.4	−847.89	0.04588
−10.3	−840.54	0.04469
−5.1	−837.96	0.04454
0.0	−837.39	0.04398
5.1	−837.74	0.04398
10.3	−840.87	0.04463
15.4	−849.26	0.04624
25.7	−880.47	0.05313
36.0	−931.65	0.06651

Table 3.9: Energy E_f, referred to the isolated atoms at null field, and average curvature k at different electric field values.

In Tab. 3.9 the energy E_f and the average curvatures are reported, while they are plotted in Fig. 3.35. Differently from the pure graphene, where the average

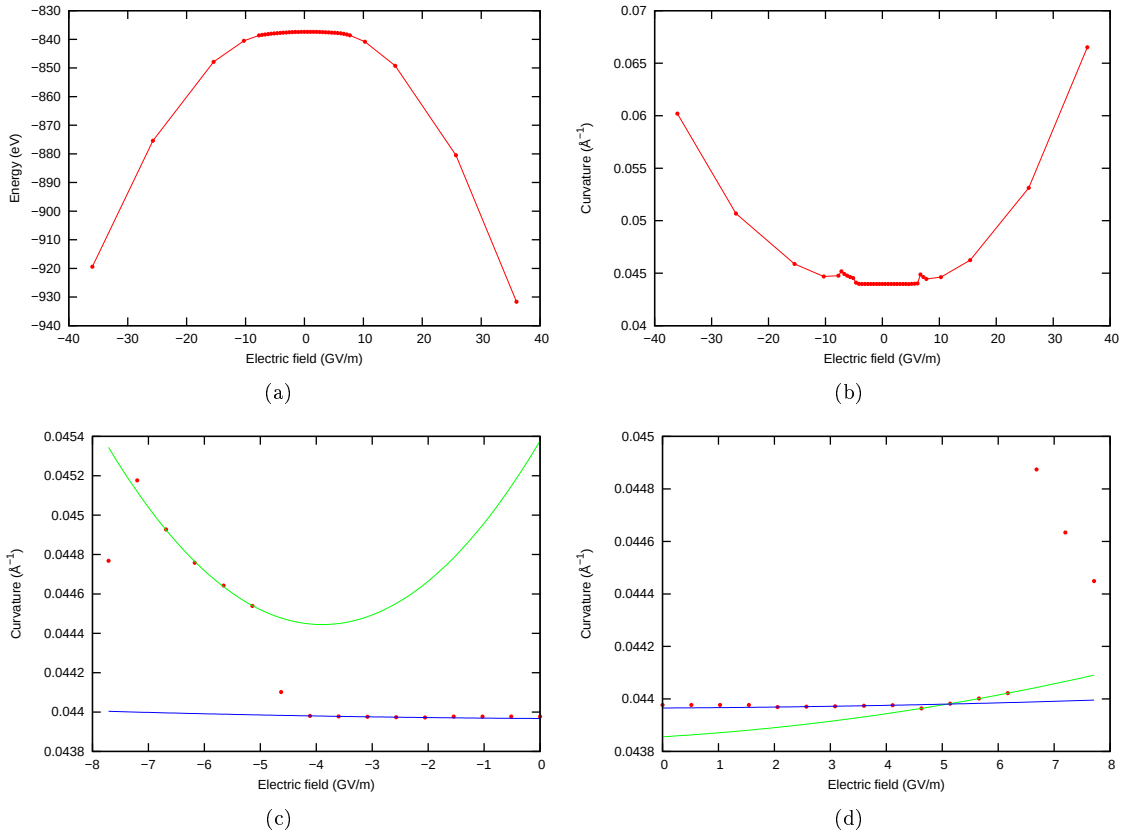

Figure 3.35: (a) Energy E_f and (b) average curvature at different electric field values. Curvature for negative (c) and (d) positive electric field values below the ionization threshold. Data in red, fitting curve in blue (first regime) and green (second regime).

curvature changes significally for electric fields over 15 Å, the structure shows alterations also at the lower field values implemented. The curvature is particulary strong around the boron atom, that strongly interacts with the electric field. The flexoelectricity was evaluated considering the curvature variation. The negative fields enhance more the curvature, and a double regime appears, as for the cell at zero compression, for both field directions. As for pure graphene, the flexoelectricity is a second order effect, and was fitted with a formula of the type $k(F) = aF^2+bF+k_0$. For negative electric fields, the parameters were fitted to: $a_1^- = 4.10 \cdot 10^{-15}$ C^2/N$^2 \cdot$m, $b_1^- = -1.55 \cdot 10^{-5}$ C/N$\cdot$m and $k_1^- = 0.04397$ Å^{-1} for the first regime, $a_2^- = 6.16 \cdot 10^{-13}$ C^2/N$^2 \cdot$m, $b_2^- = 0.00048$ C/N$\cdot$m and $k_2^- = 0.04538$ Å^{-1} for the second regime. For positive electric fields, instead, the parameters were fitted to $a_1^+ = 3.67 \cdot 10^{-15}$ C^2/N$^2 \cdot$m, $b_1^+ = -1.06 \cdot 10^{-5}$ C/N$\cdot$m and $k_1^+ = 0.04397$ Å^{-1} for the first regime, $a_2^+ = 2.28 \cdot 10^{-14}$ C^2/N$^2 \cdot$m, $b_2^+ = 1.29 \cdot 10^{-4}$ C/N$\cdot$m and $k_2^+ = 0.04386$ Å^{-1} for the second regime.

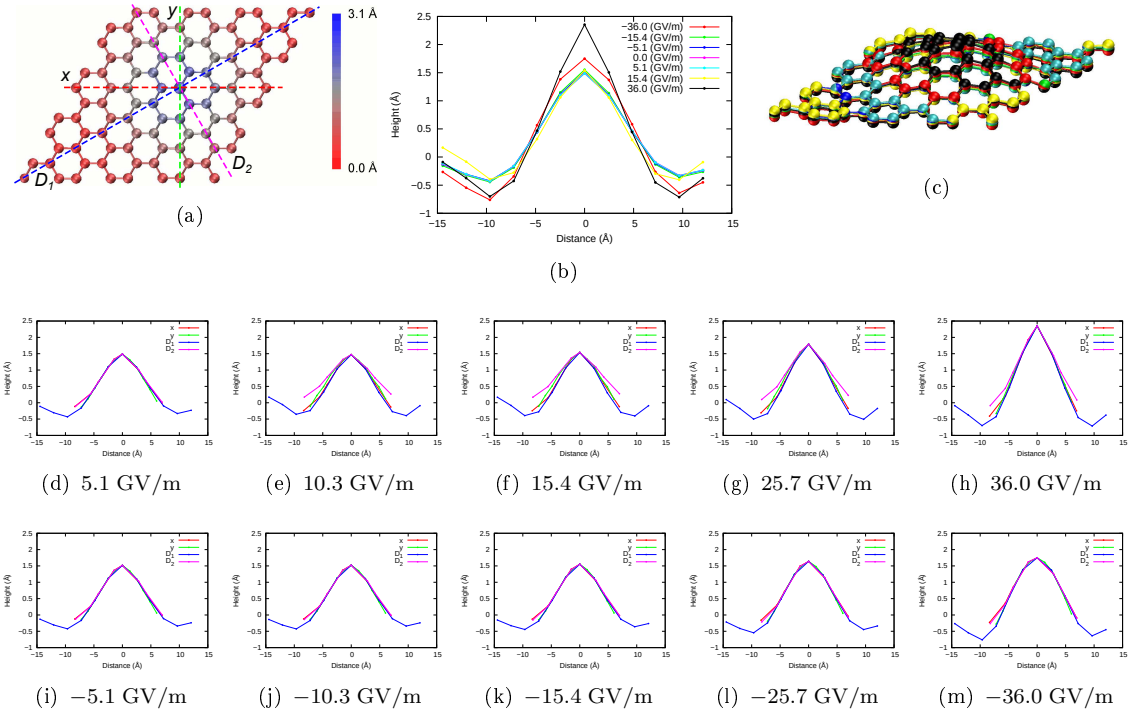

(a) (b) (c)

(d) 5.1 GV/m (e) 10.3 GV/m (f) 15.4 GV/m (g) 25.7 GV/m (h) 36.0 GV/m

(i) −5.1 GV/m (j) −10.3 GV/m (k) −15.4 GV/m (l) −25.7 GV/m (m) −36.0 GV/m

Figure 3.36: (a) Definition of the x, y, D_1 and D_2 lines along which the height of the atoms is shown. (b) Atom heights along the line D_1 for different electric field values. (c) Overlap of different structures at different electric field values. (d) - (m) Atom heights along the line x, y, D_1 and D_2 for different electric field values.

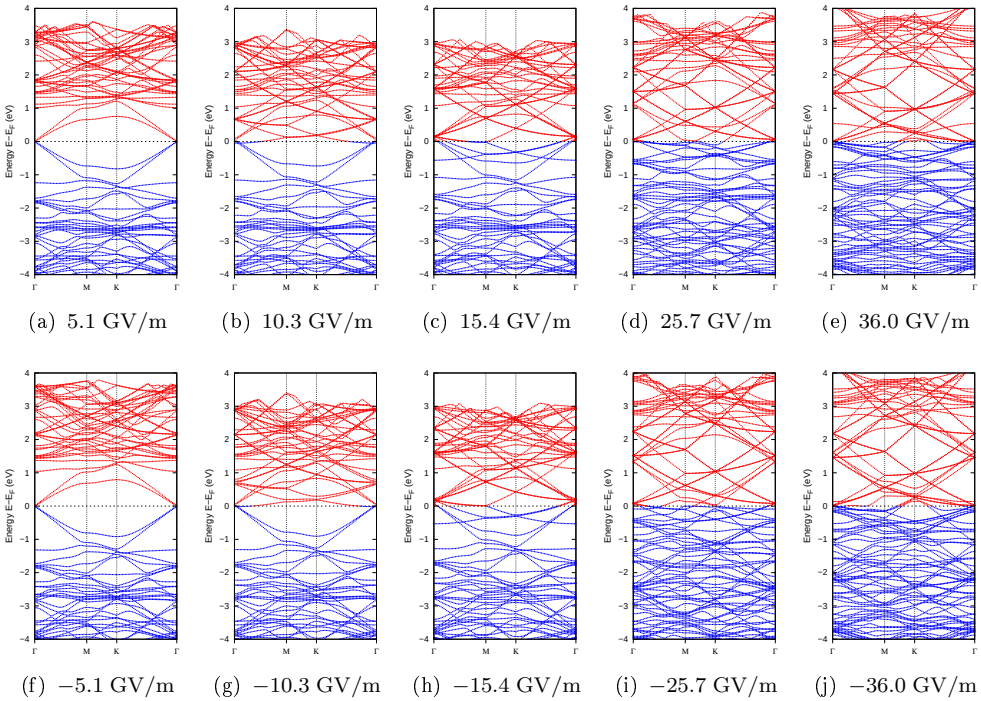

(a) 5.1 GV/m (b) 10.3 GV/m (c) 15.4 GV/m (d) 25.7 GV/m (e) 36.0 GV/m

(f) −5.1 GV/m (g) −10.3 GV/m (h) −15.4 GV/m (i) −25.7 GV/m (j) −36.0 GV/m

Figure 3.37: Band structures at different electric field values.

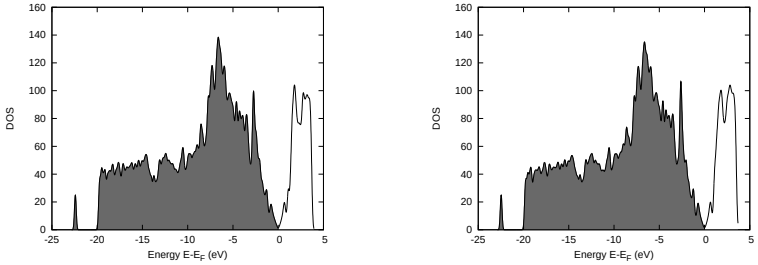

(a) −5.1 GV/m

(b) 5.1 GV/m

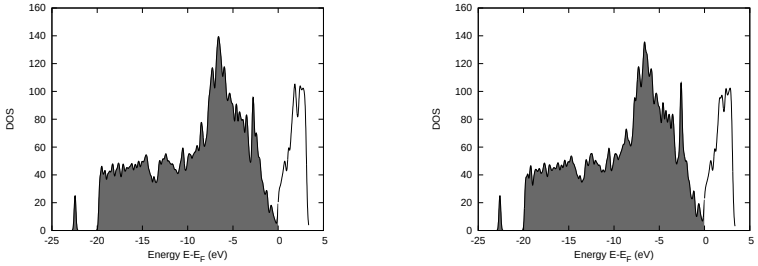

(c) −10.3 GV/m

(d) 10.3 GV/m

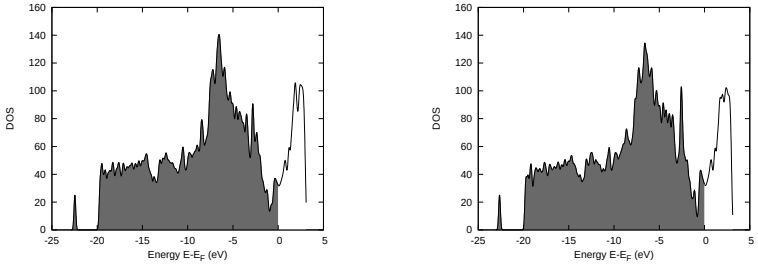

(e) −15.4 GV/m

(f) 15.4 GV/m

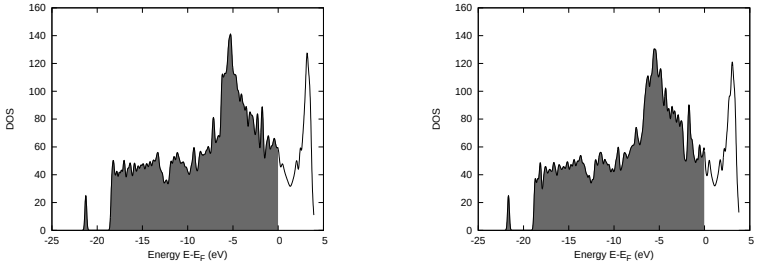

(g) −25.7 GV/m

(h) 25.7 GV/m

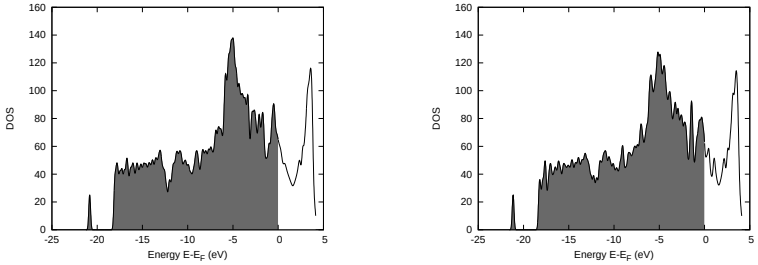

(i) −36.0 GV/m

(j) 36.0 GV/m

Figure 3.38: DOS at different electric field values.

The band structures are shown in Fig. 3.37, while the DOS in Fig. 3.38. The band structure is altered both by the electric field and the curvature, and this implies that the electronic structure is pretty complex. Many bands split, as an effect of the curvature, and the p-doping, consequence of the removed charge, appears at high electric field values. Observing the DOS, many peaks are present due to the doping elements. At the higher fields, the DOS barely barely resembles the one of free standing pure graphene at null field.

3.2.5 N-Graphene

The same simulations performed for BN-graphene, namely relaxations with and without electric field for the $4\sqrt{3} \times 4\sqrt{3}R30$ cell at zero compression and rippled at 2% compression, were repeated for N-graphene, where one carbon atom is replaced by a nitrogen atom, as described in Sec. 3.1.1. The charge difference between N-graphene and pure graphene is reported in Fig. 3.39. As expected, the charge screens the atomic nitrogen charge, that is +1 respect to the carbon atom, fluctuating around the N atom.

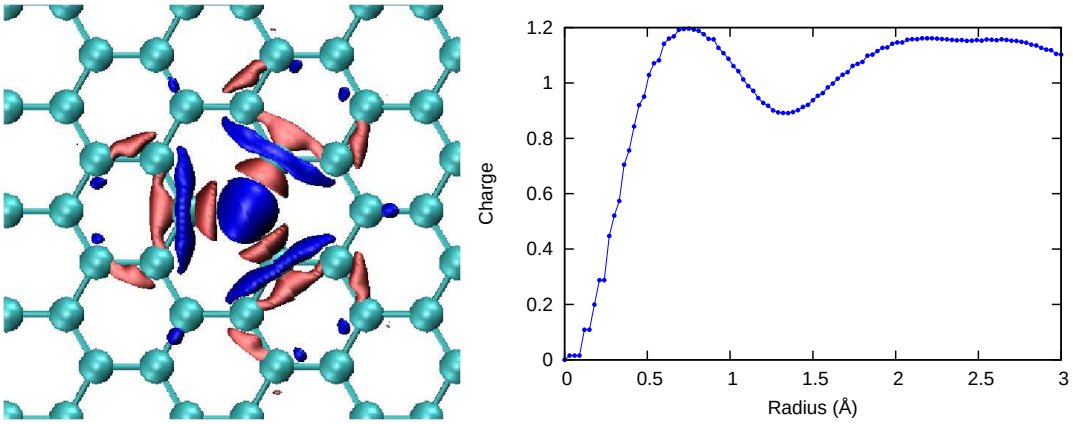

Figure 3.39: (a) Charge difference around the nitrogen atom respect to pure graphene in blue. (b) Graph of the charge difference integrated at different radius.

$4\sqrt{3} \times 4\sqrt{3}R30$ cell at zero compression

Relaxations at different electric field values were performed for the $4\sqrt{3} \times 4\sqrt{3}R30$ cell at zero compression, and the energy E_f, referred to the isoled atoms at null field, and the average curvature k are reported in Tab. 3.10. Differently from BN-graphene, in which the doping atoms enhance the electromechanical response, the N-graphene starts to bend at 6.4 GV/m, about 1.5 GV/m over the value of pure graphene and about 3 GV/m of BN-graphene. This could be due to the stress induced in the structure by the cell boundary conditions. However once the structure is curved, the average curvature at the same field is of the same order of magnitude, even if lower, of BN-graphene and hence much higher than pure graphene.

In Fig. 3.41 the structure at different electric fields are shown. For values up to 10.3 GV/m the curvature is concentrated around the N atom and in particular its three first neighbours, that are higher also than the doping atom. Then, when the electric field is widely above the ionization threshold, the curvature involves all atoms but, differently from pure graphene and BN-graphene, there is not curvature inversion.

F (GV/m)	E_f (eV)	k (Å^{-1})
0.0	−842.97	0
5.1	−843.39	0
6.2	−843.58	0
6.4	−843.63	0.000147
6.7	−843.69	0.000152
6.9	−843.74	0.000159
7.2	−843.83	0.000288
7.5	−843.93	0.000289
7.7	−844.05	0.000288
10.3	−846.05	0.000347
15.4	−853.82	0.000668
25.7	−883.87	0.008401
36.0	−930.89	0.028912

Table 3.10: Energy E_f, referred to the isolated atoms at null field, and average curvature k at different electric field value for the $4\sqrt{3} \times 4\sqrt{3}R30$ N-graphene cell at zero compression.

In Fig. 3.41 the graphs of the energy E_f and the average curvature k at different electric fields are reported. Below the ionization threshold the linear region for the curvature, fingerprint of the flexoelectricity, is easily identifiable. The constant obtained by the fit is $\eta = 2.278 \cdot 10^{-4}$ C/N $\cdot$ m for a corresponding flexoelectric constant, using the pure graphene value of the bending stiffness, about 0.2 nN $\cdot$ nm, of $f = 1.14 \cdot 10^{-21}$ C $= 7.1 \cdot 10^{-3}$ e. This value is slightly less with respect to BN-graphene, but of the same order of magnitude. However the flexoelectricity manifests at much higher electric field values, also with respect to pure graphene.

The charge difference between the cell in electric field and at null field, for values of 5.1 GV/m, below the ionization threshold, and 36.0 GV/m, above the threshold, is reported in Fig. 3.42. The electric field mostly affects the carbon atoms that are neighbours of the nitrogen, moving more charge around these ones. At 36.0 GV/m the charge difference is mainly due to the shift of the atoms caused by the appearing curvature.

Fig. 3.43 reports the band structures at different electric fields, while the DOS are reported in Fig. 3.44. The π bands are splitted due to the nitrogen doping even if the splitting is different from the BN-graphene below the Fermi energy. The p-doping is present over the ionization threshold, as an effect of the charge removed by the electric field. The DOS structure is characterized by the presence of several

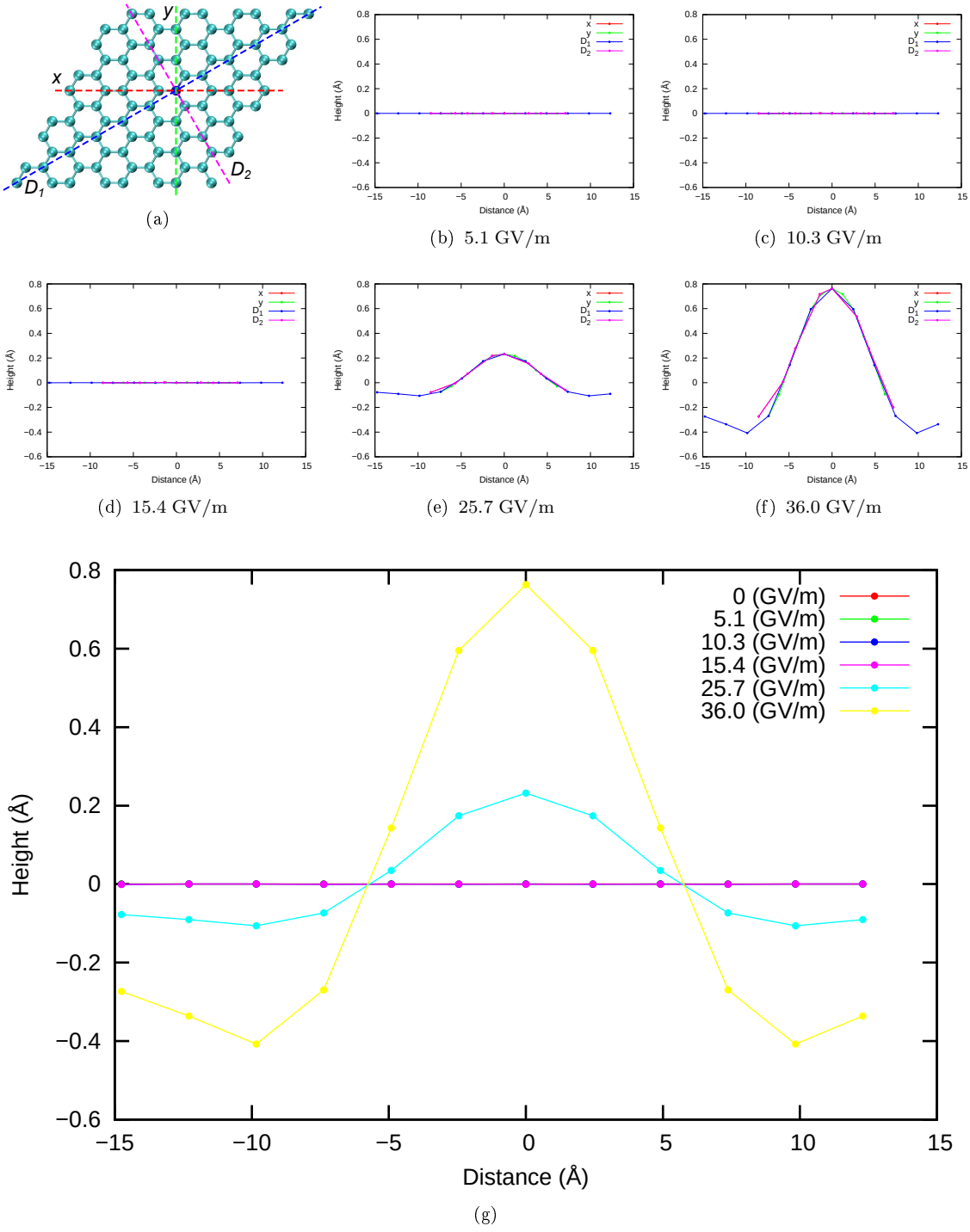

(a) (b) 5.1 GV/m (c) 10.3 GV/m

(d) 15.4 GV/m (e) 25.7 GV/m (f) 36.0 GV/m

(g)

Figure 3.40: Height of the atoms of the $4\sqrt{3} \times 4\sqrt{3}R30$ cell at zero compression. (a) Section lines x, y, D_1 and D_2, passing through the atom on top of the curvature, along which the height of the atoms were plotted. (b) (c) (d) (e) (f) Height of the atoms along the lines x, y, D_1 and D_2. (g) Height of atoms along the D_1 line at different electric field values.

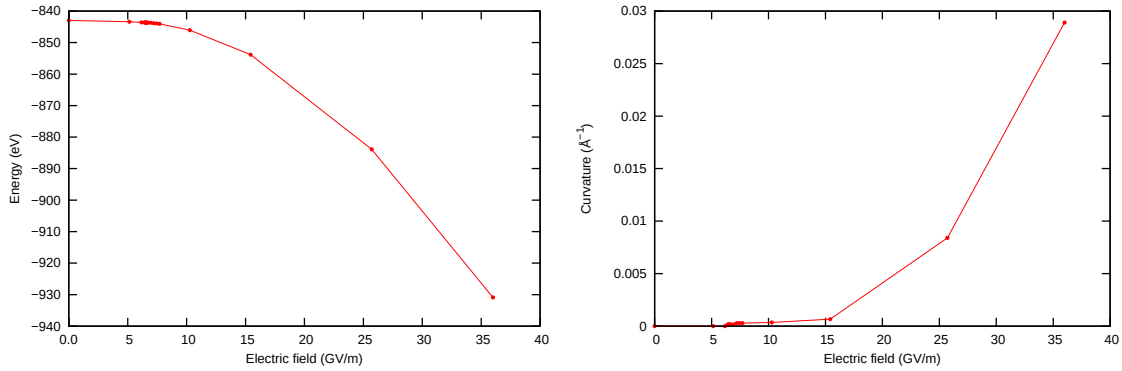

(a)

(b)

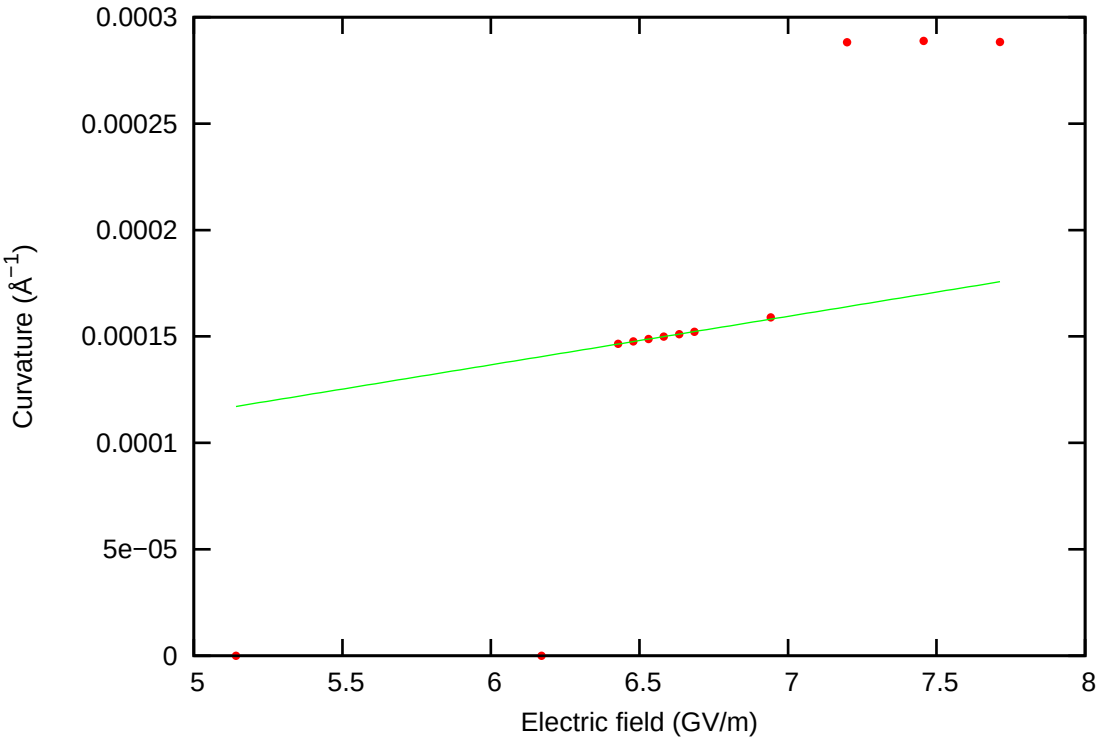

(c)

Figure 3.41: (a) Energy E_f and (b) average curvature k at different electric field values. (c) Zoom of the average curvature near the ionization threshold.

(a) (b)

Figure 3.42: (a) Difference of the total charge density between 5.1 GV/m and null field. (b) Difference of the total charge density between 36.0 GV/m and null field. In blue the areas where the there is more charge with the electric field, in red where there is lesser.

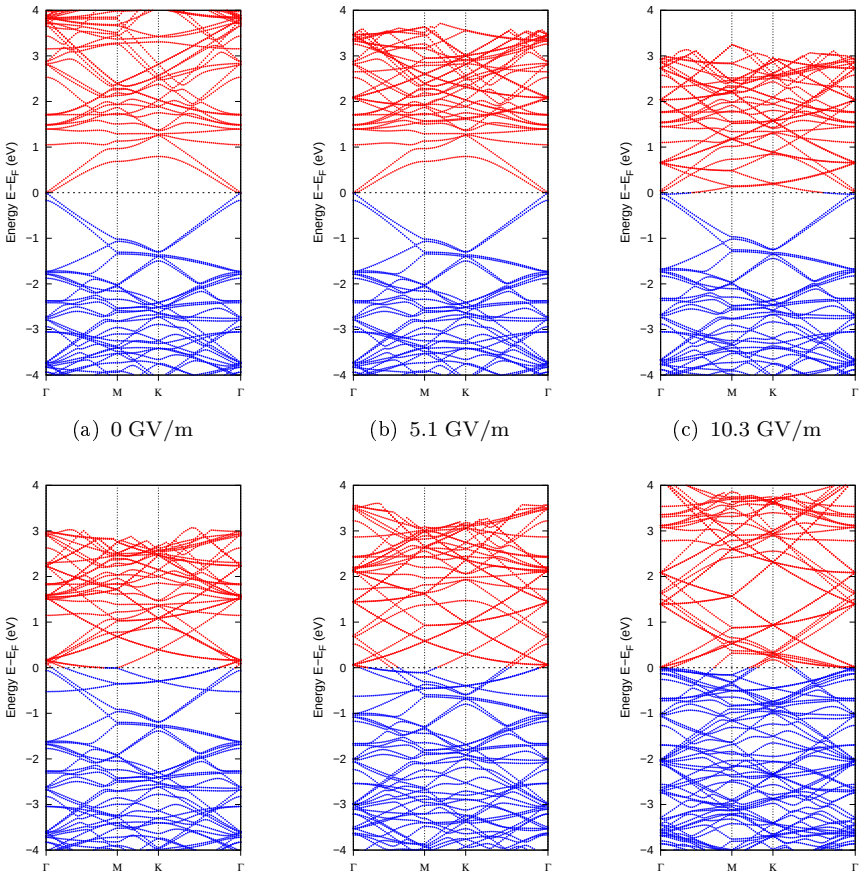

(a) 0 GV/m (b) 5.1 GV/m (c) 10.3 GV/m

(d) 15.4 GV/m (e) 25.7 GV/m (f) 36.0 GV/m

Figure 3.43: Band structures for the N-doped graphene with the $4\sqrt{3} \times 4\sqrt{3}R30$ cell at zero compression at different electric field values.

peaks not correlated to the electric field, even if in a minor way respect to BN-graphene. As for BN-graphene, the low doping keeps the gap closed. The isolated state at -23 eV is still present.

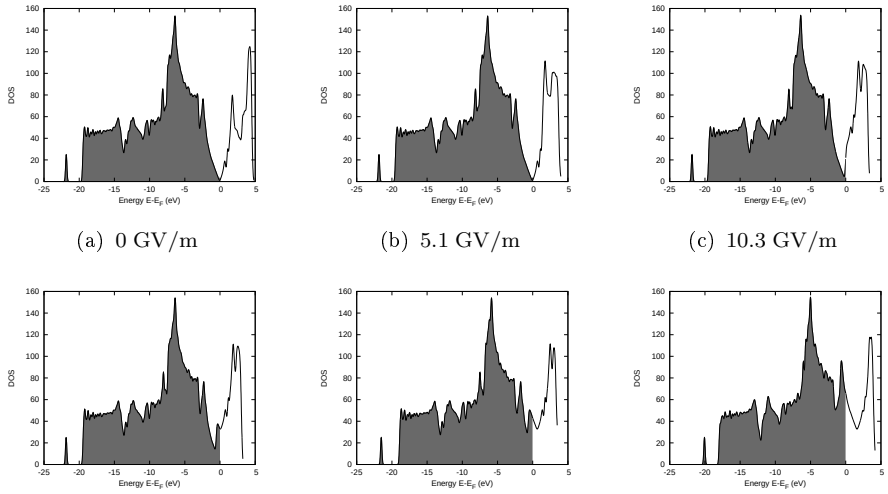

(a) 0 GV/m (b) 5.1 GV/m (c) 10.3 GV/m

(d) 15.4 GV/m (e) 25.7 GV/m (f) 36.0 GV/m

Figure 3.44: DOS for the N-doped graphene with the $4\sqrt{3} \times 4\sqrt{3}R30$ cell at zero compression.

$4\sqrt{3} \times 4\sqrt{3}R30$ rippled cell

Simulations of the rippled N-graphene, using the $4\sqrt{3} \times 4\sqrt{3}R30$ cell compressed at 2%, were performed at different electric fields. The optimized structure for pure graphene at null field was used to perform a relaxation at null field for the N-graphene, in order to obtain the starting structure for ralaxations in electric field. Due to the ripple, the structure is shifted upwards on the z direction of about 0.25 Å respect to the centre of the cell, and the electric field was implemented in both directions.

F (GV/m)	E_f (eV)	k (Å^{-1})
−36.0	−921.97	0.05521
−25.7	−878.09	0.04296
−15.4	−850.35	0.03593
−10.3	−843.14	0.03587
−5.1	−840.68	0.03586
0.0	−840.28	0.03585
5.1	−840.76	0.03585
10.3	−843.90	0.03584
15.4	−852.28	0.03826
25.7	−884.11	0.04621
36.0	−933.96	0.05901

Table 3.11: Energy E_f, referred to the isolated atoms at null field, and average curvature k at different electric field values.

The energy E_f, calculated referring to the isolated atoms at null field, is reported

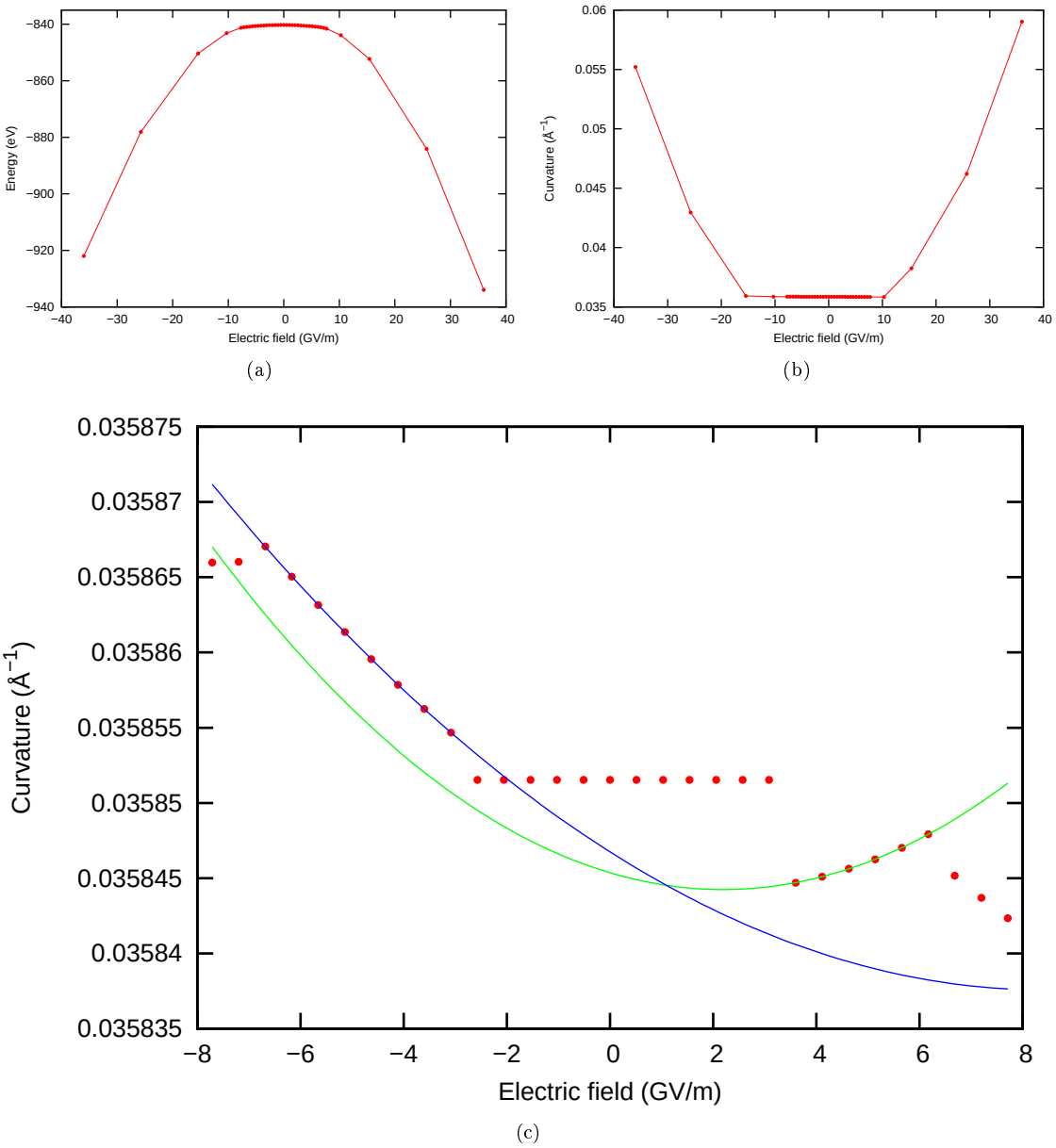

(a) (b)

(c)

Figure 3.45: (a) Energy E_f and (b) average curvature at different electric field values. (c) Curvature for electric field values below the ionization threshold. Data in red, fitting curve in green (positive fields) and blue (negative fields).

with the average curvature in Tab. 3.11 and in Fig. 3.45 at different fields. The structure at various electric fields is shown in Fig. 3.46. The structure does not change significantly for electric fields up to 25 GV/m and, for these field values, does not show a structure asymmetry between positive and negative electric fields. Again, the curvature is stronger around the doping atom but, differently from the BN-graphene, the nitrogen atom involves much more its neighbours on the deformation.

The curvature variation below the ionization threshold is reported in Fig. 3.45(c).

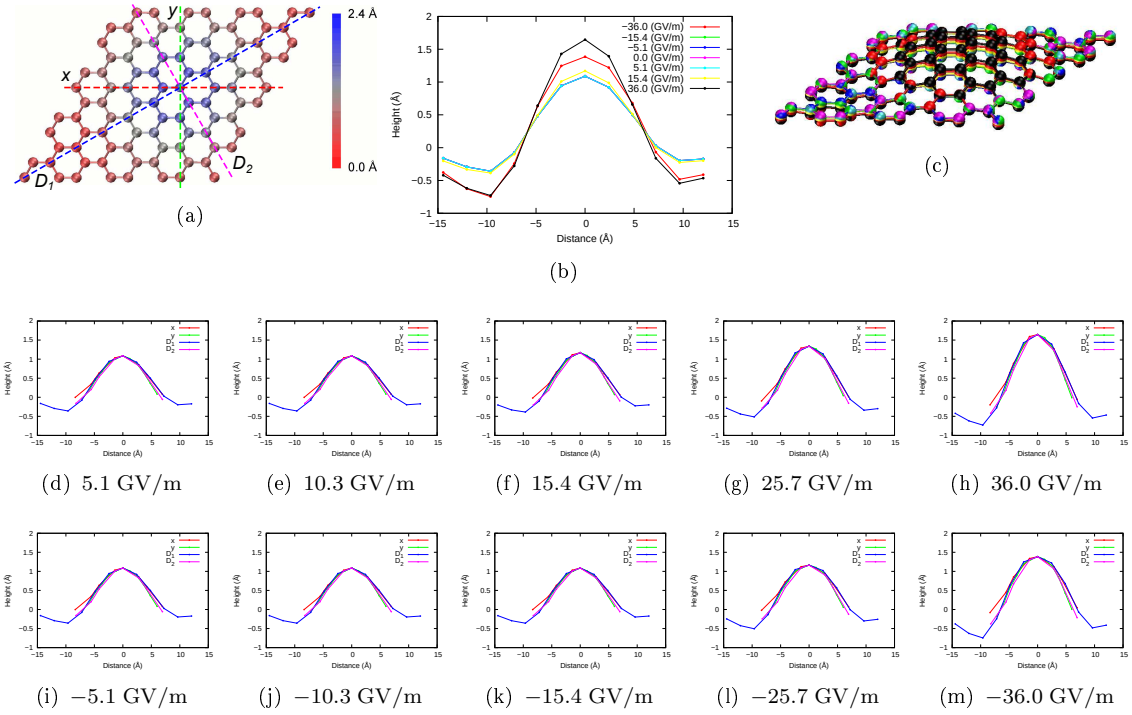

Figure 3.46: (a) Definition of the x, y, D_1 and D_2 lines along which the height of the atoms is shown. (b) Atom heights along the line D_1 for different electric field values. (c) Overlap of different structures at different electric field values. (d) - (m) Atom heights along the line x, y, D_1 and D_2 for different electric field values.

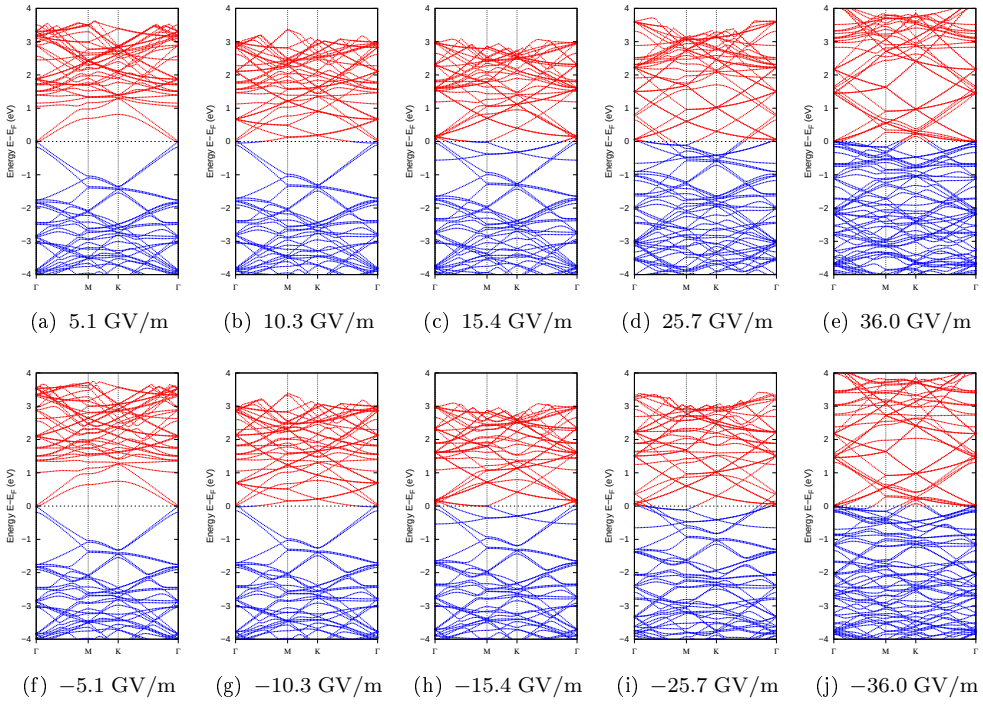

Figure 3.47: Band structures at different electric field values.

The nitrogen doping inverts the effect of the electric field respect to pure graphene: positive fields suppress the curvature while negative fields enhance it. The fit, done separately for positive and negative electric fields with a quadratic function $k(F) = aF^2 + bF + k_0$, gives these values: $a_+ = 2.32 \cdot 10^{-15}$ C^2/N$^2 \cdot$m, $b_+ = -1.02 \cdot 10^{-5}$ C/N$\cdot$m and $k_0^+ = 0.035845$ Å^{-1} for positive fields, $a_- = 1.29 \cdot 10^{-15}$ C^2/N$^2 \cdot$m, $b_- = -2.17 \cdot 10^{-5}$ C/N$\cdot$m and $k_0^- = 0.035847$ Å^{-1} for negative fields.

The electronic structure is reported in Fig. 3.47, the band structure, and in Fig. 3.48, the DOS. The electronic structure is altered by the presence of the nitrogen atom, the electric field and the curvature, that also depends on the field. The p-doping effect is visible, as a consequence of the ionization, and many bands split due to the symmetry breaking caused by the curvature, that is enhanced at higher electric fields. The DOS, altered by the presence of several peaks due the doping, resemble more the one of graphene respect to BN-graphene. For negative electric fields, the DOS are more altered.

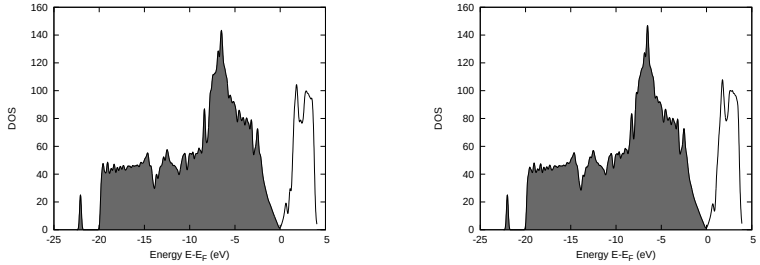

(a) −5.1 GV/m

(b) 5.1 GV/m

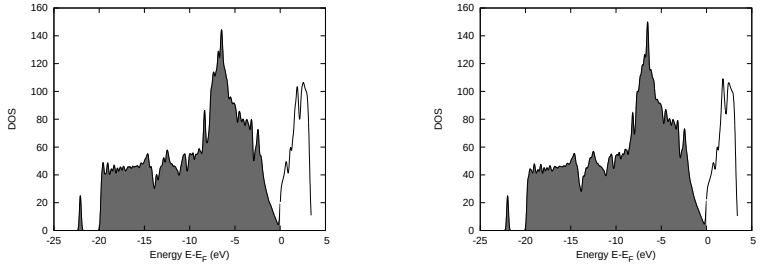

(c) −10.3 GV/m

(d) 10.3 GV/m

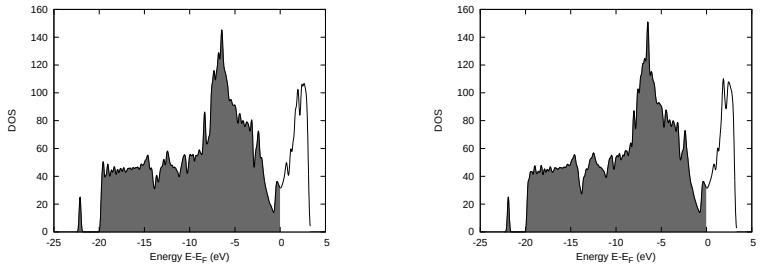

(e) −15.4 GV/m

(f) 15.4 GV/m

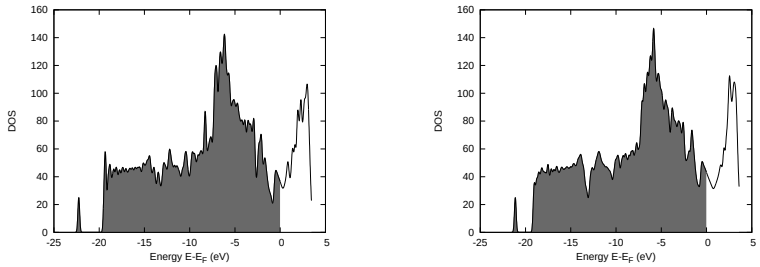

(g) −25.7 GV/m

(h) 25.7 GV/m

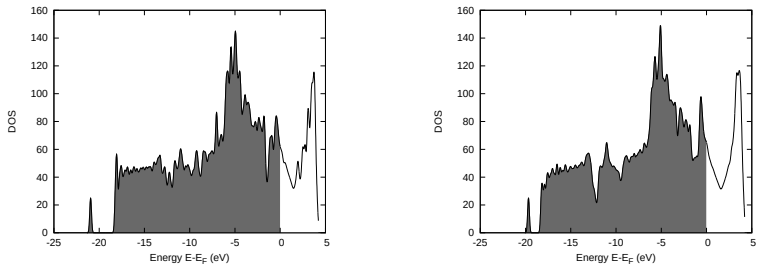

(i) −36.0 V/m

(j) 36.0 GV/m

Figure 3.48: DOS at different electric field values.

Chapter 4

Conclusions

The aim of this work was to study the electromechanical properties and the interaction of graphene with an external orthogonal electric field, in order to, firstly, explore the possibility of manipulation of the structural and electronic properties of this material for technological purpose, and secondly to direct the future possible experiments of graphene on electric field. The electric field intensity was increased in a vast range, in order to observe both small and large structural and chemical alterations, hence reaching and exceed the graphene ionization threshold. The removed charge accumulates in a well defined portion of the simulation supercell, interacting with the ionized graphene. A preliminary study was performed to accurately determine the ionization threshold and the ionic and electronic behaviour over this threshold, in order to choose the appropriate simulation parameters. The polarizability was also evaluated by energy calculations, and a value comparable with other estimates was obtained. An approximated model for the polarizability of the ionized graphene was considered, obtaining that the polarizability decrease as the charge is removed.

Once the effect of the ionization was considered, the flexoelectricity was evaluated. The system used for this study is the $4\sqrt{3} \times 4\sqrt{3}R30$ cell, that approximately reproduce the periodicity of ripples of the graphene grown on silicon carbide, which is one of the most promising techniques to obtain samples for high tech applications. From the simulation performed, the flexoelectric effect is observed as the dependence on curvature is linear, though the estimated flexoelectric constant is different from previous theoretical estimates. Besides differences in calculations setup, this could be attributed to the specific boundary conditions used in these calculations, which influences the symmetry and structure of ripples and, consequently, the curvature properties. This is, however, wanted, since this work calculations are aimed to compare with a specific experimental system, which has the same kind of constraints. Under the ionization threshold, the electronic structure is only qualitatively changed by the effects of curvature and electric field, but the main conductive properties are preserved. Over the threshold the band structure is strongly altered, due to a p-doping effect caused by the removed charge. The same simulations were performed on the rippled structure to mimic the monolayer graphene on SiC and all electromechanical related properties (curvature and flexoelectricity) are seen to be

enhanced. The flexoelectric effect manifests at lower electric fields value respect to flat structures. Different behaviours were found for positive and negative electric fields, but each effect seems to be enhanced and driven by the previously present ripples. These prediction could be experimentally verified on the naturally rippled monolayer graphene on SiC.

The flexoelectricity was studied also in doped systems, the BN-graphene and the N-graphene, in the $4\sqrt{3} \times 4\sqrt{3}R30$ cell at zero compression and rippled. For both systems the flexoelectric constant is enhanced by the presence of the doping atoms, in particular for the BN-graphene, since the boron atom in graphene is seen to be strongly interacting with the external electric field. The flexoelectric constant results enhanced of about three orders of magnitude. Moreover the structure starts to bend at lower field value, even with a lower coupling with the electric field: a double flexoelectric regime was found, the first from the starting of the curvature up to the start of curvature for pure graphene, were a second and greater interaction with the electric field is established. The double regime was found also in the corrugated structures, both at positive and negative fields. As for pure graphene, the flexoelectricity seems to be a second order effect. For the N-graphene, instead, the picture is more complex. The flexoelectric constant was found to be of the same order of magnitude of BN-graphene, but the bending starts at a larger value of the electric field also respect to pure graphene. This unexpected behaviour could be related to the stress induced by the cell boundary constrains, but further analysis are necessary to better understand this phenomenon.

Since one of the goals of the present study was to simulate the real system, SiC structure, first with the buffer layer then adding also the graphene monolayer, was relaxed, with the aim of applying the electric fields, afterwards. Already this calculation, however, lead to some unexpected results. In fact, while the buffer layer structure is similar to the one found by other simulations, this is not true for the monolayer: the ripples of the structure here obtained seem to be inverted with respect to those reported in the literature. Since the two states with "normal" and inverted curvature are perfectly degenerate in absence of substrate, one can infer that they maintain a similar energy even in the presence of substrate. Thus the state here found could be only slightly metastable with respect to the one usually considered the stable one. Further investigations are currently in the course to verify this hypothesis, which is very interesting from the practical point of view. In fact, the calculations on the free standing graphene show that one of the effect of the electric field is precisely the possibility of inverting the curvature, thus it is presumable that the passage from the structural state here found and the one reported in the literature could be driven by the electric field. This in turn could lead to technological applications. The control of local curvature of graphene would lead to the possibility of controlling its interaction with hydrogen or its reactivity towards a number of possible different chemical species, implying the control of functionalization. On the other way round, the inversion of curvature leads to change in electronic structure and could then generate potential differences in graphene, which could be exploited for electromechanical harvesting.

In conclusion, this work shows the possibility of manipulating the electrome-

chanical properties of graphene by curvature and BN doping. Flexoelectricity is shown to be enhanced by already present ripples and by substitutional doping. This might have important consequences in the design of possible devices exploiting flexoelectricity for curvature control and energy applications. In addition, observables are quantitatively evaluated (STM simulated images, DOS, flexoelectric properties, structures) in systems mimicking the real one, which could be directly measured. Thus it is hopeful that this study could stimulate the corresponding experiments, needed to validate these theoretical predictions.

Appendix A

Simulations with QE and supporting softwares

A.1 Quantum ESPRESSO input file

Quantum ESPRESSO is a suite of softwares that performs different kind of calculations. The software that performs the DFT plane wave simulations is pw.x, whose input parameters are passed by a text file. The input file is composed by different sections, each one that describes a different aspect of the simulation. Below is reported the input file for a structural optimization of BN-graphene, in order to understand the layout of the input file.

```
&control
   calculation    = 'relax'              Type of calculation: 'relax' for structural optimization, 'scf' for electronic optimization
   restart_mode   = 'from_scratch'
   prefix         = 'carbon'
   tstress        = .true.
   tprnfor        = .true.
   nstep          = 1000                 Max number of ionic steps for the structural optimization
   max_seconds    = 7080
   pseudo_dir     = 'PSEUDO/'
   outdir         = './outdir_r'
   wf_collect     = .true.
   tefield        = .true.               It sets the electric field
/
&system
   ibrav          = 4                    Bravais lattice type
   celldm(1)      = 32.20                Dimension a of the cell in Bohr
   celldm(3)      = 1.17374285           Ratio between the height c and a
   nat            = 96                   Number of atoms in the cell
   ntyp           = 3                    Number of atom types in the cell
   ecutwfc        = 30.0                 Cutoff energy for the plane waves in Ry
   ecutrho        = 300.0                Cutoff energy for the electronic density in Ry
   occupations    = 'smearing'           It sets the smearing
   smearing       = 'gaussian'           It sets the gaussian smearing
   degauss        = 0.01                 Value of the gaussian smearing in Ry
```

```
   london          = .true.
   edir            = 3
   emaxpos         = 0.875
   eopreg          = 0.25
   eamp            = 0.01
/
&electrons
   diagonalization= 'david'
   mixing_mode     = 'plain'
   mixing_beta     = 0.7
   conv_thr        = 1.0d-8
/
&Ions
/
ATOMIC_SPECIES
   B  10.8  B.pbe-n-rrkjus_psl.0.1.UPF
   C  12.0  C.pbe-n-rrkjus_psl.0.1.UPF
   N  14.0  N.pbe-n-rrkjus_psl.0.1.UPF
ATOMIC_POSITIONS {angstrom}
   N   0.001236263   0.003110308  10.0
   C   2.135602007   3.685581470  10.0
   ...
   C  23.444781028  13.532223626  10.0
K_POINTS gamma
```

It sets the semi-empirical van der Waals implementation

Direction of the electric field

Relative position of the maximum of the electrostatic potential

Relative lenght of the electric potential drop zone

Amplitude of the electric field in au

Diagonalization algorithm

Convergence criterion for the DFT self-consisten cycle

Types of atoms, their masses and their pseudopotential files

For band structure calculations, the flag `'relax'`, in `calculation`, is replaced by `'bands'`, while the k-points sampling is defined replacing the last line with a code of this type:

```
K_POINTS crystal
  100
0.0000000000    0.0000000000    0.0000000000    1.0
0.0000000000   -0.0138888889    0.0000000000    1.0
...
0.0079364286   -0.0158730952    0.0000000000    1.0
0.0000000000    0.0000000000    0.0000000000    1.0
```

The flag `crystal` indicates that the coordinates of each of the 100 k-points is expressed as relative to the base vectors of the Brillouin zone. For each point, the three coordinates plus the weight of the point are reported. This code is obtained using XCrySDen, a crystalline structure visualisation program that can read QE input and output files and reproduce the structures. Moreover the corresponding Brillouin zone is reproduced, and one can graphically select the path along the high symmetry k-points to obtain this code.

For DOS calculations, instead, the flag `'relax'` is replaced by `'nscf'`, while the k-point grid is expressed as:

```
K_POINTS automatic
  15 15 1 0 0 0
```

The first three number generate the $15 \times 15 \times 1$ grid, while the other three express the offset of the grid, that it is null in this case.

For both band strucure and DOS calculations further computations are required to obtain the data, performed by others softwares of the QE suite: bands.x for the band structure and dos.x for the DOS. Finally the charge density is obtained with the program pp.x.

A.2 Self made programs

Several self made programs were written, mainly in C, for the input structures building and the data analysis. A partial list of written programs includes:

- building of the graphene layer, namely the coordinates of each carbon atom in the hexagonal lattice;
- calculation of the difference of two charge densities;
- integration of the charge density along xy planes (to evaluate the removed charge) and around a specific atom;
- evaluation of the local curvature, both the improper dihedral angle and the local sphere radius.

The program for the evaluation of the local curvature is the more complex, due to the difficulty of the identification of the first neighbours for the atoms at the cell edges. Using the building structure file, the identification of the neighbours was implemented as follows:

```
#define DIST 1.7

typedef struct vettore{
  char type[2];
  double pos[3];
  int index;
  int sym;
  struct vettore *next[3];
}node;

void vicini(node **c,int dim,double CELLDM){
  double b[2][3],v[2][3],dx,dy,dz,dist,max,coord[dim][3],CELLDM_P;
  node *aux;
  int i,j,k,l,cont,indx;
  char car,path[100],*stringa;
  FILE *file;

  CELLDM_P=32.20*ANG;
  file=fopen("coord.xyz","r");
  fscanf(file,"%d\n",&i);
  stringa=fgets(path,100,file);

  i=0;
  while(!feof(file)){
    fscanf(file,"%s\t",path);
    fscanf(file,"%lf\t",&coord[i][0]);
    fscanf(file,"%lf\t",&coord[i][1]);
    fscanf(file,"%lf\n",&coord[i][2]);
    i++;
  }
  fclose(file);

  b[0][0]=CELLDM;
  b[0][1]=0;
  b[0][2]=0;
  b[1][0]=0.5*CELLDM;
  b[1][1]=0.5*sqrt(3)*CELLDM;
```

```
  b[1][2]=0;
  v[0][0]=CELLDM_P;
  v[0][1]=0;
  v[0][2]=0;
  v[1][0]=0.5*CELLDM_P;
  v[1][1]=0.5*sqrt(3)*CELLDM_P;
  v[1][2]=0;

  for(i=0;i<dim;i++){
    cont=0;
    for(j=0;j<dim;j++)
      if(j!=i)
for(k=-1;k<=1;k++)
     for(l=-1;l<=1;l++){
     dx=coord[j][0]+k*v[0][0]+l*v[1][0]-coord[i][0];
    dy=coord[j][1]+k*v[0][1]+l*v[1][1]-coord[i][1];
    dz=coord[j][2]+k*v[0][2]+l*v[1][2]-coord[i][2];
    dist=sqrt(pow(dx,2)+pow(dy,2)+pow(dz,2));
     if(dist<DIST){
         aux=new_node();
         aux->pos[0]=c[j]->pos[0]+k*b[0][0]+l*b[1][0];
          aux->pos[1]=c[j]->pos[1]+k*b[0][1]+l*b[1][1];
         aux->pos[2]=c[j]->pos[2]+k*b[0][2]+l*b[1][2];
         aux->index=j;
         c[i]->next[cont]=aux;
         cont++;
    }
     }
     for(j=0;j<3;j++){
       max=c[i]->next[j]->pos[1];
       indx=j;
       for(k=j;k<3;k++)
     if(c[i]->next[k]->pos[1]>max){
       max=c[i]->next[k]->pos[1];
       indx=k;
     }
       if(indx!=j){
     aux=c[i]->next[j];
     c[i]->next[j]=c[i]->next[indx];
     c[i]->next[indx]=aux;
       }
     }
     c[i]->sym=0;
     if(c[i]->pos[0]>c[i]->next[1]->pos[0]){
       aux=c[i]->next[1];
       c[i]->next[1]=c[i]->next[2];
       c[i]->next[2]=aux;
       c[i]->sym=1;
     }
  }
  return;
}
```

Appendix B

Details of the calculation protocols

B.1 Cutoff energies

The convergence study for the cutoff energy for the plane waves was performed on the graphene unit cell at null field, with a irreducible Brillouin zone sampling of $15 \times 15 \times 1$. The cohesive energy of the system, calculated at different cutoff energies, is reported in Tab. B.1(a) and plotted in the graph of Fig. B.1. The cohesive energy starts to converge at ~ 25 Ry, hence the cutoff energy was setted to 30 Ry. For what concern the cutoff energy for the electronic density, it was setted to 300 Ry, according to the instructions of the QE documentation[45], that recommends, for ultrasoft pseudopotentials, a value from 8 to 12 times the plane wave cutoff.

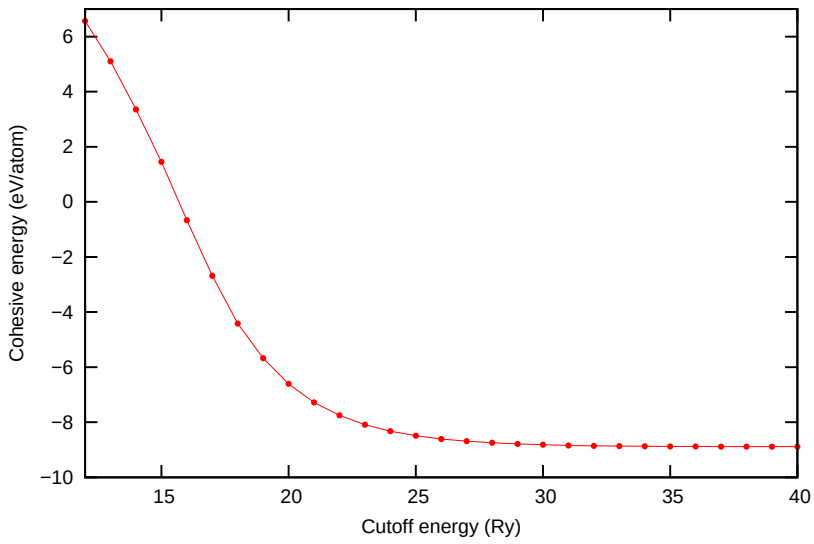

Figure B.1: Graph of the convergence test for the plane wave energy cutoff for the PBE functional, obtained by unit cell simulation with a $15 \times 15 \times 1$ k-point grid sampling. A value of 30 Ry was chosen.

B.2 Grids for the Brillouin zone integration

Similar tests were made to determine the grid sampling to use for the integration of the irreducible Brillouin zone. Since the Brillouin zone depends on the size of the real cell, a study for each cell was made. In Tab. B.1 (b) (c) and in Fig. B.2 are reported the cohesive energies of the graphene in the unit cell and in the $4\sqrt{3} \times 4\sqrt{3}R30$ cell with different grid sampling in the reciprocal space (note that along the z direction only one point is sampled). For the unit cell, the system starts to converge with a grid of 8×8, but since the computational times do not vary significantly increasing the sampling, at least for this cell, a denser grid was chosen, equal to 15×15.

For the $4\sqrt{3} \times 4\sqrt{3}R30$ cell, instead, the energy difference between the value with the Γ point sampling and the convergence value is $\sim 0.25\%$, hence only the Γ point was sampled in simulations with this cell. Finally for the 13×13 cell, being bigger than the $4\sqrt{3} \times 4\sqrt{3}R30$ and hence having a smaller Brillouin zone, a convergence study was not made and the Γ point sampling was used.

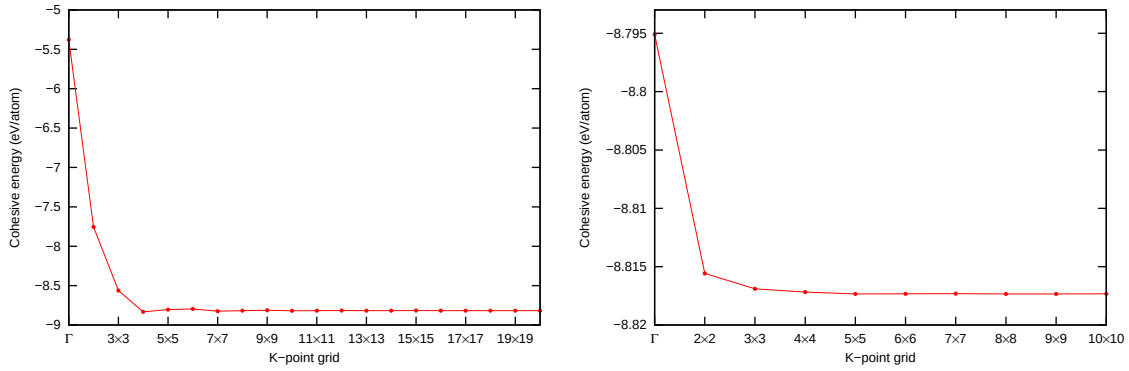

(a) Unit cell

(b) $4\sqrt{3} \times 4\sqrt{3}R30$ cell

Figure B.2: Graphs of the convergence tests varying the k-point grid sampling. A 15×15 grid was chosen for the unit cell, while for the $4\sqrt{3} \times 4\sqrt{3}R30$ and the 13×13 cells, the grid is reduced to the only Γ point.

B.3 Input structure for the rippled cell

To obtain the rippled $4\sqrt{3} \times 4\sqrt{3}R30$ cell, the cell parameter was compressed by 2% and a ripple was superimposed to the structure, then a relaxation at null electric field was performed. The initial ripple consists of a Gauss bell with an height amplitude of 0.5 Å, as shown in Fig. B.3.

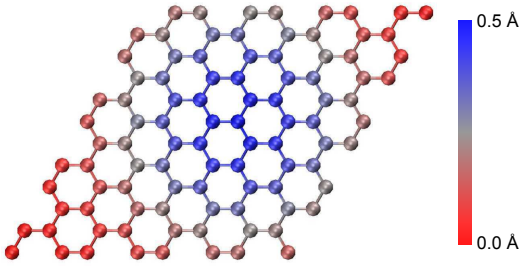

Figure B.3: Input strucure for the relaxation of the rippled $4\sqrt{3} \times 4\sqrt{3}R30$ cell with null electric field. In blue the higher height, in red the lower.

E_{cut} (Ry)	E_{coh} (eV/atom)
12	6.5655
13	5.1058
14	3.3524
15	1.4499
16	−0.6632
17	−2.6814
18	−4.4144
19	−5.6721
20	−6.6077
21	−7.2777
22	−7.7501
23	−8.0901
24	−8.3250
25	−8.4880
26	−8.6061
27	−8.6868
28	−8.7446
29	−8.7870
30	−8.8169
31	−8.8393
32	−8.8549
33	−8.8661
34	−8.8733
35	−8.8781
36	−8.8811
37	−8.8830
38	−8.8840
39	−8.8847
40	−8.8850

(a) Unit cell

k-grid	E_{coh} (eV/atom)
Γ	−5.3783
2×2	−7.7546
3×3	−8.5618
4×4	−8.8324
5×5	−8.8051
6×6	−8.7966
7×7	−8.8242
8×8	−8.8171
9×9	−8.8130
10×10	−8.8200
11×11	−8.8179
12×12	−8.8156
13×13	−8.8184
14×14	−8.8177
15×15	−8.8169
16×16	−8.8179
17×17	−8.8178
18×18	−8.8173
19×19	−8.8177
20×20	−8.8177

(b) Unit cell

k-grid	E_{coh} (eV/atom)
Γ	−8.7951
2×2	−8.8156
3×3	−8.8169
4×4	−8.8172
5×5	−8.8173
6×6	−8.8173
7×7	−8.8173
8×8	−8.8173
9×9	−8.8173
10×10	−8.8173

(c) $4\sqrt{3} \times 4\sqrt{3}R30$ cell

Table B.1: (a) Cohesive energy per atom at different plane wave cutoff energies. (b) (c) Cohesive energy per atom at different integration grid in reciprocal space.

Appendix C

Lattice constant optimization for the $4\sqrt{3} \times 4\sqrt{3}R30$ cell

The graphene $4\sqrt{3} \times 4\sqrt{3}R30$ flat cell was relaxed at different lattice constants a to find the one for which the cohesive energy reaches its minimum. All the data are reported in Tab. C.1 and in Fig. C.1. A value of 16.9914 Å for the lattice constant, corresponding to an effective C-C bond lenght of 1.41595 Å, was found.

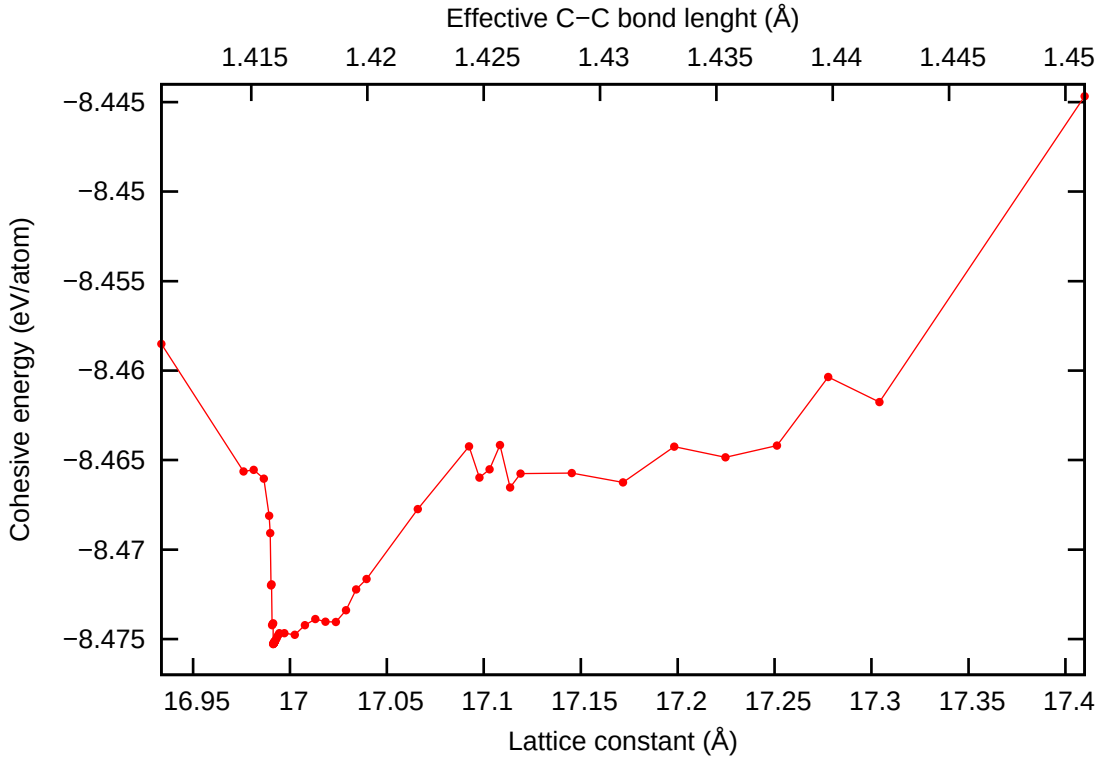

Figure C.1: Graph of the cohesive energy per atom at different lattice constant for the $4\sqrt{3} \times 4\sqrt{3}R30$ cell with flat structure.

a (Å)	C-C (Å)	E_{coh} (eV/atom)
16.9337	1.411139	−8.4585
16.9760	1.414667	−8.4656
16.9813	1.415108	−8.4655
16.9866	1.415549	−8.4660
16.9892	1.415770	−8.4681
16.9898	1.415814	−8.4691
16.9903	1.415858	−8.4720
16.9906	1.415880	−8.4720
16.9908	1.415902	−8.4742
16.9911	1.415924	−8.4742
16.9914	1.415946	−8.4741
16.9914	1.415950	−8.4753
16.9915	1.415955	−8.4753
16.9915	1.415959	−8.4753
16.9916	1.415964	−8.4752
16.9916	1.415968	−8.4752
16.9917	1.415972	−8.4752
16.9917	1.415977	−8.4752
16.9918	1.415981	−8.4752
16.9918	1.415986	−8.4752
16.9919	1.415990	−8.4752
16.9919	1.415990	−8.4752
16.9919	1.415995	−8.4752
16.9920	1.415999	−8.4752
16.9920	1.416003	−8.4752
16.9921	1.416008	−8.4751
16.9921	1.416012	−8.4751
16.9924	1.416034	−8.4751

a (Å)	C-C (Å)	E_{coh} (eV/atom)
16.9929	1.416078	−8.4750
16.9935	1.416122	−8.4749
16.9940	1.416167	−8.4748
16.9945	1.416211	−8.4747
16.9972	1.416431	−8.4747
17.0025	1.416872	−8.4748
17.0078	1.417313	−8.4742
17.0130	1.417754	−8.4739
17.0183	1.418195	−8.4740
17.0236	1.418636	−8.4740
17.0289	1.419077	−8.4734
17.0342	1.419518	−8.4722
17.0395	1.419959	−8.4716
17.0660	1.422164	−8.4677
17.0924	1.424369	−8.4642
17.0977	1.424810	−8.4660
17.1030	1.425251	−8.4655
17.1083	1.425692	−8.4642
17.1136	1.426133	−8.4665
17.1189	1.426574	−8.4658
17.1453	1.428779	−8.4657
17.1718	1.430983	−8.4662
17.1983	1.433188	−8.4643
17.2247	1.435393	−8.4648
17.2512	1.437598	−8.4642
17.2776	1.439803	−8.4604
17.3041	1.442008	−8.4618
17.4099	1.450828	−8.4447

Table C.1: Cohesive energy for atom at different lattice constant a and corresponding effective C-C bond lenght for the $4\sqrt{3} \times 4\sqrt{3}R30$ flat cell.

Bibliography

[1] A. K. Geim and K. S. Novoselov, "The rise of graphene," *Nat Mater*, vol. 6, pp. 183–191, Mar. 2007.

[2] P. R. Wallace, "The Band Theory of Graphite," *Phys. Rev.*, vol. 71, pp. 622–634, May 1947.

[3] J. C. Slonczewski and P. R. Weiss, "Band Structure of Graphite," *Phys. Rev.*, vol. 109, pp. 272–279, Jan 1958.

[4] R. E. Peierls, "Quelques proprietes typiques des corpses solides," *Ann. I. H. Poincare*, vol. 5, pp. 177–222, 1935.

[5] L. D. Landau, "Zur Theorie der phasenumwandlungen II," *Phys. Z. Sowjetunion*, vol. 11, pp. 26–35, 1937.

[6] N. D. Mermin, "Crystalline Order in Two Dimensions," *Phys. Rev.*, vol. 176, pp. 250–254, Dec 1968.

[7] K. S. Novoselov, A. K. Geim, S. V. Morozov, D. Jiang, Y. Zhang, S. V. Dubonos, I. V. Grigorieva, and A. A. Firsov, "Electric Field Effect in Atomically Thin Carbon Films," *Science*, vol. 306, no. 5696, pp. 666–669, 2004.

[8] A. H. Castro Neto, F. Guinea, N. M. R. Peres, K. S. Novoselov, and A. K. Geim, "The electronic properties of graphene," *Rev. Mod. Phys.*, vol. 81, pp. 109–162, Jan 2009.

[9] M. Klintenberg, S. Lebègue, C. Ortiz, B. Sanyal, J. Fransson, and O. Eriksson, "Evolving properties of two-dimensional materials: from graphene to graphite," *Journal of Physics: Condensed Matter*, vol. 21, no. 33, p. 335502, 2009.

[10] B. Partoens and F. M. Peeters, "From graphene to graphite: Electronic structure around the K point," *Phys. Rev. B*, vol. 74, p. 075404, Aug 2006.

[11] Y. Zhang, Y.-W. Tan, H. L. Stormer, and P. Kim, "Experimental Observation of Quantum Hall Effect and Berry's Phase in Graphene," Sept. 2005.

[12] K. S. Novoselov, Z. Jiang, Y. Zhang, S. V. Morozov, H. L. Stormer, U. Zeitler, J. C. Maan, G. S. Boebinger, P. Kim, and A. K. Geim, "Room-Temperature Quantum Hall Effect in Graphene," *Science*, vol. 315, p. 1379, Mar. 2007.

[13] K. V. Emtsev, A. Bostwick, K. Horn, J. Jobst, G. L. Kellogg, L. Ley, J. L. McChesney, T. Ohta, S. A. Reshanov, J. Rohrl, E. Rotenberg, A. K. Schmid, D. Waldmann, H. B. Weber, and T. Seyller, "Towards wafer-size graphene layers by atmospheric pressure graphitization of silicon carbide," *Nature Materials*, vol. 8, pp. 203–207, Feb. 2009.

[14] A. Mattausch and O. Pankratov, "*Ab Initio* Study of Graphene on SiC," *Phys. Rev. Lett.*, vol. 99, p. 076802, Aug 2007.

[15] F. Varchon, P. Mallet, J.-Y. Veuillen, and L. Magaud, "Ripples in epitaxial graphene on the Si-terminated SiC(0001) surface," *Phys. Rev. B*, vol. 77, p. 235412, Jun 2008.

[16] S. Kim, J. Ihm, H. J. Choi, and Y.-W. Son, "Origin of Anomalous Electronic Structures of Epitaxial Graphene on Silicon Carbide," *Phys. Rev. Lett.*, vol. 100, p. 176802, Apr 2008.

[17] P. V. Yudin and A. K. Tagantsev, "Fundamentals of flexoelectricity in solids," *Nanotechnology*, vol. 24, no. 43, p. 432001, 2013.

[18] J. Hong and D. Vanderbilt, "First-principles theory and calculation of flexoelectricity," *Phys. Rev. B*, vol. 88, p. 174107, Nov 2013.

[19] R. Maranganti and P. Sharma, "Atomistic determination of flexoelectric properties of crystalline dielectrics," *Phys. Rev. B*, vol. 80, p. 054109, Aug 2009.

[20] A. K. Tagantsev, "Piezoelectricity and flexoelectricity in crystalline dielectrics," *Phys. Rev. B*, vol. 34, pp. 5883–5889, Oct 1986.

[21] R. Resta, "Towards a Bulk Theory of Flexoelectricity," *Physical Review Letters*, vol. 105, p. 127601, sep 2010.

[22] M. T. Ong and E. J. Reed, "Engineered Piezoelectricity in Graphene," *ACS Nano*, vol. 6, pp. 1387–1394, Dec. 2011.

[23] I. Naumov, A. M. Bratkovsky, and V. Ranjan, "Unusual Flexoelectric Effect in Two-Dimensional Noncentrosymmetric sp^2-Bonded Crystals," *Phys. Rev. Lett.*, vol. 102, p. 217601, May 2009.

[24] S. V. Kalinin and V. Meunier, "Electronic flexoelectricity in low-dimensional systems," *Phys. Rev. B*, vol. 77, p. 033403, Jan 2008.

[25] Z. Wang, L. Philippe, and J. Elias, "Deflection of suspended graphene by a transverse electric field," *Phys. Rev. B*, vol. 81, p. 155405, Apr 2010.

[26] V. Tozzini and V. Pellegrini, "Reversible Hydrogen Storage by Controlled Buckling of Graphene Layers," *J. Phys. Chem. C*, vol. 115, pp. 25523–25528, Nov. 2011.

[27] G. Grosso and G. Parravicini, *Solid State Physics*. Elsevier Science, 2000.

[28] E. Gross and R. Dreizler, *Density Functional Theory*. Springer, 1995.

[29] W. Kohn and L. J. Sham, "Self-Consistent Equations Including Exchange and Correlation Effects," *Phys. Rev.*, vol. 140, pp. A1133–A1138, Nov 1965.

[30] J. P. Perdew and A. Zunger, "Self-interaction correction to density-functional approximations for many-electron systems," *Phys. Rev. B*, vol. 23, pp. 5048–5079, May 1981.

[31] J. C. Slater, "A Simplification of the Hartree-Fock Method," *Phys. Rev.*, vol. 81, pp. 385–390, Feb 1951.

[32] J. P. Perdew, K. Burke, and M. Ernzerhof, "Generalized Gradient Approximation Made Simple," *Phys. Rev. Lett.*, vol. 77, pp. 3865–3868, Oct 1996.

[33] Calandra, Matteo and Mauri, Francesco, "Electron-phonon coupling and electron self-energy in electron-doped graphene: Calculation of angular-resolved photoemission spectra," *Phys. Rev. B*, vol. 76, p. 205411, Nov 2007.

[34] Becke, Axel D., "Density-functional thermochemistry. III. The role of exact exchange," *The Journal of Chemical Physics*, vol. 98, no. 7, pp. 5648–5652, 1993.

[35] Lee, Chengteh and Yang, Weitao and Parr, Robert G., "Development of the Colle-Salvetti correlation-energy formula into a functional of the electron density," *Phys. Rev. B*, vol. 37, pp. 785–789, Jan 1988.

[36] Adamo, Carlo and Barone, Vincenzo, "Toward reliable density functional methods without adjustable parameters: The PBE0 model," *The Journal of Chemical Physics*, vol. 110, no. 13, pp. 6158–6170, 1999.

[37] F. Aryasetiawan and O. Gunnarson, "The GW method," *Rep. Prog. Phys.*, vol. 61, pp. 237–312, 1998.

[38] E. Runge and E. K. U. Gross, "Density-Functional Theory for Time-Dependent Systems," *Phys. Rev. Lett.*, vol. 52, pp. 997–1000, Mar 1984.

[39] A. D. McNaught and A. Wilkinson, *Compendium of Chemical Terminology*. IUPAC Nomenclature Books Series ("Color Books"), Oxford: Blackwell Science, 2nd edition ed., 1997.

[40] X. Wu, M. C. Vargas, S. Nayak, V. Lotrich, and G. Scoles, "Towards extending the applicability of density functional theory to weakly bound systems," *The Journal of Chemical Physics*, vol. 115, no. 19, pp. 8748–8757, 2001.

[41] S. Grimme, "Semiempirical GGA-type density functional constructed with a long-range dispersion correction," *Journal of Computational Chemistry*, vol. 27, no. 15, pp. 1787–1799, 2006.

[42] H. Hellmann, "A New Approximation Method in the Problem of Many Electrons," *The Journal of Chemical Physics*, vol. 3, no. 1, pp. 61–61, 1935.

[43] D. R. Hamann, M. Schlüter, and C. Chiang, "Norm-Conserving Pseudopotentials," *Phys. Rev. Lett.*, vol. 43, pp. 1494–1497, Nov 1979.

[44] D. Vanderbilt, "Soft self-consistent pseudopotentials in a generalized eigenvalue formalism," *Phys. Rev. B*, vol. 41, pp. 7892–7895, Apr 1990.

[45] `http://www.quantum-espresso.org/wp-content/uploads/Doc/INPUT_PW.html`.

[46] J. Moreno and J. M. Soler, "Optimal meshes for integrals in real- and reciprocal-space unit cells," *Phys. Rev. B*, vol. 45, pp. 13891–13898, Jun 1992.

[47] H. J. Monkhorst and J. D. Pack, "Special points for Brillouin-zone integrations," *Phys. Rev. B*, vol. 13, pp. 5188–5192, Jun 1976.

[48] P. Giannozzi, S. Baroni, N. Bonini, M. Calandra, R. Car, C. Cavazzoni, D. Ceresoli, G. L. Chiarotti, M. Cococcioni, I. Dabo, A. D. Corso, S. de Gironcoli, S. Fabris, G. Fratesi, R. Gebauer, U. Gerstmann, C. Gougoussis, A. Kokalj, M. Lazzeri, L. Martin-Samos, N. Marzari, F. Mauri, R. Mazzarello, S. Paolini, A. Pasquarello, L. Paulatto, C. Sbraccia, S. Scandolo, G. Sclauzero, A. P. Seitsonen, A. Smogunov, P. Umari, and R. M. Wentzcovitch, "QUANTUM ESPRESSO: a modular and open-source software project for quantum simulations of materials," *Journal of Physics: Condensed Matter*, vol. 21, no. 39, p. 395502, 2009.

[49] A. Rossi, V. Tozzini, *et al.*, "Structure, electronic properties and stability of nano-scopically of ripples corrugated/hydrogenated graphene: a Density Functional Theory study," Submitted.

[50] http://www.hpc.cineca.it/content/documentation.

[51] T. I. Oh, Y. J. Yoo, Y. S. You, and K. Y. Kim, "Generation of strong terahertz fields exceeding 8 MV/cm at 1 kHz and real-time beam profiling," *Applied Physics Letters*, vol. 105, no. 4, 2014.

[52] J. Hebling, K.-L. Yeh, M. C. Hoffmann, B. Bartal, and K. A. Nelson, "Generation of high-power terahertz pulses by tilted-pulse-front excitation and their application possibilities," *J. Opt. Soc. Am. B*, vol. 25, pp. B6–B19, Jul 2008.

[53] A. Sell, A. Leitenstorfer, and R. Huber, "Phase-locked generation and field-resolved detection of widely tunable terahertz pulses with amplitudes exceeding 100 MV/cm," *Opt. Lett.*, vol. 33, pp. 2767–2769, Dec 2008.

[54] E. K. Yu, D. A. Stewart, and S. Tiwari, "*Ab initio* study of polarizability and induced charge densities in multilayer graphene films," *Phys. Rev. B*, vol. 77, p. 195406, May 2008.

[55] Q. Lu, M. Arroyo, and R. Huang, "Elastic bending modulus of monolayer graphene," *Journal of Physics D: Applied Physics*, vol. 42, no. 10, p. 102002, 2009.

[56] C. Lee, X. Wei, J. W. Kysar, and J. Hone, "Measurement of the Elastic Properties and Intrinsic Strength of Monolayer Graphene," *Science*, vol. 321, no. 5887, pp. 385–388, 2008.